Morphogenesis and Growth of Soft Biological tissues

Anna Dai

Thèse préparée à l'Ecole Normale Supérieure
Sorbonne Université

École doctorale 564 Physique en Ile-de-France

Morphogenesis and Growth of Soft Biological tissues

Morphogenèse et croissance des tissus biologiques mous

presented by Anna Dai

Thèse de doctorat de Physique

- directed by

  Martine Ben Amar, Professeur à l'École Normale Supérieur et à Sorbonne Université

- presented and publicly defended on Monday 18 September 2023, and the jury composed of

  Jean-François Joanny, Professeur à l'Institut Curie, examinateur SU, président
  Mokhtar Adda-Bedia, Directeur de recherche à l'École normale supérieure de Lyon, rapporteur
  Yoël Forterre, Directeur de recherche à Aix-Marseille Université, rapporteur
  Alain Goriely, Professeur à Oxford University, examinateur
  Mingming Wu, Professeur à Cornell University, examinateur
  Michel Labouesse, Professeur à Sorbonne Université, invité

Morphogenesis and Growth of Soft Biological tissues

Morphogenèse et croissance des tissus biologiques mous

par Anna DAI

Résumé

Les tissus et organes biologiques possèdent une multiplicité de structures et de morphologies qui sont intimement liées à leurs conditions environnementales et à leurs fonctions. Leur organisation, leur forme et leur évolution sont profondément influencées par la régulation mécanique au cours de leur croissance et de leur développement. Pour clarifier ce processus complexe, les outils mathématiques aident à reconstruire l'ensemble du processus de croissance et de développement en analysant des modèles physiques impliquant la géométrie, la croissance, la déformation active, les propriétés des matériaux et les facteurs environnementaux. Cette thèse se focalise sur la matière molle active biologique dans deux cas : la croissance des feuilles naturelles et la transformation de la forme des embryons de *C. elegans*. La formation et l'évolution de la morphologie sous le couplage force-croissance et le mécanisme d'interaction entre l'information biologique et la mécanique sont élucidés grâce au développement d'un modèle théorique d'élasticité continue, combiné à l'analyse de données expérimentales et à la simulation par éléments finis.

Mots-clés

Morphogenèse, morphoélasticité, biomécanique, réseau actif, croissance des feuilles, représentation conforme, embryogenèse de *C. elegans*

Abstract

Biological tissues and organs possess a multiplicity of structures and morphologies that are intimately linked to their environmental conditions and functions. Their organization, shapes and evolution are profoundly influenced by mechanical regulation during their growth and development. To clarify this complex process, mathematical tools help to reconstruct the entire growth and development process by analyzing physical models involving geometry, growth, active deformation, material properties, and environmental factors. This thesis focuses on the biological active soft matter in two cases : the growth of natural leaves and the shape transformation of *C. elegans* embryos. The formation and evolution of morphology under force-growth coupling and the mechanism of how biological information interacts with mechanics, are elucidated through the development of a continuous elasticity theoretical model, combined with the analysis of experimental data and FEM simulation.

Keywords

Morphogenesis, morphoelasticity, biomechanics, active network, leaf growth, conformal mapping, *C. elegans* embryogenesis

Acknowledgements

I would like to express my heartfelt gratitude to my supervisor, Martine Ben Amar, for her patience and invaluable guidance throughout my doctoral journey. In the first year of my Ph.D life, when I found myself overwhelmed by the intricacies of theoretical research, Martine nurtured my understanding from the theoretical fundamentals to formula derivations. Because of the primary focus on experimental research during my Master's studies, she has generously spent extra time and effort to teach me. I am grateful to her for always being there when I needed her and helping me whenever I encountered difficulties. Every discussion and exchange with her has enriched me, thanks to her vast knowledge and extensive research experience. The role of Martine extended beyond that of a supervisor, she made me feel like family while I resided in a foreign land. I am immensely grateful for Martine's continuous support and guidance throughout the past four years.

Within our group, I would like to extend my appreciation to Joseph Ackermann, Ting Wang, and Paul-Qiuyang Qu, for their help in scientific and numerical discussions. Their insightful perspectives and expertise have provided much help and inspiration for my scientific work. Moreover, I am grateful for the warm and supportive environment that our small team has cultivated.

I would also like to thank Michel Labouesse and Kelly Molnar, whom I have learned from working with experimentalists. And it was a pleasure to have a fruitful discussion with them about the experimental observations on the elongation of *C. elegans* embryos.

I express my sincere gratitude to Yoël Forterre and Mokhtar Adda-Bedia for graciously accepting the role of rapporteurs for my thesis. Many thanks to Alain Goriely, Mingming Wu, Jean-François Joanny, and Michel Labouesse, for their esteemed presence as jury members. It is an honor to have this chance to communicate and discuss with them about my thesis. I hope that they will enjoy this thesis as well as the defense.

Pursuing a Ph.D. proved to be a captivating and demanding journey, full of numerous obstacles and setbacks. Nonetheless, I feel extremely happy with the unwavering support of my parents, despite their limited comprehension of my pursuits. Every conversation with them fortifies my resolve and reaffirms that they will always be my port of call. My husband is in touch with me almost every day and although the epidemic has meant that we have seen very little of each other over the past four years, his concern for me makes me feel that he is always there for me. Being a fellow researcher, he comprehends my emotional journey, providing invaluable encouragement. I am immensely grateful for the unwavering support of my family throughout this endeavor.

Finally, Many thanks to the director of our laboratory Jean-Marc Berroir, and the administrative staff, notably Nora Sadaoui, Delphine Rolland, Christine Chambon and Olga Hodges, for their efficiency and availability, and thanks to the Internet technical staff Yann Colin.

Table of Contents

Introduction

Biologically active soft matter converts external or stored energy into its own kinetic energy, causing itself to move or deform, and is the most important type of material that makes up living systems. From macroscopic flocks of birds, fish and bees to swimming bacterial communities, migrating cell monolayers and the internal skeleton of cells, all are active substances. As a result of the interactions between the basic units that make up active matter, and between these active units and the environmental medium, the whole system exhibits a rich dynamical behavior. Scientists have been exploring their behavior and believe that it must follow a particular pattern.

Active soft matter in biological systems self-organizes to form rich mechanical morphologies and biochemical patches that reflect the evolution of non-equilibrium systems from disordered to ordered structures over a wide range of spatial and temporal scales. From the formation of spiral and stellate clusters of active actin networks at the subcellular scale [1] to the formation of epithelial folds in tissues and organs such as the chicken embryonic gut [2], which shows the diverse mechanical self-organizational morphology of living systems. Such patterns and phenomena have attracted scientists from a wide range of disciplines, including chemistry, physics, mechanics and mathematics, they follow the biological findings and study the network of processes and all the influences that constitute the phenomenon of morphogenesis, with the ultimate aim of identifying, quantifying and theorizing the mechanisms that give rise to these structures and forms.

The original idea of mechanical forces influencing morphogenesis is not traceable for us, but the modern concept, which is built on the relationship between mathematics and biology, was first proposed by Darcy Wentworth Thompson in his book "On Growth and Form", published in 1917. Subsequently, in 1952, Turing proposed a model in which two morphogenetic elements with different diffusion coefficients - an activator and an inhibitor, respectively - undergo reactive diffusion to form a spatially self-organized patchwork. This model ignored the mechanics. Taken together, these two perspectives believe that physicochemical mechanisms, in close conjunction with biological factors, are involved in the emergence of universal structures in biological objects and can explain the morphological evolution and bio-chemical patchiness of biological developmental processes. To date, a large body of theoretical and experimental work has supported this, including the researchs of leaves, petals, algae, blades of grass, skin, birthmarks, melanomas, biofilms, arteries, etc. It is now well-established that the phenomenon of morphogenesis is clearly an interdisciplinary issue.

The study of active soft matter in living systems can help to reveal the mechanisms of complex morphological self-organization generation in embryonic development and to understand the complex dynamics of the evolution of living systems. With this in mind, the aim of this thesis is to elucidate

the coupling between growth and stress and their morphogenetic processes through theoretical models developed for two different research objects.

Presentation of the thesis

The aim of this thesis is to develop theoretical models for biologically active soft substances and to compare and analyze these models with the results of experimental and simulation simulations. Before discussing the work on the two different topics of this thesis, the phenomena of growth and morphogenesis as well as the background and current state of research are first presented in chapter 1, including some of the underlying concepts and theories used in the subsequent work.

First, in chapter 2, we investigate the morphological evolution of 2-dimensional stress-free growth. Based on two different theoretical derivations, one of which continues the previous definition of the basis [3] but removes the constraints from the derivation process. The second and more simplified approach is to define the initial and final configurations by means of complex functions, to obtain the morphological evolution from an energy minimization perspective, and we have concluded that 2-dimensional stress-free growth follows a conformal or quasi-conformal mapping. This conclusion is verified in the growth of planar natural leaves.

In chapter 3, we investigate the early elongation of *C. elegans* embryos under the influence of acto-myosin, providing a brief background on its biology and understanding the mode of acto-myosin activity. Then finite element simulation work was carried out and compared the results of previous theoretical studies by our group [4]. To further investigate complete elongation in the *C. elegans* embryo, we simplified the model by treating the epidermis as the same matter and considering the muscle structure. In addition, we simulated actin activity at this stage based on a kinetic model of myosin recruitment.

As a continuation of the early elongation problem in chapter 3, the main focus in chapter 4 is on late elongation resulting from the combined action of muscle and actin. We present a coupled bio-mechanical analysis model that illustrates the actual structure of worm biology. The model translates biochemical stimuli into driving forces and describes in detail all the deformations that occur during elongation. As the periodic contraction of the muscle is able to accumulate elastic energy, this energy is transferred to the circumferential actin network, which then allows the embryo to increase in length. Remarkably, we have also assessed for the first time the non-negligible rotation based on muscle activity and the viscous torque generated by the interstitial fluid within the egg.

The *C. elegans* study is an example of a closely collaborative study with an experimental team (Prof. Michel Labouesse and his group) whose ability to compare the results of theoretical modeling and experimental data provides a better understanding of physical phenomena in living organisms.

Chapter 1

Morphogenesis and elasticity of biological tissues

1.1 Research background

1.1.1 Basic understanding of the growth

Growth, one of the most fundamental and crucial biological activities, describes the process by which the mass of biological organs and tissues changes over time, resulting in a variety of forms as volumes shift and morphologies evolve. This intricate process involves a multitude of complex physiochemical reactions. At the microscopic scale, these reactions include protein production, cell division, and differentiation, all of which are controlled by a mix of internal and external factors, including the genetic code, nutrition, physical and chemical environments, and biological stimuli. At the macroscopic scale, the production of these proteins, cell division, and differentiation further determine morphogenesis, development, maintenance, disease, and aging [5, 6]. While normal and benign growth enables organisms to thrive and achieve their full potential, malignant growth such as cancer, aneurysm, or inflammation can impede essential biological functions and even be fatal [7, 8, 9, 10]. However, the mechanisms behind genetic transformation, cell differentiation and migration, and adaptive growth and remodeling remain challenging enigma in biology today. Fully understanding how organisms regulate their shape and function through growth and remodeling remains a daunting task.

By taking into account how the body changes during development, either by changing its volume and material properties or by rearranging the relative position of material points, three main growth processes can be distinguished [6]:

- **Growth:** Growth can be conceptually defined as the increase in mass or, by extension, as the characterization of a decrease in mass. Increases in mass can occur while maintaining constant density, such as in the context of soft tissue growth, or while maintaining constant volume, as seen in the formation of osteophytes.
- **Remodeling:** It mainly refers to the evolution of material properties such as stiffness, fiber orientation, fiber strength, etc., but the mass does not change. These remodeling processes are due to

changes in the microstructure that determine the overall behavior of the tissue. It is well known that during the aging process, tissues may become stiffer or softer [11, 12].

- **Morphogenesis:** During the early embryonic stage, new tissues and organs undergo development. In this process, the main reorganization and differentiation of cells occur following cell division, where only one material element is reorganized. For this process to take place, it is crucial that the adhesions between the different components are weak enough to enable their separation and subsequent reattachment.

1.1.2 Modelling of growth

The growth can be broadly classified into three types according to the location of the growth: tip growth, surface growth, or volume growth.

Tip growth

Tip growth describes the growth process that occurs in a small area at the tip of a filamentous structure. It is a polarised form of growth in living cells and results in a cellular form with an elongated cylindrical shape with a rounded tip where the growth activity takes place. It is the main growth mechanism used by many microbial and plant systems, such as fungal hyphae, which extend continuously at their extreme apices [13, 14, 15, 16, 17, 18], as shown in Fig.1.1 (a)-(d) Another example is the growth of root hairs and pollen tubes, whose volume develops almost in a single direction or is mainly one-dimensional, which can also be considered as tip growth [19, 20, 21], as shown in Fig.1.1 (e)-(f).

In these organisms, a small active growth zone exists at and near the tip, where new material is constantly being added. For small organisms such as filamentous bacteria, the newly added material is transported to the tip by diffusion processes, whereas for larger organisms such as fungi and pollen tubes, complex internal structures are required for propagation.

The main questions in mechanics are to understand the interaction of the tip with its environment and to determine how its morphology, internal stresses, and their evolution during development. How the structure changes according to different methods of material addition. These questions it related to the deposition of new materials on the cell surface and the mechanical deformation caused by the turgor pressure of the cell [19].

Surface growth

Surface growth, also known as cumulative growth, can be used to denote the proliferation or removal of material from the external or internal surfaces of a tissue. For instance, deposition occurs in hard tissues when new material is added to the existing boundaries of bodies. It is a typical growth mechanism for teeth, corals, horns, nails, antlers, shells, bones, tree trunks, etc [6, 22, 23, 24, 25, 26, 27]. In some cases, such as nails and horns, the surface where growth occurs is fixed relative to the main structure of the animal (e.g. the skeleton). In other cases, growth occurs on external surfaces, such as shells and antlers, so that as growth proceeds, the form, and position of the growing surface itself change in

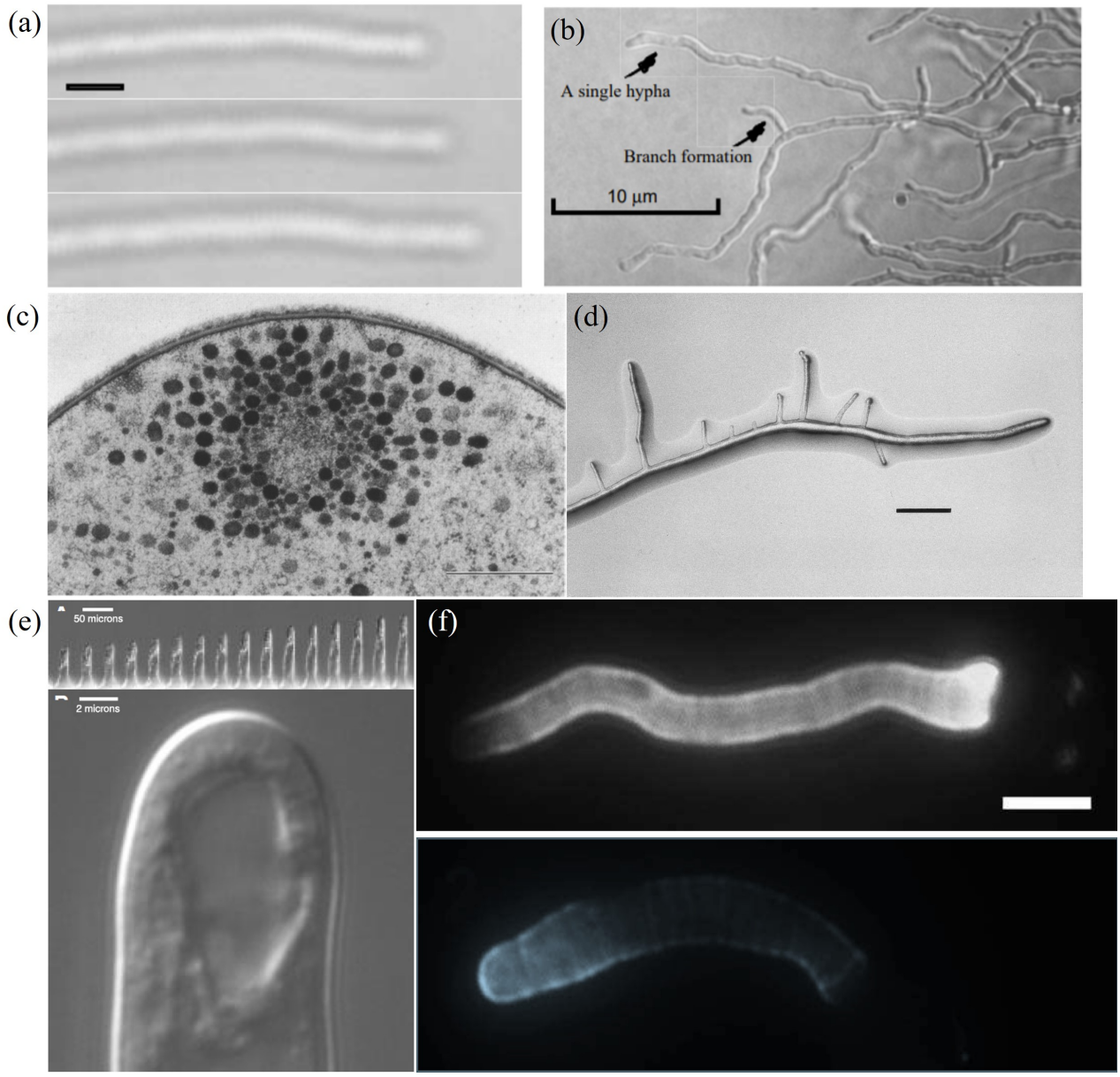

Figure 1.1 – *(a) Time lapsed sequence of hyphal growth of Streptomyces coelicolor. Each image is 150 sec apart (the bar is* $1\mu m$*) [18]. (b) Mycelial growth of S. coelicolor on solid agar medium [17]. (c) The Spitzenkörper of Scterotium rolfsii. Note the dense aggregate of apical vesicles and microvesicles surrounding a fibrillar, vesiclefree core, Bar:* $0.5\mu m$ *[16]. (d) Tip growing hypha of Saprolegnia ferax with numerous subapical branches [15]. (e) Tip growth in root hairs. Above: Time-lapse images of an elongating root hair of Medicago truncatula. Images were taken every 10 minutes. Below: Close-up of the growing tip [19]. (f) Above: Immunofluorescence label of Solanum chacoense pollen tube for pectins with a low degree of methyl-esterification using monoclonal antibody JIM5. Label intensity is stronger at the shank of the tube than at the apex (located at the left). Bar:* $10\mu m$ *µm. Below: Immunofluorescence label of Solanum chacoense pollen tube for pectins with a high degree of methyl-esterification using monoclonal antibody JIM7. Label intensity is higher at the apex (located at the left) [20].*

space relative to the main structure of the animal. Fig.1.2(a)-(f) shows some examples of surface growth obtained by numerical calculations that well mimic the surface growth of actual biological structures.

In mathematical modeling, the growth process can be captured by a growth velocity vector which can be normal to the growth surface, for example in mathematical and numerical simulations of bone remodeling it is generally assumed that surface growth can be described by a normal velocity vector to

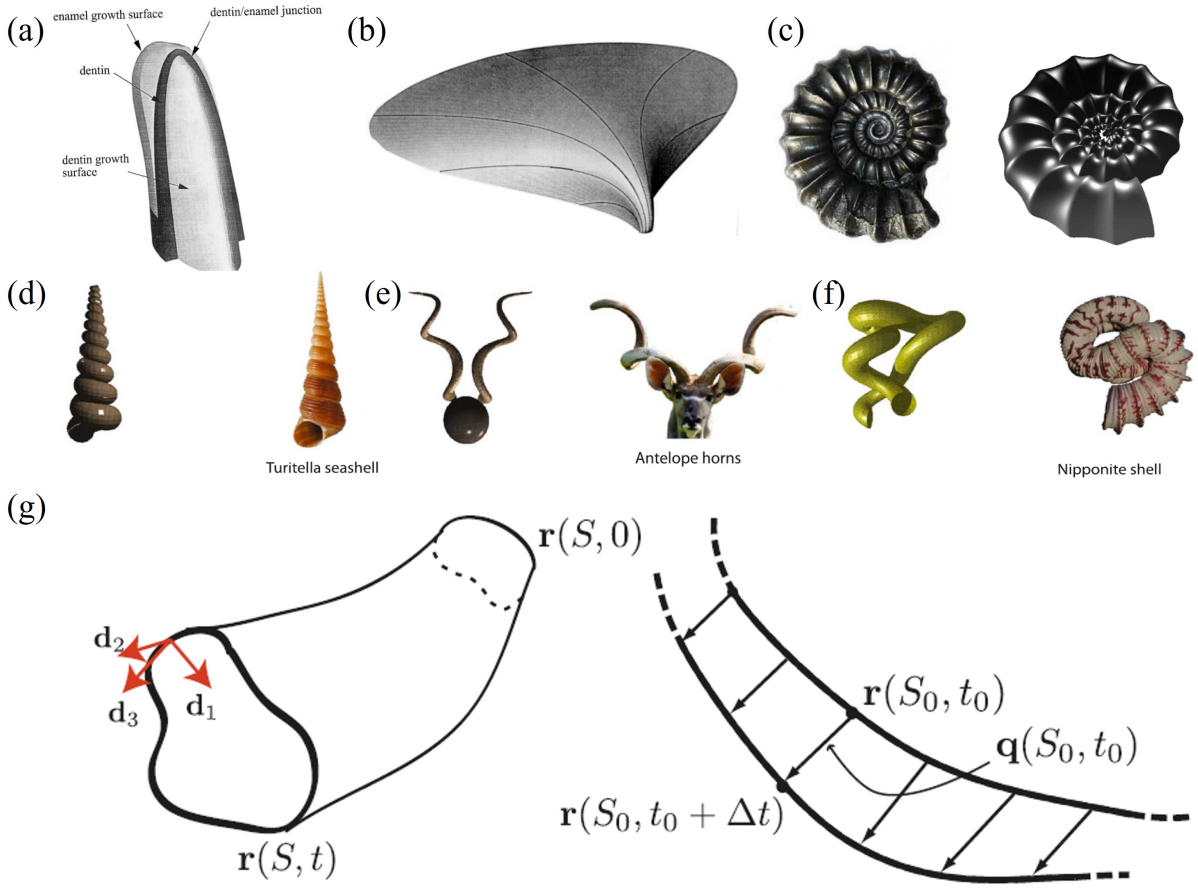

Figure 1.2 – *(a) Simulation image of the growth of the crown of a tooth (incisor). [25]. (b) Simulation image of a model of a bivalve leaf [25]. (c) Simulation of an ammonite [26]. Biological structures and its simulation image: (d)a Turitella seashell, (e) Antelope horns, and a (f) Nipponite shell [27]. (g) Create surfaces from the initially generated curves [27].*

the growth surface [28, 29]. While this may be sufficient for circular structures, in the case of some sharp angles the growth velocity must be considered to be at an angle to the growth surface. This is already known from anatomical and developmental studies, where generated cells and new tissue tend to be at an angle to the normal of the growth surface. Since surface growth is a continuously forming process, obtaining a mapping of the reference configuration to the current configuration is challenging. Moulton *et al.* [27] developed a mathematical framework to model the kinematics of surface growth of objects that can evolve a curve by evolving in space. Growth is determined by the growth velocity vector field at each point on the generating curve. Each point on the generating curve has a local orthogonal basis and the velocity field is given in the direction of the local coordinates by which such objects can eventually be generated by evolving this curve, the schematic image as shown in Fig.1.2 (g). In summary, in modeling, it is first necessary to understand the interactions between the soft material parts of biological tissue and the added hard material and then to derive their corresponding accretion law.

Volume growth

Volumetric growth, also known as bulk and interstitial growth, is a process that describes the change in local volume elements in the body over time. This process leads to incompatibility and generates residual stresses. Tip and surface growth, mentioned earlier, is where new material is added to a specific

surface or area and eventually produces changes at its boundaries. Volumetric growth, on the other hand, occurs as the interstitial growth of local volume elements. It is a very common mode of growth in biology, such as the volumetric changes and morphological evolution of blood vessels, muscles, solid tumors, and hearts [30, 31, 32, 33, 34, 35], some examples are shown in Fig.1.3.

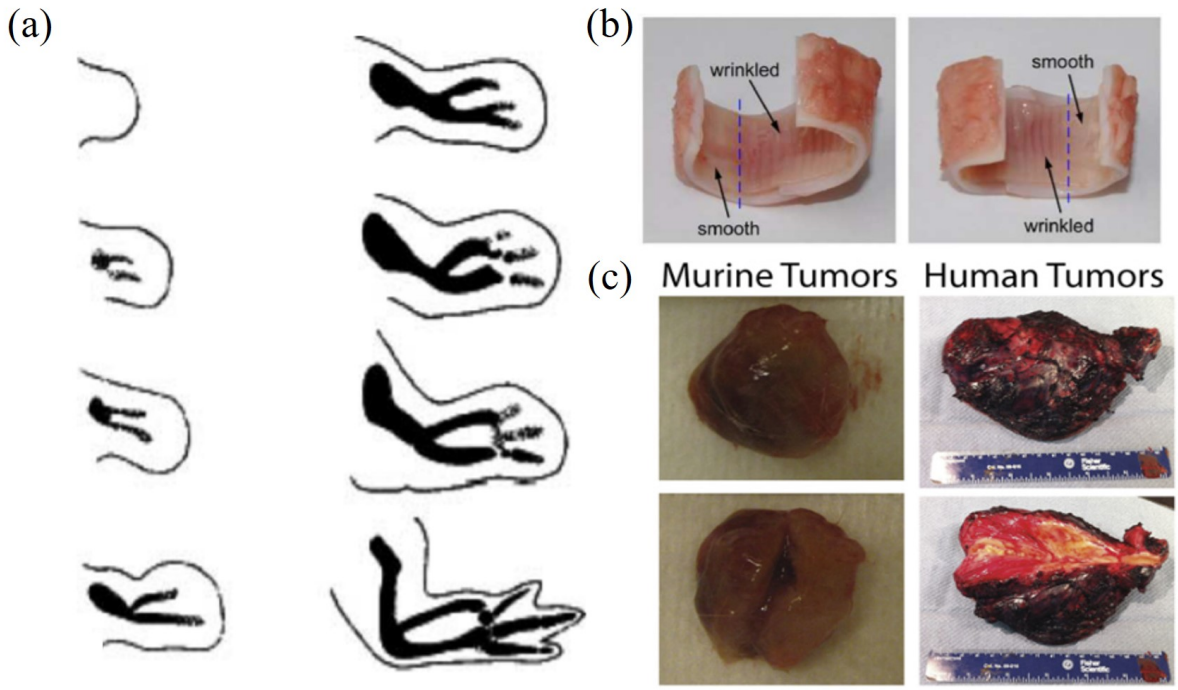

Figure 1.3 – *(a) Development of the chick limb bud between four and seven days of incubation. The solid black regions represent definitive cartilage; striped areas represent early cartilage [36]. (b) Experiments of localized, growth-induced wrinkling in porcine airways [33]. (c) photographs of the initial and final shape of the tumor. [34].*

In volumetric growth, local volume elements may not remain isotropic during growth and we need a tensor description of the deformation. The process of volume growth assigns a tensor, the growth tensor G, at each point in the body, describing the change in a local volume element. From a continuum mechanics perspective, it is assumed that local differential growth and/or overall inhomogeneous growth will lead to incompatibility [37], and this is also seen as a source of residual stress. Physically, incompatibilities may lead to overlapping objects or the creation of gaps, hence the need for elastic deformation to keep all pieces of materials continuous with each other after growth [38], this will also be explained in detail later.

As mentioned above, a body goes from its initial state to its final state when it is due to the growth or elastic response of the material, mostly a combination of these two processes. But in the case of soft tissue, it is possible to produce deformation by applying a load. So, if we know the form of a body after natural growth, but if it is subjected to different loads during growth, how will its form change [39]? This is still a problem that haunts physicists and biologists alike.

1.1.3 The relationship between the mechanics and growth

D'Arcy Thompson proposed the idea that mechanical forces affect morphogenesis in the book "On Growth and Form", first published in 1917 [40]. Usually from a biological point of view, growth is controlled and regulated by genes, with different genes controlling different cells and their activities such as cell division, proliferation, and expansion, determining their growth information and the shape of the body. However, the importance of mechanical stress during the growth and development of living organisms has been demonstrated, and it couples with genetic and also biochemical signals to determine their final shape.

The effects of mechanical stress on the morphology of biological tissue can be observed in daily life. For example, increased training for a specific limb in athletes clearly promotes muscle growth in the corresponding region; facial expressions will result in wrinkles form[41], while 'rhytidectomy' eliminate wrinkles and flatten the face; astronauts lose bone mass during space flight due to the effects of reduced gravity [42]; wearing excessively high heels for a long time can lead to the skeletal of foot deformities [43]. There are similar examples in plants, such as specially shaped fruits obtained through fixed-shape moulds, and trees becoming shorter and thicker in windy places [44].

Mechanical stress can also have an effect at the cellular level, cells can undergo both passive responses to mechanical signals from the external environment, such as deformation and displacement, and active responses, such as the generation of force-sensitive biochemical signals in the cell membrane or cytoplasm. This forms a force-chemo-biotic feedback loop, whereby mechanical signals can stimulate biochemical signaling pathways, and biochemical signals can alter the ability of cells to generate, transduce and receive mechanical signals. Many life processes, such as cell migration, cell polarisation, cell differentiation, wound healing and tissue regeneration, rely on the perception and transduction of force-chemical signals over long periods of time and on a spatial scale. It is well known that cells sense and respond to complex mechanistic signals throughout their life cycle.

As described above, we have known that growth is under the influence of stress, and indeed that growth also can lead to the stresses generated. Most of the biological tissues in different locations grow at different rates due to the coupling of mechanical, chemical and biological factors. Such differential growth can lead to the generation of internal residual stresses, even in the absence of external loading [45]. Residual stress is widely present in biological tissues such as ripe fruits, tree trunks, blood vessels, or tumors and is thought to have a crucial influence on basic biological activities [46, 47, 48, 49], and we can observe the presence of residual stress in living organisms by cutting in different directions (opening angle method), as shown in the Fig.1.4 (a)-(c).

As the body grows and residual stresses increase, internal, surface or structural instability may occur at an amount of the growth. Morphological instability then forms new stable patterns, which are significant for life because some normal biological activities and basic functions strongly depend on patterns. For example, the wrinkles found in the intestine are useful for digestion [55], while folds in the brain cortex are associated with cognitive development [56]. Some patterns may also reflect pathological information; for example, abnormally wrinkled airways are a sign of asthmatic bronchi, and frequent morphological changes in tumors point to a pre-metastatic state [57]. Some of the instability patterns are shown in Fig.1.4 (d)-(f).

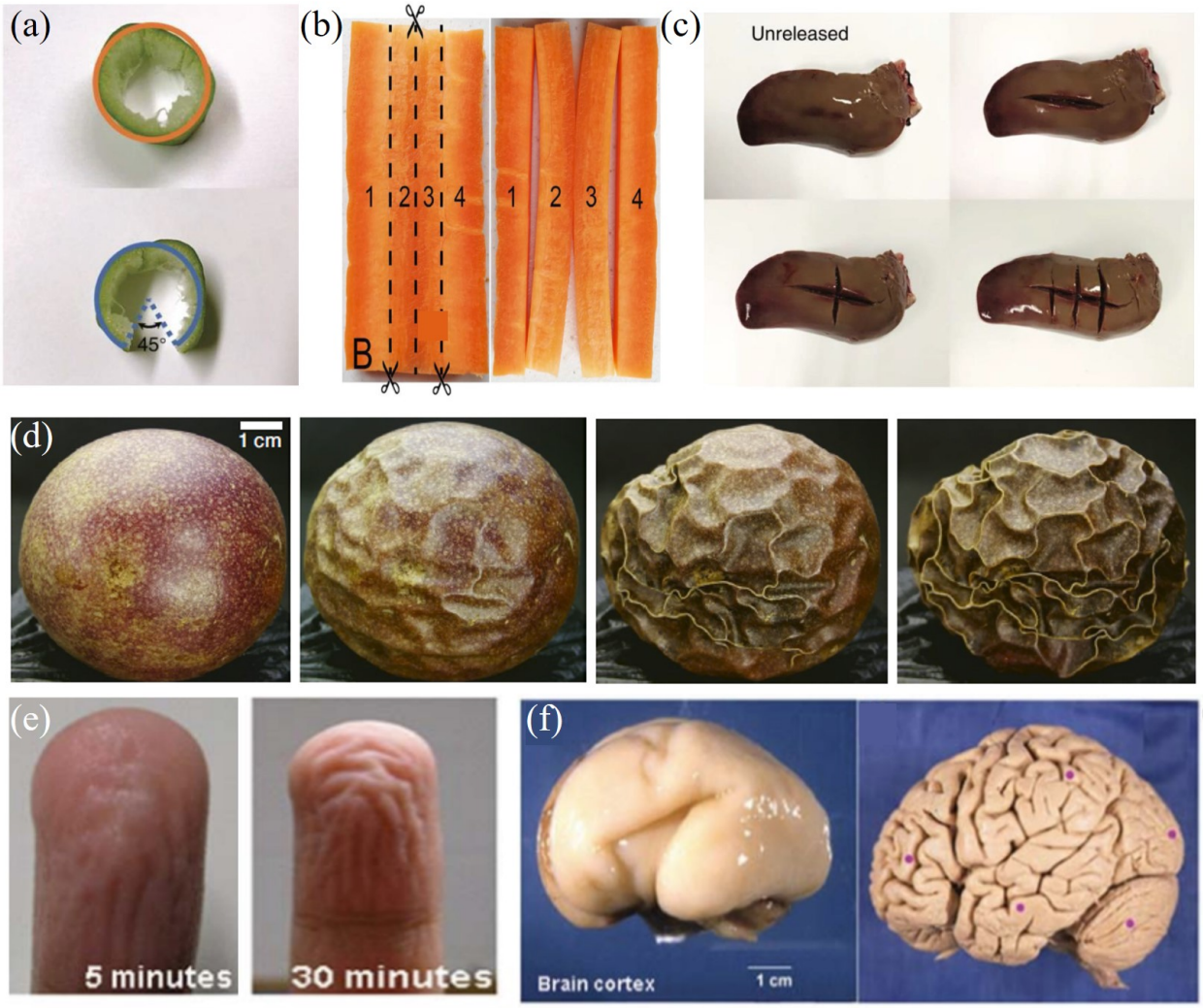

Figure 1.4 – *(a) Demonstration by the opening angle of a scallion ring after cutting along the axial direction [50]. (b) Cutting an axial slab of fresh carrot along the dashed lines reveals that the outer layers (1 and 4) were almost stress-free whilst the core layers (2 and 3) were subjected to large inhomogeneous axial and radial residual stresses [51]. (c) Influence of the number and direction of cuts to release residual stress in a duck liver [50]. (d) Evolution of wrinkling topography in excessive dehydration of deformed passion fruit [52]. (e) Representative wrinkled morphology of fingertips with different immersed times [53]. (f)) The surface is relatively smooth in the fetus period yet, it folds into a pattern with bumps and grooves during growth [54].*

Here, it is important to mention the concept of 'Homeostasis', derived from the Greek words meaning 'same' and 'steady'. Homeostasis refers to the ability of the organism or system to maintain internal stability and equilibrium in response to changes in the external environment. It is a fundamental concept in biology and is essential for the proper functioning and survival of living organisms. The study of homeostasis has a rich history, spanning centuries. The concept of maintaining internal balance can be traced back to ancient Greek and Roman philosophers who recognized the importance of balance in the human body. One of the earliest recorded references to balance was by the Greek physician Hippocrates, often referred to as the 'father of medicine'. He introduced the concept of '*physis*' (nature) and the ability of the human body to maintain a balance between the four humors - blood, phlegm, yellow bile and black bile [58]. The French physiologist Claude Bernard described the concept of regulating the internal environment in 1849, while the term homeostasis was coined by the physician Walter Bradford Cannon

in 1930 [59, 60]. His book "The Wisdom of the Body" [60], described how the human body maintains steady levels of temperature and other vital conditions such as water, salt, sugar, protein, fat, calcium and oxygen levels in the blood. Similar processes dynamically maintain the homeostatic conditions of the earth's environment. In 1932, the British physiologist Joseph Barcroft was the first to suggest that the higher function of the brain requires the most stable internal environment. Thus, in Barcroft's view, homeostasis is not only organized by the brain, but also at the service of the brain [61]. Homeostasis is an almost exclusively biological term, concerning the constancy of the internal environment in which the cells of the body live and survive [59, 60, 62].

In homeostasis, various physiological processes work together to regulate and maintain internal conditions within a certain range, regardless of external fluctuations. These internal conditions include body temperature, pH level, blood pressure, heart rate, fluid balance, and nutrient levels, among others. The process of homeostasis involves continuously monitoring the internal environment with specialized sensors, such as receptors or chemoreceptors, which detect changes in various parameters. When a deviation from the optimal range is detected, the body initiates a series of responses to restore equilibrium and bring the conditions back to normal. Homeostatic mechanisms involve negative feedback loops, where the response counteracts the initial change and brings the system back to its set point. For example, if body temperature increases, the body responds by initiating mechanisms like sweating and vasodilation to cool down and restore the normal temperature [63, 64]. Various organ systems in the body play a role in maintaining homeostasis. The nervous and endocrine systems, in particular, are crucial in coordinating and regulating the responses required to maintain internal balance. Overall, homeostasis is a vital process that ensures the stability and functionality of living organisms, allowing them to survive and adapt to changes in their environment.

1.2 Current status of research

The variety of morphological changes exhibited by living systems has always attracted the attention of scientists alike [40, 65]. The active soft matter of biological systems, such as organs and tissues, evolves morphologically for two main reasons: firstly, it can produce active force and active deformation, which leads to self-driven and self-organized morphological evolution; secondly, growth and remodeling lead to an increase or decrease in the matter, which results in a self-organized morphology. Depending on the system being studied, the active deformation and the growth model determine whether a discrete particle model or a continuous medium model is used. The discrete particle model usually is used for the study of cells, but the biological tissues or organs, the continuous medium model is better. This paper focuses on the continuous medium model.

Continuous medium models of active soft matter in living systems include active fluid models [66, 67] and active solid models [68]. These models can in turn be classified according to the geometrical configuration and material properties of the tissues under study. For two-dimensional structures commonly found in biological tissues, such as thin films and thin-shell structures, researchers have developed active fluid film models [67, 69], active Helfrich film models [70, 71] and active solid thin-shell models [72, 73]; for three-dimensional biological tissues, there are deformation gradient multiplicative decomposition models analogous to those used to describe plastic deformation of elastomers [74], active

colloid model [75], etc. There are various physical models to describe active deformation processes in continuous media active substances, three common approaches are described here. The first is to decompose the stress σ of the material into a passive stress σ^p and the introduction of an active stress σ^a that

$$\sigma = \sigma^p + \sigma^a. \tag{1.1}$$

This active stress can depend on physical quantities such as the concentration of local biochemical signals, the orientation of active fibers or the order parameter of active polar fibers [72, 75, 76]. For biological thin plates or thin shell structures, such as cell cortices and epithelial cell monolayers, researchers often introduce assumptions or set up spatiotemporally inhomogeneous distributions of surface tension as active stresses based on experimental results. A second approach is to add an energy term related to the concentration of biochemical signals to the free energy of the passive material. This model is often used to study membrane protein distribution and membrane morphology evolution, for example, morphology evolution due to protein distribution on vesicle membranes [71] and morphology formation in red blood cells [77]. A third approach is to decompose deformation into active and passive deformation. For three-dimensional large deformation problems, a multiplicative decomposition of the deformation gradient tensor $\mathbf{F}$ can be performed,

$$\mathbf{F} = \mathbf{F}^e \cdot \mathbf{F}^a, \tag{1.2}$$

where $\mathbf{F}^e$ and $\mathbf{F}^a$ represent the passive elastic deformation part and the active deformation part of the material, respectively. For the common thin plate and shell structures in biological systems, the strain is small but the overall displacement can be large, i.e. small deformation and large rotation problems, when the additive decomposition of the deformation tensor can be used,

$$\mathbf{E} = \mathbf{E}^e + \mathbf{E}^a, \tag{1.3}$$

where $\mathbf{E}^e$ and $\mathbf{E}^a$ represent the passive elastic deformation part and the active deformation part of the material, respectively.

Continuous medium models describing the growth of active substances have been mentioned in the previous section and include apical growth models, surface growth models and bulk growth models. In order to better understand the subsequent work in this thesis, in this section we first explain the basic theoretical approach to growth modeling. We then summarise some theoretical and simulation studies for various morphologies of different biological tissues during the growth.

1.2.1 The kinematics of growth

The kinematics of growth involves the precise tracking of spatial and temporal changes, including the expansion and relative deformation of various points within a body. In three-dimensional space, we consider as body $\mathcal{B}$ occupying a specific region within the spatial domain $\mathscr{E}$. Following deformation, body $\mathcal{B}$ transforms into $\mathscr{B}$, now occupying a distinct region within space. Describing the motion of each body point from its original position to its present state, we employ a vector mapping function $\overrightarrow{\chi}$. By

examining derivatives of this mapping in space and time, we extract the relative motion of neighboring points. Moreover, this mapping enables us to define fundamental quantities such as strain and stretch.

The concept of the configuration

We define a configuration for body $\mathcal{B}$, denoting the positions of all points within it as the vector $\vec{X}$. Subsequently, we introduce $\vec{\chi}$, a mapping that allows us to relate the points of body $\mathcal{B}$ to their respective deformed positions $\vec{x}$ within $\mathscr{B}$.

$$\begin{aligned} &\mathcal{B} \to \mathscr{B}, \\ &\vec{X} \to \vec{\chi}\left(\vec{X}\right). \end{aligned} \tag{1.4}$$

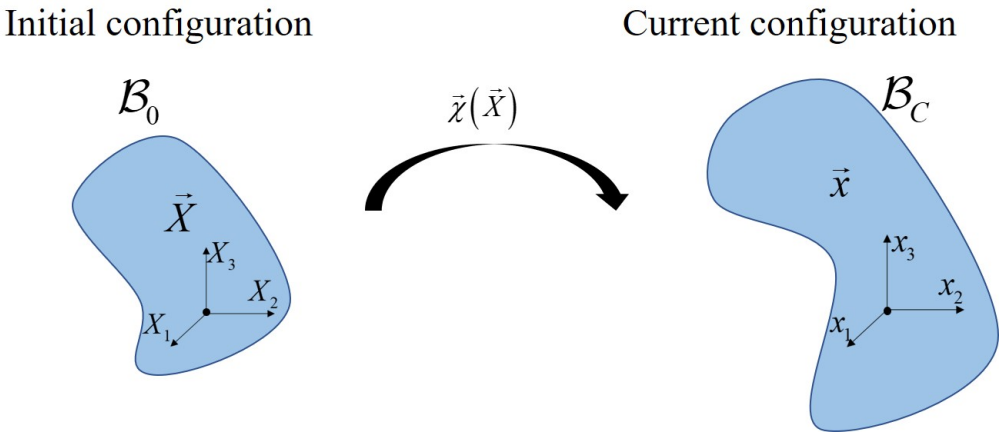

Figure 1.5 – *The schematic of the deformation.*

We also can write this relation:

$$\mathscr{B} = \vec{\chi}(\mathcal{B}) \quad or \quad \vec{x} = \vec{\chi}\left(\vec{X}\right),\ \vec{X} \in \mathcal{B}. \tag{1.5}$$

Prior to undergoing a deformation process, body $\mathcal{B}$ is in an initial (reference) configuration, comprising a collection of material points occupying a specific region in space denoted as $\mathcal{B}_0$, and for simplicity, we assume the initial configuration is the stress-free state. It is important to note that the initial (reference) configuration remains unaffected by time. However, as the body moves or undergoes deformation, this set of points can vary with time t, resulting in a configuration denoted as $\mathcal{B}_C$, representing the state of $\mathcal{B}$ at a given time t. Therefore, we have the following relationships:

$$\vec{x} = \vec{\chi}\left(\vec{X}, t\right),\ \forall \vec{X} \in \mathcal{B}_0, \tag{1.6}$$

The mapping $\vec{\chi}$ is assumed to be uniquely invertible:

$$\vec{X} = \vec{\chi}^{-1}\left(\vec{x}, t\right),\ \forall \vec{x} \in \mathcal{B}_C, \tag{1.7}$$

with inverse mapping denoted by $\vec{\chi}^{-1}$. For a given time t, the inverse mapping Eq.1.7 carries the points

located at the configuration $\mathcal{B}_C$ to the points at the reference configuration $\mathcal{B}_0$.

The deformation gradient

In order to analyze a deformation locally (in the neighborhood of a material point), it is necessary to characterize the deformation of an infinitesimal line element $d\vec{X}$ within the body $\mathcal{B}$. To accomplish this, let us differentiate Eq. (1.5). In Cartesian coordinates, the resulting expression is as follows:

$$dx_i = \frac{\partial x_i}{\partial X_j} dX_j = F_{ij} dX_i, \tag{1.8}$$

where we apply the Einstein notation on repeated indices, the Latin indices belong to the set $\{1, 2, 3\}$. The geometric deformation tensor $\mathbf{F}$ has been introduced here:

$$d\vec{x} = \mathbf{F} d\vec{X}, \quad \mathbf{F} = \frac{\partial x}{\partial X}. \tag{1.9}$$

Deformation of the volume

When a body undergoes deformation, it can change the relative sizes of its material elements. Let us consider an infinitesimal volume element formed by three non-coplanar line elements, namely $d\vec{X}_1$, $d\vec{X}_2$, and $d\vec{X}_3$, located at point $\vec{X}$ within $\mathscr{B}_0$. The volume dV of this infinitesimal element can be expressed as follows:

$$dV = \det\left(d\vec{X}_1, d\vec{X}_2, d\vec{X}_3\right). \tag{1.10}$$

In the current configuration, the corresponding volume element dv is given by:

$$dv = \det\left(d\vec{x}_1, d\vec{x}_2, d\vec{x}_3\right). \tag{1.11}$$

and the process is shown in Fig.1.6,

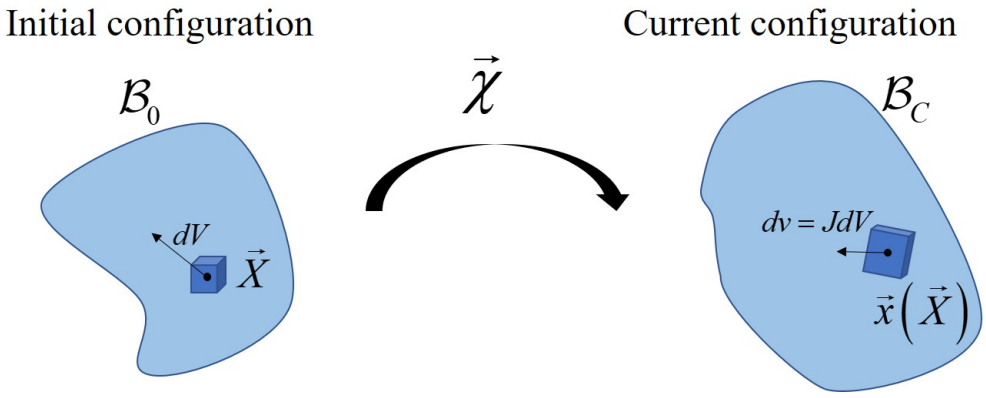

Figure 1.6 – *Transformation of volumes, dV is an infinitesimal volume element, the new volume after deformed $dv = JdV$.*

According to the Eq.(1.9), we can therefore rewrite Eq.(1.11) as follows:

$$dv = \det \mathbf{F} dV = J_F dV. \tag{1.12}$$

where $J_F = \det \mathbf{F}$, it means the local volume change, i.e. the ratio of a volume element of the current configuration to that of the reference configuration. If the volume does not change locally during the deformation:

$$J_F \equiv \det \mathbf{F} = 1, \tag{1.13}$$

If the Eq.(1.13) is satisfied, all deformations of $\vec{X}$ in $\mathcal{B}_0$ are isochoric.

Deformation of the surface

By considering a material area element that is normal to a given vector $\vec{N}$, we define an area element. Referring to the equation in Ref. [78], the transformation of the surface integral can be described:

$$\int_{\partial \mathcal{B}_0} \vec{n} da = \int_{\partial \mathcal{B}_0} J_F \mathbf{F}^{-T} \vec{N} dA \tag{1.14}$$

where $\vec{n}$ and $\vec{N}$ are outward unit normals, dA and da are the area elements at a given point as shown in Fig.1.7. An infinitesimal element of area defined in the initial (reference) configuration by a normal $\vec{N}$ and surface area dA is transformed into another element of the area in the current configuration defined by a vector $\vec{n}$ with area da and related to the reference one by Nanson's formula:

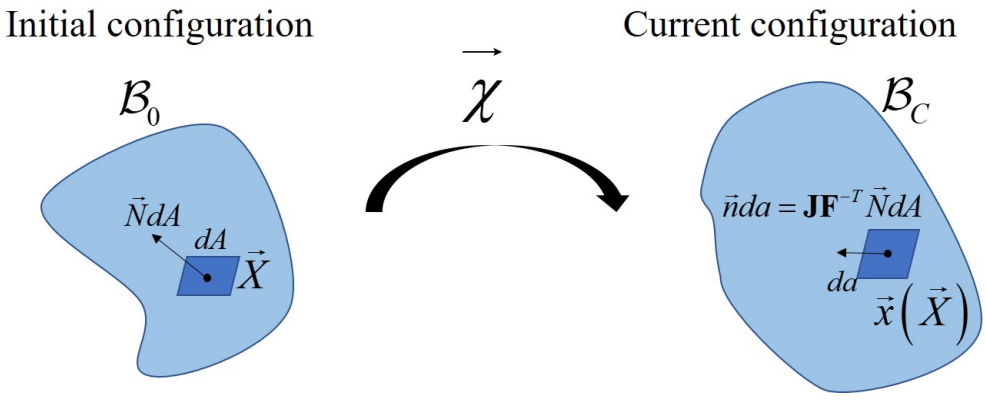

Figure 1.7 – *Transformation of areas. An infinitesimal area is transformed according to Nanson's formula during the deformation.*

$$da = J_F \mathbf{F}^{-T} \cdot dA, \quad \vec{n} da = J_F \mathbf{F}^{-T} \cdot \vec{N} dA. \tag{1.15}$$

Deformation Tensors

George Green introduced a deformation tensor, which is known as the right Cauchy–Green deformation tensor or Green's deformation tensor [79]:

$$\mathbf{C} = \mathbf{F}^T\mathbf{F}. \tag{1.16}$$

Physically, the right Cauchy-Green tensor provides the square of the local change in distances resulting from deformation:

$$d\vec{x}^2 = d\vec{X} \cdot \mathbf{C} \cdot d\vec{X} \tag{1.17}$$

Reversing the order of multiplication in the formula for the right Green-Cauchy deformation tensor leads to the left Cauchy-Green deformation tensor which is defined as:

$$\mathbf{B} = \mathbf{F}\mathbf{F}^{\mathbf{T}}. \tag{1.18}$$

The left Cauchy-Green deformation tensor is often called the Finger deformation tensor [79, 80].

Finite strain Tensor

In the initial (reference) configuration, if the distance of two points is:

$$\sqrt{dX^2} = \sqrt{dX_i dX_i}, \tag{1.19}$$

after the deformation, the distance change to the

$$\sqrt{dx^2} = \sqrt{dx_i dx_i}. \tag{1.20}$$

In terms of the tensor $\mathbf{F}$, we can write :

$$dx^2 = F_{ij}F_{ik}dX_j dX_k = C_{jk}dX_j dX_k. \tag{1.21}$$

where tensor $\mathbf{C}$ is right Cauchy-Green deformation tensor. It is symmetric and positive definite. Now, the variation of the square of a length element is :

$$dx^2 - dX^2 = \left(C_{jk} - \delta_{jk}\right) dX_j dX_k = 2E_{jk}dX_j dX_k, \tag{1.22}$$

where $\mathbf{E}$ is the Green strain tensor, also called the Green-Lagrangian strain tensor or Green-St-Venant strain tensor, $\mathbf{E} = \frac{1}{2}\left(\mathbf{C} - \mathrm{I}\right)$. A material element is deformed if and only if $\mathbf{E} \neq 0$. Since this tensor is associated with the reference configuration, it is called the Lagrangian strain tensor.

Multiplicative decomposition

As discussed in the previous section (Section 1.1), the growth process involves two factors: growth itself and elastic stress. Residual stresses in biological materials are directly linked to the internal material reorganization caused by growth. Even in the absence of external loads, changes in size or relative position of different elements within the body can generate stresses. Thus, the theory of elastic growth posits that the overall deformation results from a combination of growth-induced deformations and elastic deformations required to preserve the body's integrity.

The concept is based on the early contributions of several scientific groups [81]. It was first discussed by Flory [82] in a study of polymer swelling and was also mentioned by Kröner in the context of elasticity problems [83, 84, 85] and later generalized by Lee [86]. In the research field of biological tissues, it was the seminal work of Rodriguez *et al.* [38] that proposed multiplicative decomposition as a central concept in biomechanics, and then this approach was widely used[87, 88, 89, 90]. The method is based on three key points:

- There is an initial (reference) state without stress.
- The geometric deformation tensor admits a multiplicative decomposition into a growth tensor $\mathbf{G}$ and an elastic tensor $\mathbf{A}$:

$$\mathbf{F} = \mathbf{A}\mathbf{G}. \tag{1.23}$$

- The response of the material depends on total deformation ($\mathbf{F}$), but the elastic energy is only related to the elastic part ($\mathbf{A}$).

Consider an initial body without any geometric or physical constraints. And suppose that this body undergoes spatially homogeneous growth. In this scenario, a deformation (Eq.(1.5)) describes the transition from the initial state to the current state, without any cavitation or overlap occurring during this process. As a result, no elastic accommodation is required, and $\mathbf{A} = \mathbf{I}$, where $\mathbf{I}$ denotes the identity. However, it should be noted that this situation, where $\mathbf{A}$ and $\mathbf{G}$ can be directly expressed as gradients of deformation, is atypical but possible. Generally, neither $\mathbf{A}$ nor $\mathbf{G}$ can be directly represented as gradients of any deformation. Consequently, the "virtual state" $\mathscr{B}_G$ induced by the transformation $\mathbf{G}$ is not a physically achievable configuration of the body $\mathcal{B}$. Nonetheless, there is a conceptual procedure to obtain the $\mathscr{B}_G$ state. By progressively slicing the body $\mathcal{B}$ into an infinite number of infinitesimal pieces, the internal constraints can be theoretically relaxed. The shape of each sliced element defines the local deformation gradient $\mathbf{G}$. Therefore, the virtual state $\mathscr{B}_G$ is often described as a collection of configurations.

1.2.2 Balance laws

Now, we have established a comprehensive description of the deformation of a body. Initially, a mapping $\vec{\chi}$ is defined, followed by the deformation gradient $\mathbf{F}$, which captures information about the relative deformations of the body, including local changes in volume, area, and stretch. These primary quantities serve as the basis for defining secondary quantities, such as the left and right Cauchy-Green tensors, $\mathbf{B}$ and $\mathbf{C}$, which provide information about the strain developed during deformation. With a

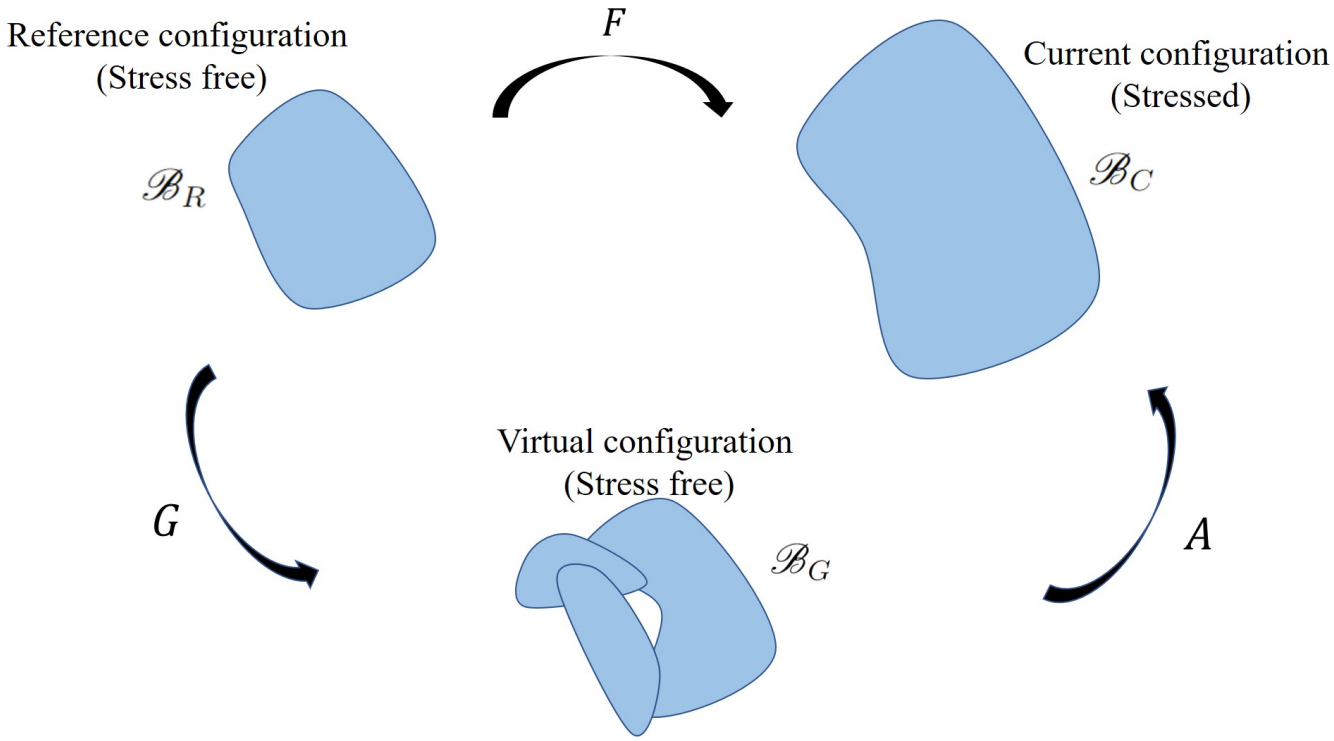

Figure 1.8 – *Schematic representation of the Multiplicative decomposition. The system, initially in a stress-free configuration $\mathscr{B}_R$, is first transformed into the virtual state $\mathscr{B}_G$, which maybe contains holes and overlaps. In the second step, the integrity of the $\mathscr{B}_G$ state is recovered by an elastic process, resulting in the stressed $\mathscr{B}_C$ configuration.*

complete kinematic description of the body, we can define physical fields at each point and utilize fundamental laws of physics to establish local equations connecting these fields. The equilibrium equations in continuum mechanics are derived by considering the balance of physical quantities, including mass, linear momentum, angular momentum, and energy. Here, we will specifically focus on the conservation of energy.

It is important to note that this approach is based on the Minimum Potential Energy (MPE) principle, also known as the variational method. According to this principle, among the set of kinematically possible deformations that satisfy only the boundary conditions of the displacement field, the observed deformations are those that minimize the potential energy. In other words, the actual deformations correspond to the ones that minimize the potential energy.

Elastic energy

The elastic process represented by the tensor $\mathbf{A}$ in Fig.1.8 is considered as a reversible process at temperature T, with the existence of a elastic energy $\mathscr{E}$. As mentioned earlier, this energy is assumed to depend only on the elastic component $\mathbf{A}$ of the decomposition in Eq.(1.23). Hence, it is a function of the deformation field $\vec{x}$, expressed as:

$$\mathscr{E} = \mathscr{E}(\vec{x}) \equiv \int_{\mathscr{B}_G} \mathcal{W}(\mathbf{A}) \mathrm{d}V_G \tag{1.24}$$

where dV_G is an infinitesimal volume element of the virtual state $\mathscr{B}_G$, and the integral is taken over the region $\mathscr{B}_G$. The quantity $\mathcal{W}$ corresponds to the elastic energy density [91, 92]. The definition in Eq.(1.24) implies that the energy is independent of the deformation process. Materials that satisfy this approximation are referred to as hyperelastic or Green's elastic materials, which do not include all viscoelastic or plastic effects.

The tensor $\mathbf{A}$ represents a local measure of deformation that depends on the choice of the observer. To obtain an expression for invariant energy under coordinate changes, an accurate approach is to use a local measure of deformation that is independent of the observer's choice, unlike the tensor $\mathbf{A}$. The right Cauchy-Green strain tensor $\mathbf{C} = \mathbf{F}^T\mathbf{F}$ is symmetric and positive definite. Its eigenvalues, also known as principal stretches, denoted as ${\lambda_1}^2$, ${\lambda_2}^2$, and ${\lambda_3}^2$, are real and strictly positive. Alternatively, it is common in the literature to define the elastic energy density $\mathcal{W}$ in terms of the principal invariants I_1, I_2, and I_3 of the tensor $\mathbf{C}$. These invariants are defined as:

$$I_1 = Tr\left(\mathbf{C}\right) = {\lambda_1}^2 + {\lambda_2}^2 + {\lambda_3}^2, \tag{1.25}$$

$$I_2 = \frac{1}{2}\left(Tr(\mathbf{C})^2 - (Tr\mathbf{C})^2\right) = \lambda_1\lambda_2 + \lambda_2\lambda_3 + \lambda_1\lambda_3, \tag{1.26}$$

$$I_3 = \det\mathbf{C} = {\lambda_1}^2{\lambda_2}^2{\lambda_3}^2. \tag{1.27}$$

If the material exhibits a preferred direction, indicated by a vector $\overrightarrow{m}$, such as in the case of fiber-reinforced materials, additional invariants are introduced based on the tensors $\vec{m}\otimes\vec{m}$ and $\mathbf{C}$ [93, 94, 95, 96, 97].

If the system is internally constrained, as in the case of incompressible materials, we have the condition $\mathbf{C}(\mathbf{A}) = \mathbf{0}$. To incorporate this constraint, we introduce a Lagrange multiplier p into the definition in Eq.(1.24), resulting in a modified function:

$$\mathscr{E}\left[\vec{x}, p\right] \equiv \int_{B_G} \mathcal{W}\left(\mathbf{A}\right) dV_G - \int_{B_G} p\, C\left(\mathbf{A}\right) dV_G. \tag{1.28}$$

Note the explicit dependence of the functional $\mathscr{E}$ on p, which also needs to consider in the variational procedure.

Hyperelastic materials or models possess several distinctive characteristics:

- 1: They can withstand significant elastic (recoverable) deformations, often up to 10 times the applied strain;
- 2: Hyperelastic materials can be compressible or incompressible. For living systems, it is usually considered incompressible, meaning their volume does not change significantly under deformation;
- 3: The constitutive relationship of hyperelastic materials may exhibit a high degree of nonlinearity, meaning that the relationship is not linear.

Due to their similarity to biological tissues in terms of these properties, hyperelastic materials are widely used in various biomechanical problems. One of the simplest hyperelastic models is the Neo-Hookean model, proposed by Ronald Rivlin [98] in 1948. This model is expressed as:

$$\mathcal{W} = C_1 \left(I_1 - 3 \right), \tag{1.29}$$

where C_1 is a material constant, which is half the value of the shear modulus. Although Neo-Hookean is not very accurate in predicting large strain deformation, it is simple and has strong applicability for small and medium strains.

The Mooney-Rivlin model is named after the combined surnames of two physicists, M. Mooney and R. S. Rivlin, they established the essence of the Mooney-Rivlin hyperelastic model[98, 99], the form is:

$$\mathcal{W} = C_1 \left(I_1 - 3 \right) + C_2 \left(I_2 - 3 \right) \tag{1.30}$$

where C_1 and C_2 are determined material constants.

A notable and widely used hyperelastic model is the Ogden model, developed by Raymond Ogden [100]. This model is highly versatile and applicable to various materials, including rubber, polymers, and biological tissues. One of its distinctive features in the theoretical formulation is the use of principal stretches as independent variables, instead of the strain tensor invariants. The expression of the Ogden model is given by:

$$\mathcal{W} = \sum_{p=1}^{N} \frac{\mu_p}{\alpha_p} \left({\lambda_1}^{\alpha_p} + {\lambda_2}^{\alpha_p} + {\lambda_3}^{\alpha_p} - 3 \right) \tag{1.31}$$

where N, μ_p and α_p are material constants. For particular values of material constants the Ogden model will reduce to either the Neo-Hookean material ($N = 1,\ \alpha_i = 2$) or the Mooney-Rivlin material ($N = 2,\ \alpha_1 = 2,\ \alpha_2 = -2$, with the constraint condition $\lambda_1 \lambda_2 \lambda_3 = 1$).

In addition to the models mentioned above, there are also common models such as Fung [101], Gent[102], etc.

Equilibrium equations and variational method

To derive the equilibrium equation, we can rewrite Eq.(1.28) as an integral over the reference (initial) configuration $\mathscr{B}_R$. Based on Eq.(1.12), the infinitesimal volume elements of the reference configuration $\mathscr{B}_R$ and the virtual state $\mathscr{B}_G$ are related by $dV_G = J_G dV_R$, where $J_G = \det \mathbf{G}$. Consequently, we can express the elastic energy equation as follows:

$$\mathscr{E}\left[\vec{x}, p\right] = \int_{\mathscr{B}_G} J_G \left\{ \mathcal{W}\left(\mathbf{A}\right) - p\, C\left(\mathbf{A}\right) \right\} dV_R, \tag{1.32}$$

according the Eq.(1.23), so we can reads:

$$\mathscr{E}\left[\vec{x},p\right]=\int_{\mathscr{B}_G}J_G\left\{W\left(\mathbf{F}\mathbf{G}^{-1}\right)-p\,C\left(\mathbf{F}\mathbf{G}^{-1}\right)\right\}dV_R \tag{1.33}$$

The principle of virtual work states that, during an isothermal deformation process, the infinitesimal change $\delta\mathscr{E}=\mathscr{E}\left[\vec{x}+\delta\vec{x},p+\delta p\right]-\mathscr{E}\left[\vec{x},p\right]$ of the elastic energy is equal to the work of the mechanical forces applied to the system. It is generally assumed that there are volume forces, denoted $\vec{B}$, and surface forces, denoted $\vec{T}$. Under these conditions, the principle of virtual work is written:

$$\delta\mathscr{E}=\int_{\mathscr{B}_R}\vec{B}\cdot\delta\vec{x}dV_R+\int_{\partial\mathscr{B}_R}\vec{T}\cdot\delta\vec{x}dA_R, \tag{1.34}$$

where dA_R is an infinitesimal element of the surface $\partial\mathscr{B}_R$. The energy $\mathscr{E}$ is a function of the fields $\vec{x}$ and p, we develop the variation $\delta\mathscr{E}$ in terms of the variations $\delta\vec{x}$ and δp:

$$\delta\mathscr{E}=\int_{\mathscr{B}_R}J_G\left\{\left(\mathbf{G}^{-1}\frac{\partial W}{\partial\mathbf{A}}-p\mathbf{G}^{-1}\frac{\partial C}{\partial\mathbf{A}}\right)\delta\mathbf{F}-\mathbf{C}\left(\mathbf{A}\right)\delta\mathbf{p}\right\}dV_R. \tag{1.35}$$

Generally, if $\mathbf{A}=\mathbf{BC}$, and any scalar function F of the tensor $\mathbf{A}$ have this relation:

$$\frac{\partial F\left(\mathbf{A}\right)}{\partial\mathbf{B}}=\mathbf{C}\frac{\partial F\left(\mathbf{A}\right)}{\partial\mathbf{A}}. \tag{1.36}$$

We now insert Eq.(1.36) into Eq.(1.35) and integrate by parts to obtain:

$$\int_{\mathscr{B}_G}J_GC\left(\mathbf{A}\right)\delta pdV_R-\int_{\mathscr{B}_R}\left(Div\mathbf{S}+\overrightarrow{\mathbf{B}}\right)\cdot\delta\vec{x}dV_R-\int_{\partial\mathscr{B}_R}\left(\vec{T}+\mathbf{S}^{\mathbf{T}}\vec{N}\right)\cdot\delta\vec{x}dA_R=0, \tag{1.37}$$

where the nominal stress tensor has been defined:

$$\mathbf{S}=J_G\mathbf{G}^{-1}\frac{\partial W}{\partial A}-J_Gp\mathbf{G}^{-1}\frac{\partial C}{\partial\mathbf{A}}. \tag{1.38}$$

The tensor $\mathbf{S}$ is known as the first Piola-Kirchhoff tensor. Eq.(1.37) represents the potential energy balance equation in variational form. To obtain the differential form, we consider arbitrary infinitesimal variations $d\vec{x}$ in Eq.(1.37) while satisfying the boundary conditions. By canceling out the terms, we obtain the following expression:

$$\left.\begin{array}{c}Div\mathbf{S}+\vec{B}=0\\C\left(\mathbf{A}\right)=0\end{array}\right\}\quad in\ \mathscr{B}_R, \tag{1.39}$$

$$\mathbf{S}^T\vec{N}=\vec{T}\quad on\ \partial\mathscr{B}_R. \tag{1.40}$$

In the case where the system is subject to hydrostatic pressure P, the tension at the edge $\overrightarrow{T}$ is given

by the formula:

$$\vec{T} = -J_F P \mathbf{F}^{-T} \vec{N} \tag{1.41}$$

Once the equilibrium equations have been established in their Lagrangian form, expressed in the coordinates of the reference configuration, they can be transformed into the Eulerian form using the current coordinates. To do so, we introduce the Cauchy tensor $\mathbf{T}$, which describes the stress field in the current configuration.

$$\mathbf{T} = {J_F}^{-1}\mathbf{F}\mathbf{S} = {J_A}^{-1}\mathbf{A}\frac{\partial \mathcal{W}}{\partial \mathbf{A}} - {J_A}^{-1}p\mathbf{A}\frac{\partial C}{\partial \mathbf{A}} \tag{1.42}$$

where $J_F = \det \mathbf{F}$ and $J_A = \det \mathbf{A}$. The Eulerian form referred by Eq.(1.39)-Eq.(1.40) is:

$$\left.\begin{array}{c} Div\mathbf{T} + \vec{b} = 0 \\ C\left(\mathbf{A}\right) = 0 \end{array}\right\} \quad in\ \mathscr{B}_C, \tag{1.43}$$

$$\mathbf{T}\vec{N} = \vec{t} \quad on\ \partial\mathscr{B}_C, \tag{1.44}$$

where $\vec{b}$ and $\vec{t}$ are respectively the volume and surface forces in the current configuration $\mathscr{B}_C$ and $\vec{n}$ denotes the unit vector, directed outwards and normal to the surface $\partial\mathscr{B}_C$. The operators Div and div denote the divergence of a tensor in the reference and current coordinates, respectively.

Finally, we can mention the existence of the second Piola-Kirchhoff tensor, which is a Lagrangian measure of the stress field.

$$\sigma = \mathbf{S}\mathbf{F}^{-T} = J_F \mathbf{F}^{-1}\mathbf{T}\mathbf{F}^{-T}. \tag{1.45}$$

In conclusion, the Cauchy stress represents the force exerted on a deformed area in the deformed configuration. The First Piola-Kirchhoff stress represents the force exerted on an undeformed area in the deformed configuration. The Second Piola-Kirchhoff stress mapped to undeformed configuration on the undeformed area. The more detailed explanations can be found in Ref.[92].

The incompressible material

If the material is incompressible, by virtue of Eq.(1.13), we have the following scalar relationship:

$$J_A = \det \mathbf{A} = 1. \tag{1.46}$$

Thus we have the:

$$J_F = \det \mathbf{F} = \det \mathbf{G} \equiv J_G. \tag{1.47}$$

Using the relationship in the Ref.[92]:

$$\frac{\partial \det \mathbf{A}}{\partial \mathbf{A}} = (\det \mathbf{A})\, \mathbf{A}^{-1}, \tag{1.48}$$

we obtain the following relations for the Nominal stress tensor (The nominal stress is the transpose of the first Piola-Kirchhoff stress) and the Cauchy tensor respectively:

$$\mathbf{S} = J_G \mathbf{G}^{-1} \frac{\partial \mathcal{W}}{\partial \mathbf{A}} - J_G p \mathbf{F}^{-1}, \tag{1.49}$$

$$\mathbf{T} = \mathbf{A} \frac{\partial \mathcal{W}}{\partial \mathbf{A}} - \mathbf{pI}. \tag{1.50}$$

Furthermore, it is worth noting that the invariant I_3, which is defined as the determinant of the right Cauchy-Green elastic deformation tensor, is always equal to 1. As a result, the energy density usually can be expressed only in terms of the invariants I_1 and I_2. This explains why the term I_3 is not present in common forms of energy functions, such as those shown in Eq.(1.29) and Eq.(1.30). In general, it is traditional to separate the isochoric (volume-preserving) part from the compressible part in the expression of the energy density function.

1.2.3 Mechanical morphology of biological tissues

In nature, plants exhibit a range of forms in different developmental stages and living conditions, such as sunlight, humidity, and temperature. Recent investigations have focused on various characteristics, including the growth of flowers [103, 104], plant leaves [105, 106, 107, 108], and specific types of unicellular green algae [109, 110]. Martine Ben Amar *et al.* [111] utilized the principle of minimizing the bending energies of both petals and veins to construct the shapes of sympetalous bell-shaped flowers with constant Gaussian curvature, successfully predicting their global shape. Fan Xu *et al.* [112] observed that lotus leaves floating on water typically experience short wavelength edge wrinkling that decays toward the center, while leaves growing above water morph into a global bending cone shape with long rippled waves near the edge. They developed mathematical models to account for the inhomogeneous differential growth of floating and free-standing leaves, accurately predicting the formation and evolution of their morphology. Different species of mushrooms also exhibit a range of morphologies. Xiaoyi Chen *et al.* [113] recently discovered that Amanita muscaria and Mycena chlorophos grow similarly, with their caps rapidly expanding outward and then turning upwards. However, only the latter develops a central depression in the cap. They used mathematical modeling to uncover the interplay between physics and biology that drives the emergence of these distinct morphologies. Figure (1.9) showcases some natural forms and their corresponding simulation results.

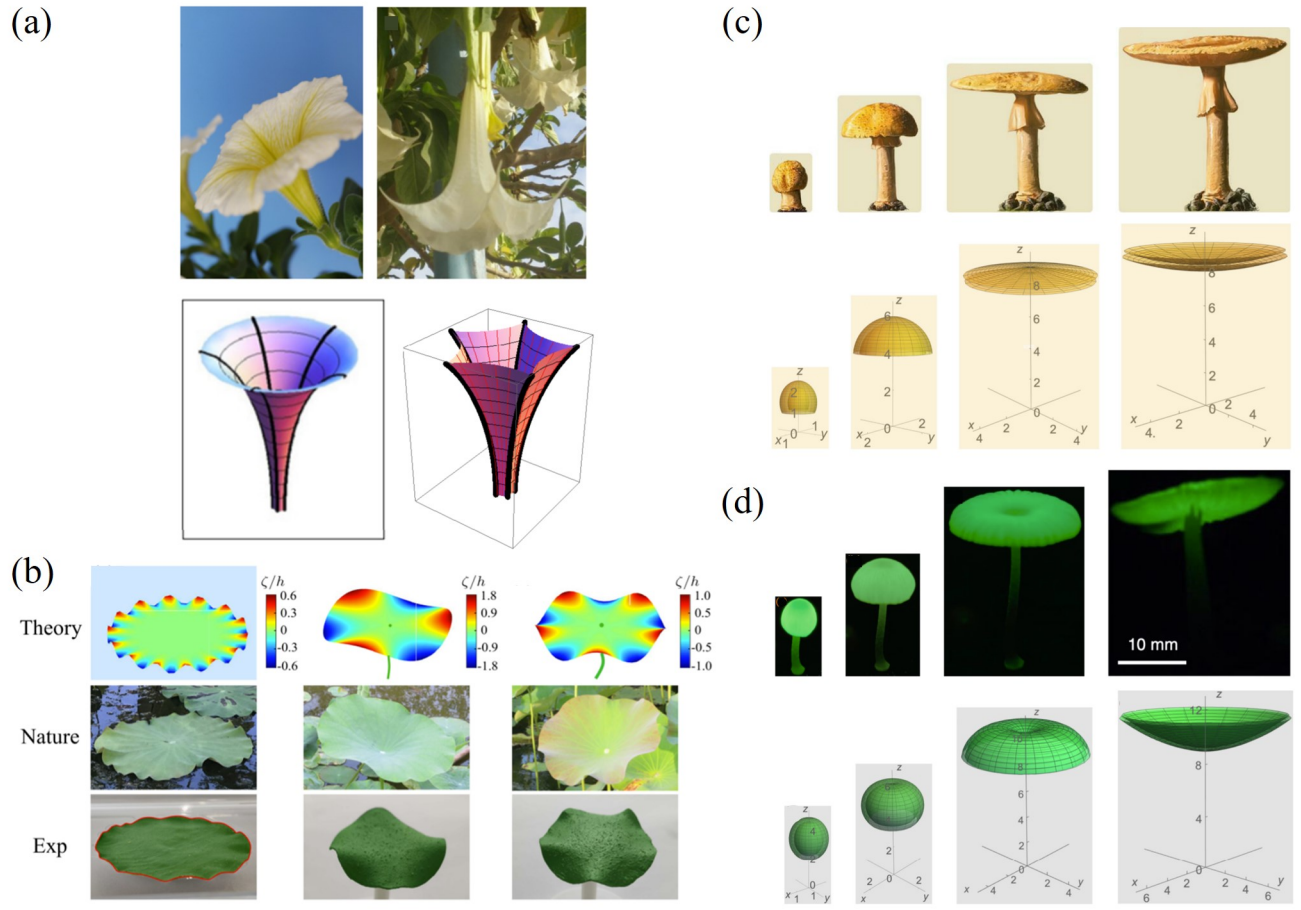

Figure 1.9 – *(a) Above: A surfinia (Paris) and An Angel's trumpet (brugmansia) (Morocco). Below: their simulation images [111]. (b) Morphological comparison of different types of lotus leaves. Left: A floating lotus leaf grows with short waves along the edge (the wavy edge is highlighted by red color in experiments). Medium and right: suspended lotus leaves morph into long-wavelength ripples [112]. (c) Above: The cap morphological development of the mushroom Amanita muscaria. Below: Simulation images of different parameters. (d) Above: The cap morphological development of the mushroom Mycena chlorophos. Below: Simulation images of different parameters [113].*

The organs and tissues of animals also exhibit a diverse range of morphologies, which are closely linked to their functions. Researchers have conducted numerous studies on various objects in this context. For example, investigations have focused on the morphogenesis of the brain cortex [54, 114, 115, 116, 117], the patterns of fingerprints [118, 119], the surface of the oesophageal mucosa [33], and the intestinal pattern [2, 120, 121, 122, 123].

For instance, Bo Li *et al.* developed a biomechanical model to investigate the relationship between mucosal morphogenesis and volume growth in physiological and pathological contexts. Through theoretical analysis and numerical simulations, they revealed the key features of mucosal crumpling in the spherical gastric sinus [33]. Another study by Du Y. *et al.* [51] proposed a modified augmented theory to determine growth-induced residual stresses and pattern evolution in stratified arteries. They applied their approach to aging bilayered human aortae, considering experimentally determined residual stress distributions and quantifying their effect. These studies highlight the importance of understanding the morphology and function of organs and tissues in biological and medical research, providing valuable insights into their development and behavior.

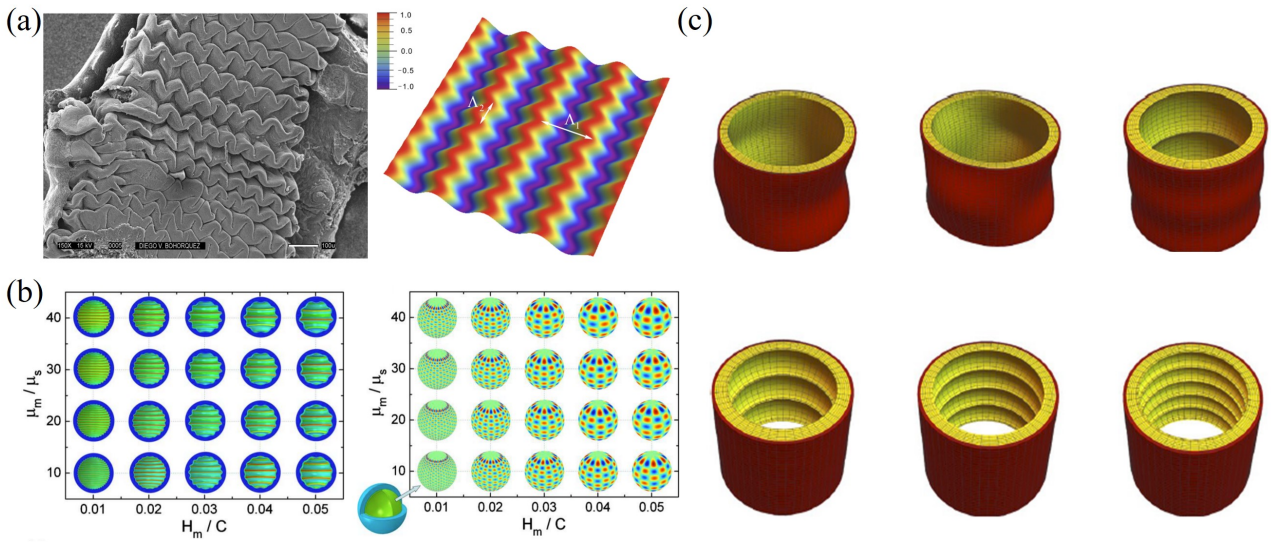

Figure 1.10 – *(a) Left: Zig-zag patterning by the previllus ridges in the jejunum turkey embryos, courtesy of D. Bohórquez. Right: Analytical prediction results [2] (b) Color online Diagrams of the critical wrinkling patterns: Left: axisymmetric pattern and Right: a possible symmetric breaking of the mucosal surface (mucosal thickness H_m/C and the modulus ratio μ_m/μ_s) [124]. (c) Simulated images of aged bilayer human aorta under different parameters [51].*

1.2.4 Applications and implications

Understanding the relationship between growth and mechanics is also of considerable importance for medical research, such as tumor treatment [125, 126, 127, 128, 129], and wound recovery [130, 131]. Giulio Lucci *et al.* [129] proposed a mathematical multiphase model, which allows for evaluating the impact of the growing tumor mass on the surrounding healthy tissue, quantifying the displacements, deformations, and stresses induced by its proliferation. Wu and Ben Amar [131] explored a growth model in the finite elasticity of a bilayer surrounding a circular wound, only the interior one being proliferative and contractile. They further discussed the occurrence of irregular wound geometry generated by stresses and show quantitatively that it is the result of a combination of stiffness, and wound size, ultimately weakened by actin cables.

Geometrically frustrated solids with non-Euclidean reference metrics are gaining significance in technological applications due to their ability to acquire incompatible target configurations through the surface accretion of masses. Zurlo *et al.* [132, 133, 134] proposed a theory of inelastic surface growth, in which the reference configuration is incompatible and exists only in non-Euclidean space, resulting in inevitable residual stresses during the growth process of a three-dimensional surface. This novel model of inelastic surface growth not only provides a comprehensive understanding of residual stresses and history dependence but also establishes a critical link between morphology and mechanics. Moreover, the proposed model can be used to guide advanced technologies such as $3D$ printing [132] and bionic $4D$ printing [135], as illustrated in Figure 1.11.

In addition, the research of biological soft tissues has great practical applications, such as soft robotics for specific functions, additive manufacturing, etc.

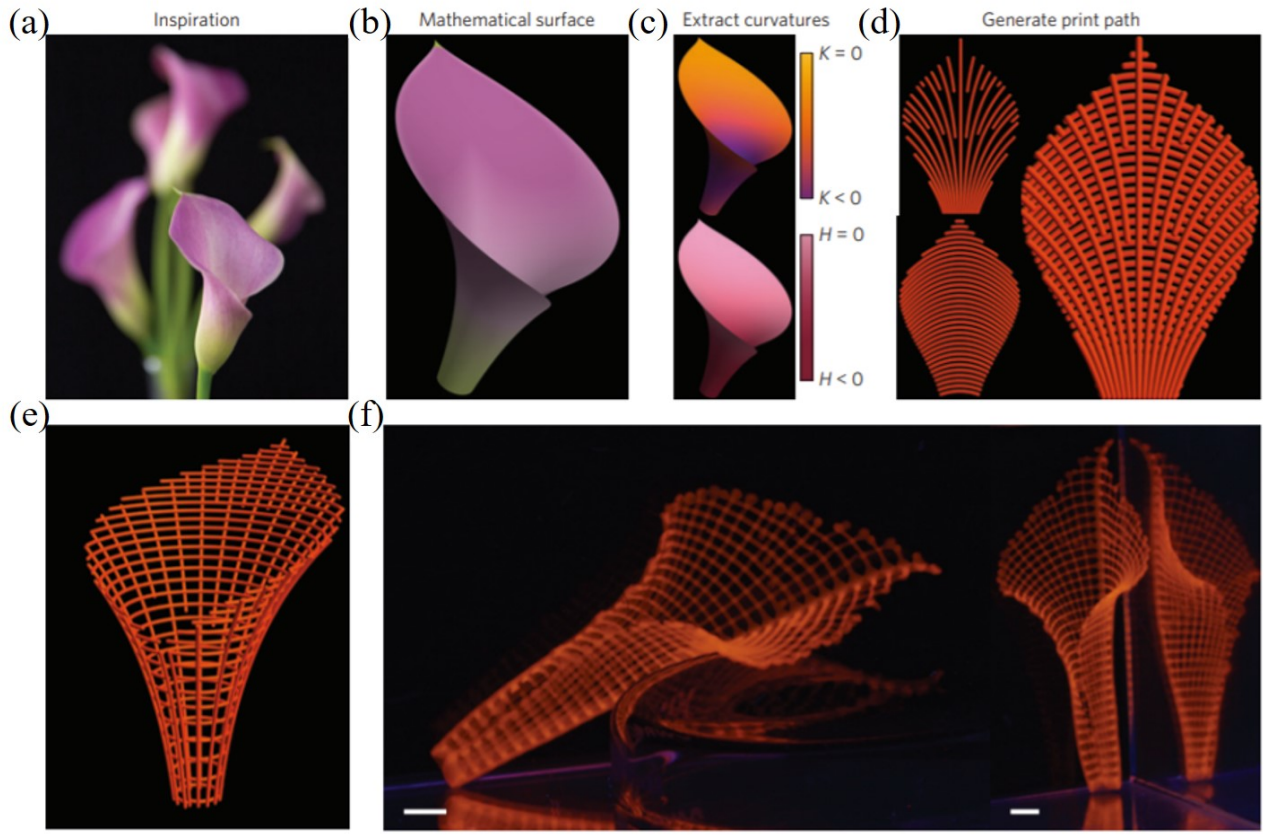

Figure 1.11 – *Simulated image of a 4D print of a biomimetic structure. (a) A native calla lily. (b) Mathematically generated model of the flower. (c) A well-defined curvature of the flower. (d) Print path. (e) The geometry of the flower on swelling. (f) Same gradients of curvature as the predicted model. The nozzle size is* $410\mu m$ *(scale bars,* $5mm$*) [135].*

1.3 Discussions

In summary, the morphological evolution of biological tissues regulated by mechanical stress during growth is of great significance in biological systems. In recent years, this research field has gradually attracted the attention of researchers, and more and more of them have explored the law of its mechanical behavior, physical mechanism and related applications from the aspects of experiment, theory and simulation. These studies contribute to a deep understanding of related life processes from the molecular scale to the tissue scale and provide new ideas for disease diagnosis and treatment. However, due to the complexity and changeability of organisms and their environments, accurately predicting and capturing the behavior of biological tissues becomes a formidable challenge. Consequently, there is a pressing and essential requirement to tackle and unravel the numerous persisting unresolved complexities within this field of study. Therefore, this thesis mainly aims at the growth and morphogenesis process of biological tissues, combining continuum mechanics and biomathematics methods, through theoretical analysis and numerical simulations, to study several key issues of its morphology formation, which provide a new physical understanding of various physiological processes.

The foundational growth theories introduced in this chapter will find application in the subsequent chapters of this thesis, where two distinct studies will be explored. The first study pertains to the ex-

amination of the conformational evolution of stress-free growth in planar leaves. Notably, despite the intricate internal structure of planar leaves, it is remarkable that they undergo growth without generating any elastic stresses. The second study focuses on the elongation of the *C. elegans* embryo. While experimental techniques have contributed to characterizing the complete elongation process and the influential factors such as acto-myosin and muscle networks, there remains a need to investigate the underlying mechanisms of elongation and deformation through theoretical studies.

Part I

The study of the morphology of leaves during growth

In this part, we investigate morphological transformations in two-dimensional stress-free growth, and the methodology and analysis can be extended to other similar biological organs or tissues. Our idea origins from recent studies [3] and the intuition of D'arcy Thompson [40], which is to find the regularity of shape transformation during stress-free growth. Then, we obtain the conclusion that stress-free growth follows a conformal mapping by the energy minimization principle. Finally, the main characteristics of some natural plant leaves are recovered by our method, which also elucidates the physical mechanisms that generate the complex morphology of two-dimensional soft tissues. In addition, we have made preliminary explorations of extending this method to study leaves with buckling morphology.

Chapter 2

Stress-Free growth of 2-D samples: application to leaves

This chapter focuses on the morphological evolution problem of 2D stress-free growth, and is taken mainly from the paper co-authored with Martine Ben Amar in Ref. [136] (Appendix A). The research background and current state are detailed in section 2.1, then the follow-up research and applications are presented in section 2.2 and 2.3, and the conclusion in section 2.3.

2.1 2D stress-free growth based on circular geometry

As we mentioned in the chapter 1, most studies in growth theory are based on multiplicative decomposition [38], i.e. the system is initially in a stress-free configuration and is first transformed into a virtual state containing holes and overlaps. In the second step, the integrity of the virtual state is restored by an elastic process that eventually leads to the current configuration. Recently, Hui-Hui Dai and his colleagues [3] have proposed that the change of geometric shape is only induced by the volumetric growth G without the generation of elastic stresses during the growth process. However, their solution was limited the growth geometry to circular shapes, and we have undertaken the problem more in-depth to solve more complex geometry.

Xiaoyi Chen *et al.* [3] suppose that the growth metric $\mathbf{M} = \mathbf{G}^T\mathbf{G} = \mathbf{U}^2$ has eigenvalues $({\mu_1}^2, {\mu_2}^2)$ $(\mu_1, \mu_2 > 0)$ and associated orthonormal eigenvectors $(\mathbf{p}^1, \mathbf{p}^2)$. Then the growth tensor $\mathbf{G}$ has the polar decomposition [92, 137]:

$$\mathbf{G} = \mathbf{QU} = \mu_1 \mathbf{q}^1 \otimes \mathbf{p}^1 + \mu_2 \mathbf{q}^2 \otimes \mathbf{p}^2 \tag{2.1}$$

where $\mathbf{q}^1 = \mathbf{Q}\mathbf{p}^1$ and $\mathbf{q}^2 = \mathbf{Q}\mathbf{p}^2$ and $\mathbf{Q}$ is a rotation tensor. For the purpose of analysis, they chose the appropriate orthogonal curvilinear coordinates (Θ_1, Θ_2) in the initial configuration R_0 such that the cotravariant base vectors $\{\mathbf{g}^1, \mathbf{g}^2\}$ have the same directions as $\{\mathbf{p}^1, \mathbf{p}^2\}$, i.e., $\mathbf{p}^i = \frac{\mathbf{g}^i}{|\mathbf{g}^i|},\ i = 1, 2$, $\mathbf{g}^i \cdot \mathbf{g}_j = \delta^i_j$, and $\mathbf{g}_j = \frac{\partial \mathbf{X}}{\partial \Theta_j}, j = 1, 2$. $\mathbf{X}$ is the position vector in R_0 and $\{\mathbf{g}^1, \mathbf{g}^2\}$ are the covariant base vectors under the system (Θ_1, Θ_2). For the virtual state R_g, the base vectors are chosen to be $\{\mathbf{q}^1, \mathbf{q}^2\}$.

From the above equations, the growth tensor can be rewritten as:

$$\mathbf{G} = \lambda_1 \mathbf{q}^1 \otimes \mathbf{g}^1 + \lambda_2 \mathbf{q}^2 \otimes \mathbf{g}^2,\ \lambda_i = \mu_i / \left|\mathbf{g}^i\right|,\ i = 1, 2 \tag{2.2}$$

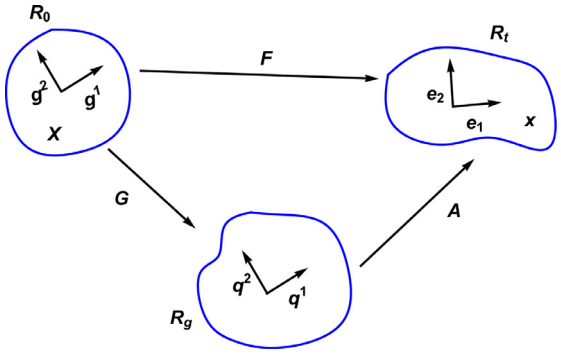

Figure 2.1 – *The decomposition of the deformation gradient* $\mathbf{F} = \mathbf{AG}$. R_0 *is the initial configuration with the initial position vector* $\mathbf{X}$, R_g *is the virtual stress-free state and* R_t *is the current configuration with the current position vector* $\mathbf{x}$. *The orthogonal base vectors* $\{\mathbf{g}^1, \mathbf{g}^2\}$, $\{\mathbf{q}^1, \mathbf{q}^2\}$ *and* $\{\mathbf{e}^1, \mathbf{e}^2\}$ *in three different configuration. [3]*

The local orthogonal (rotation) tensor A can be expressed in the form of:

$$\mathbf{A} = \cos\alpha \mathbf{e}_1 \otimes \mathbf{q}^1 + \sin\alpha \mathbf{e}_1 \otimes \mathbf{q}^2 - \sin\alpha \mathbf{e}_2 \otimes \mathbf{q}^1 + \cos\alpha \mathbf{e}_2 \otimes \mathbf{q}^2 \tag{2.3}$$

where $\{\mathbf{e}_1, \mathbf{e}_2\}$ are the rectangular base vectors in the current configuration R_t, and the position vector is $\mathbf{x} = x\mathbf{e}_1 + y\mathbf{e}_2$. So, the deformation gradient tensor takes the form:

$$\mathbf{F} = \lambda_1 \cos\alpha \mathbf{e}_1 \otimes \mathbf{g}^1 + \lambda_2 \sin\alpha \mathbf{e}_1 \otimes \mathbf{g}^2 - \lambda_1 \sin\alpha \mathbf{e}_2 \otimes \mathbf{g}^1 + \lambda_2 \cos\alpha \mathbf{e}_2 \otimes \mathbf{g}^2 \tag{2.4}$$

And the deformation gradient tensor can be expressed as another form by definition:

$$\mathbf{F} = \frac{\partial \mathbf{x}}{\partial \mathbf{X}} = \frac{\partial \mathbf{x}}{\partial \Theta^j} \otimes \mathbf{g}^j = \frac{\partial x}{\partial \Theta^1}\mathbf{e}_1 \otimes \mathbf{g}^1 + \frac{\partial y}{\partial \Theta^1}\mathbf{e}_2 \otimes \mathbf{g}^1 + \frac{\partial x}{\partial \Theta^2}\mathbf{e}_1 \otimes \mathbf{g}^2 + \frac{\partial y}{\partial \Theta^2}\mathbf{e}_2 \otimes \mathbf{g}^2 \tag{2.5}$$

Comparing the two forms of $\mathbf{F}$, they obtained the governing equations for solving (x, y):

$$\frac{\partial x}{\partial \Theta_1} = \lambda_1 \cos\alpha,\ \frac{\partial x}{\partial \Theta_2} = \lambda_2 \sin\alpha,\ \frac{\partial y}{\partial \Theta_1} = -\lambda_1 \sin\alpha,\ \frac{\partial y}{\partial \Theta_2} = \lambda_2 \cos\alpha. \tag{2.6}$$

Assuming that (x, y) are C^2-smooth:

$$\frac{\partial^2 x}{\partial \Theta_1 \partial \Theta_2} = \frac{\partial^2 x}{\partial \Theta_2 \partial \Theta_1},\ \frac{\partial^2 y}{\partial \Theta_1 \partial \Theta_2} = \frac{\partial^2 y}{\partial \Theta_2 \partial \Theta_1} \tag{2.7}$$

Then, applying Eq.(2.5) in the above equation:

$$\begin{aligned} &\cos\alpha \frac{\partial \lambda_1}{\partial \Theta_2} + \sin\alpha \left(-\lambda_1 \frac{\partial \alpha}{\partial \Theta_2}\right) = \cos\alpha \left(\lambda_2 \frac{\partial \alpha}{\partial \Theta_1}\right) + \sin\alpha \frac{\partial \lambda_2}{\partial \Theta_1}, \\ &\cos\alpha \left(\lambda_1 \frac{\partial \alpha}{\partial \Theta_2}\right) + \sin\alpha \frac{\partial \lambda_1}{\partial \Theta_2} = \cos\alpha \left(-\frac{\partial \lambda_2}{\partial \Theta_1}\right) + \sin\alpha \left(\lambda_2 \frac{\partial \alpha}{\partial \Theta_1}\right), \end{aligned} \tag{2.8}$$

the above equations are equivalent to

$$\lambda_2 \frac{\partial \alpha}{\partial \Theta_1} = \frac{\partial \lambda_1}{\partial \Theta_2},\ -\lambda_1 \frac{\partial \alpha}{\partial \Theta_2} = \frac{\partial \lambda_2}{\partial \Theta_1}. \tag{2.9}$$

Eq.(2.9) provides the governing equations for solving α. Further, they assume that α is also C^2-smooth:

$$\frac{\partial^2 \alpha}{\partial \Theta_1 \partial \Theta_2} = \frac{\partial^2 \alpha}{\partial \Theta_2 \partial \Theta_1}, \tag{2.10}$$

then get the one of constraints:

$$\frac{\partial}{\partial \Theta_1}\left(-\frac{1}{\lambda_1}\frac{\partial \lambda_2}{\partial \Theta_1}\right) = \frac{\partial}{\partial \Theta_2}\left(-\frac{1}{\lambda_2}\frac{\partial \lambda_1}{\partial \Theta_2}\right), \tag{2.11}$$

another constraint is:

$$\frac{\partial \lambda_1}{\partial \Theta_2} \neq 0 \quad or \quad \frac{\partial \lambda_2}{\partial \Theta_1} \neq 0, \tag{2.12}$$

which is the restriction on λ_1 and λ_2.

After a series of assumptions, this system is solved analytically and a family of growth functions with three parameters are obtained,

$$\alpha = \alpha\left(\Theta_1\right) = \int f_1\left(\Theta_1\right) d\Theta_1 + \alpha_0, \tag{2.13}$$

and

$$\begin{aligned} x &= \left(\int \lambda_2\left(\Theta_2\right) d\Theta_2 + d_0\right) \sin \alpha\left(\Theta_1\right) + C_1, \\ y &= \left(\int \lambda_2\left(\Theta_2\right) d\Theta_2 + d_0\right) \cos \alpha\left(\Theta_1\right) + C_2. \end{aligned} \tag{2.14}$$

where the function f_1 is arbitrary function of Θ_1, and α_0, d_0, C_1 and C_2 are constants.

Finally, five biological patterns were mimicked by varying the initial configurations and these three parameters. These morphologies are analogous to five biological patterns, such as the growth patterns of ferns, walnut shells, the skulls of the infant (simplified to 2D), stems of some bean plants, and water lily leaves. Partial real images or photos and mathematical images are shown in Fig.2.2.

2.2 Stress-free growth by conformal mapping

The study of Xiaoyi Chen *et al.* [3] on the morphological evolution of two-dimensional stress-free growth is presented in section 2.1, their derivation is rather technical, but if the Eq.(2.14) was be

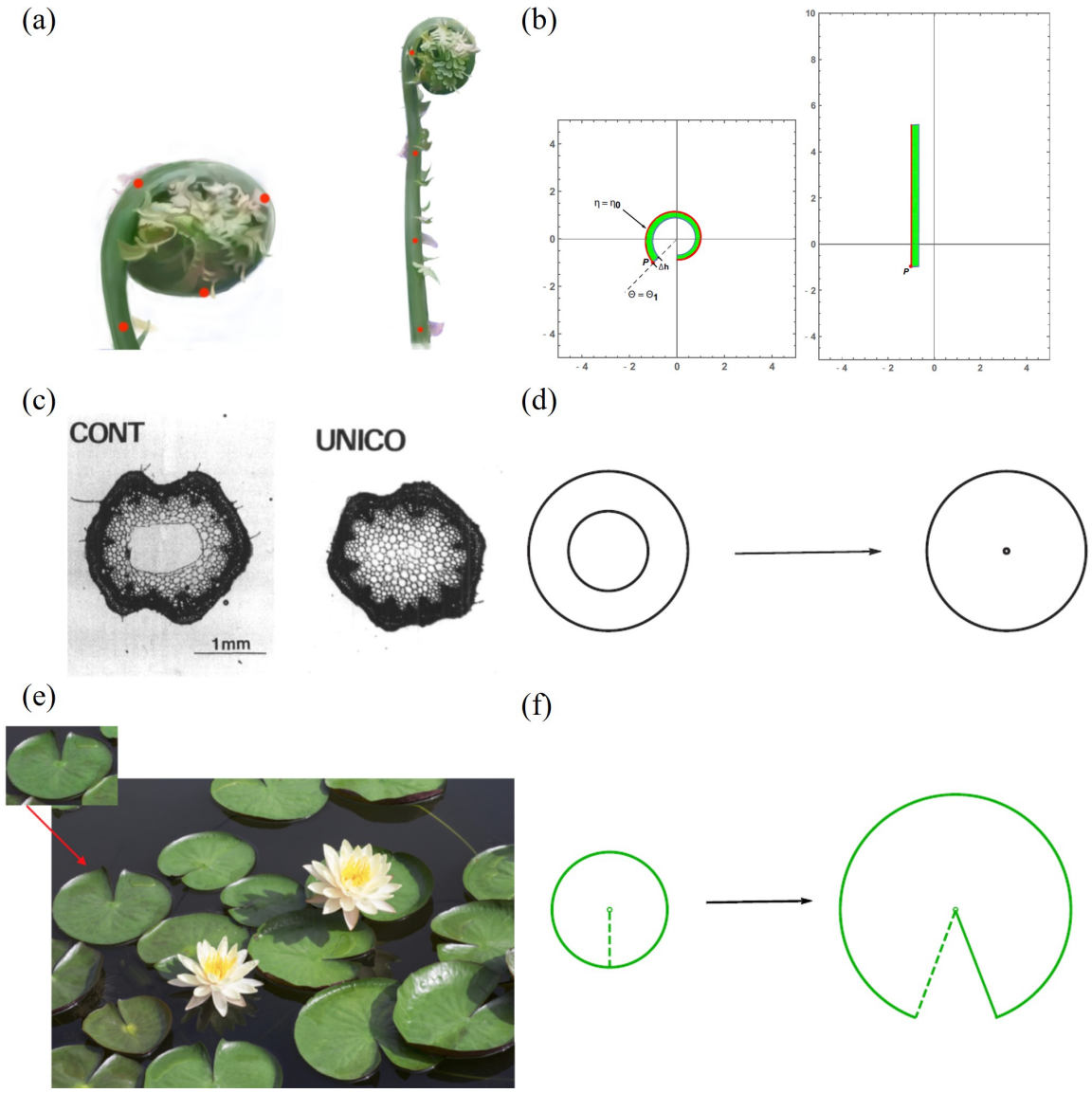

Figure 2.2 – *(a) Growth of a fern (see the red dot part). Left: Initial geometry of a fern. Right: Current configuration of the fern after growth. (b) Simulation of the straightening of the fern (red dot parts). Left: Initial geometry of the spiral strip. The red curve represents the spiral with* $\eta = \eta_0$ *and the dashed line shows* $\Theta = \Theta_1$*. Right: Current configuration of the circular strip after the spiral strip spreads out. (c) The growth patterns of two species of bean plants. From left to right, a species with a natural hollow stem is prevented from hollowing after the addition of uniconazole. (d) Growth patterns with varying inner radius: The anti-hollowing process. (e)The open angle on the leaf of the water lily. (f) The growth pattern mimics the open angle of the water lily leaf.*

simplified, we can obtain:

$$(x - C_1)^2 + (y - C_1)^2 = \left(\int \lambda_2 (\Theta_2)\, d\Theta_2 + d_0 \right)^2. \tag{2.15}$$

So, it is worth noting that their examples are based on initial circular geometry, and their examples (Fig.2.2) can also prove this conclusion.

Based on such result, we have intuited that the morphology of 2D stress-free growth should not be limited to circular geometries. When they solved the governing equations, we found that one of the

constraints is the assumption that λ only depends on Θ_2 and independently of Θ_1, it seems rigorous that may limit the final solution. Here, we have conducted an in-depth study to overcome this restriction and apply stress-free growth to a wider spectrum of the pattern biological tissues.

2.2.1 The original theoretical model

Let us reconsider the constraint equations, Eq. (2.11) and Eq. (2.12), we are no longer assume that λ only depends on Θ_2. We establish the following definition:

$$\lambda_1 = \lambda_2 = \lambda\left(\Theta_1, \Theta_2\right), \tag{2.16}$$

so, the Eq.(2.11) will be:

$$\frac{\partial}{\partial\Theta_1}\left(\frac{1}{\lambda}\frac{\partial\lambda}{\partial\Theta_1}\right) + \frac{\partial}{\partial\Theta_2}\left(\frac{1}{\lambda}\frac{\partial\lambda}{\partial\Theta_2}\right) = 0, \tag{2.17}$$

then, we obtain:

$$\frac{\partial^2 \log\left(\lambda\right)}{\partial{\Theta_1}^2} + \frac{\partial^2 \log\left(\lambda\right)}{\partial{\Theta_2}^2} = 0, \tag{2.18}$$

$$\log\left(\lambda\right) = F\left(\Theta\right) + \overline{F}\left(\overline{\Theta}\right), \tag{2.19}$$

where $\log\left(\lambda\right)$ is the real part of an holomorphic function of $\Theta = \Theta_1 + i\Theta_2$, the F is a priori an arbitrary function and the notation $\overline{F}$ means the complex conjugate of F.

According to the governing equation for α (Eq.(2.9)), we can get:

$$\frac{\partial\alpha}{\partial\Theta_1} = \frac{\partial\log\left(\lambda\right)}{\partial\Theta_2} \quad and \quad \frac{\partial\alpha}{\partial\Theta_2} = \frac{\partial\log\left(\lambda\right)}{\partial\Theta_1}, \tag{2.20}$$

we can combine into a unique equation of $\Theta = \Theta_1 + i\Theta_2$:

$$\frac{\partial\alpha}{\partial\Theta_1} - i\frac{\partial\alpha}{\partial\Theta_2} = i\left(\frac{\partial\log\left(\lambda\right)}{\partial\Theta_1} - i\frac{\partial\log\left(\lambda\right)}{\partial\Theta_2}\right). \tag{2.21}$$

Since the general relation:

$$\frac{\partial}{\partial\Theta_1} - i\frac{\partial}{\partial\Theta_2} = 2\frac{\partial}{\partial\Theta}, \tag{2.22}$$

we can get:

$$2\frac{\partial\alpha}{\partial\Theta} = 2i\frac{\partial\log\left(\lambda\right)}{\partial\Theta} \Rightarrow \alpha = i\left[F\left(\Theta\right) + \overline{F}\left(\overline{\Theta}\right)\right] + G\left(\overline{\Theta}\right), \tag{2.23}$$

If we want α is a real value, then we define $G\left(\overline{\Theta}\right) = -2i\overline{F}\left(\overline{\Theta}\right)$,

$$\alpha = i\left[F\left(\Theta\right) - \overline{F}\left(\overline{\Theta}\right)\right]. \tag{2.24}$$

Defining $z = x + iy$ and refer to governing equations Eq.(2.6) for x and y that we transform into:

$$\frac{\partial z}{\partial \Theta_1} = \lambda\left(\cos\alpha - i\sin\alpha\right) = \lambda e^{-i\alpha},\ \frac{\partial z}{\partial \Theta_2} = i\lambda\left(\cos\alpha - i\sin\alpha\right) = i\lambda e^{-i\alpha}, \tag{2.25}$$

Combining above two equations and replacing α and λ, we get:

$$\frac{\partial z}{\partial \Theta} = \lambda e^{-i\alpha} = e^{F(\Theta)+F\left(\overline{\Theta}\right)} e^{F(\Theta)-F\left(\overline{\Theta}\right)} \Rightarrow z = x + iy = \int_0^{\Theta} e^{2F(u)} du. \tag{2.26}$$

We deduce $F\left(\Theta\right)$ being given by:

$$F\left(\Theta\right) = \frac{1}{2}\log\left(\frac{dz}{d\Theta}\right) \tag{2.27}$$

So the λ can be obtained by:

$$\lambda = \sqrt{\frac{dz}{d\Theta}\frac{d\overline{z}}{d\overline{\Theta}}}. \tag{2.28}$$

Assuming that a possible shape as $z = z\left(\Theta\right)$, and solutions of x, y are obtained. Then, we can recover the value of λ, growth eigenvalues μ_1 and μ_2 and geometric gradient of the deformation. This result suggests that once we can find that the morphology of biological tissue before and after growth can be represented by $Z\left(\Theta\right)$ and $z\left(\Theta\right)$ respectively, i.e. a conformal mapping, and validated by some techniques, we can prove that is stress-free growth. This derivation process is followed by the method in the paper by Xiaoyi Chen *et al.* [3].

The concept of the conformal mapping

A conformal mapping also called a conformal map, conformal transformation, angle-preserving transformation, or biholomorphic map, is a transformation $w = f\left(z\right) = f\left(x + iy\right)$ that preserves local angles. Conformal mapping is extremely important in complex analysis, as well as in many areas of physics and engineering.

D'Arcy Thompson was a Scottish biologist who is the author of the book "On Growth and Form" [40]. In this book, he proposes that mathematical transformations perhaps can explain the morphology of macroscopic living species, as illustrated in Fig.2.3. This proposal provides the direction and ideas for our research.

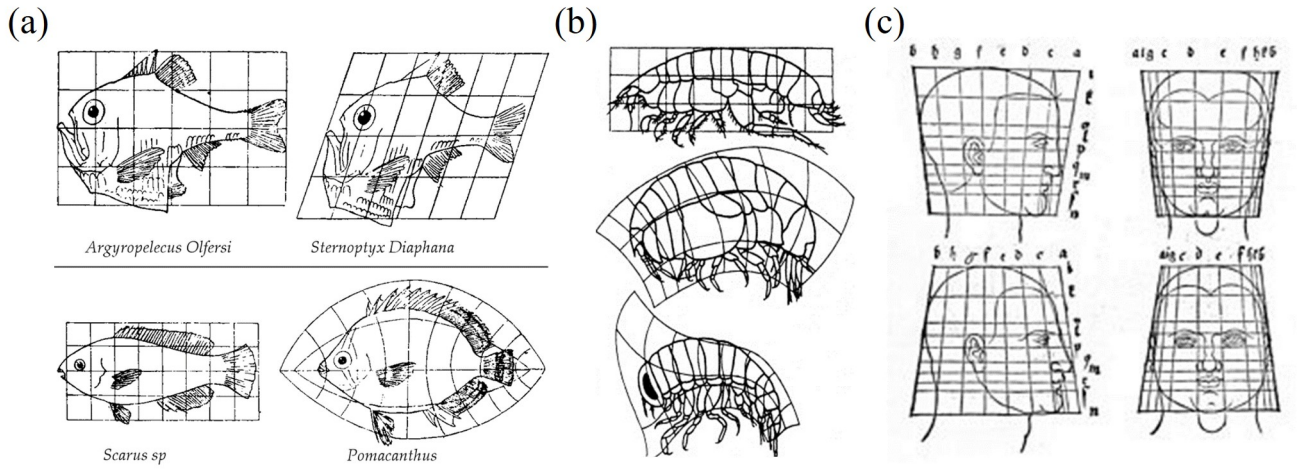

Figure 2.3 – *Morphological transformations of different organisms: (a) Fish, (b) Insect, (c) Human face.*

2.2.2 Minimizing the elastic energy by conformal growth

In the previous analysis, we found that if morphological changes follow conformal mappings during the growth, this process does not give rise to any stresses. Apart from deriving it using methods based on the general definitions, we arrived at the same conclusion by the definition of the complex plane. Furthermore, this conclusion was validated using flattened leaves.

We assume that the initial configuration is given by:

$$Z = X + iY = F_1(\Xi) = F_1(\mu + i\eta) \quad \text{so} \quad \Xi = \mu + i\eta, \tag{2.29}$$

where $i^2 = -1$, F_1 represents the mapping between cartesian coordinates and curvilinear coordinates of the interior of the leaf, μ and η are conformal coordinates. Then, we get the following Cauchy relations:

$$\frac{\partial \mu}{\partial X} = \frac{\partial \eta}{\partial Y} \quad \text{and} \quad \frac{\partial \mu}{\partial Y} = -\frac{\partial \eta}{\partial X}. \tag{2.30}$$

In morpho-elasticity, growth is represented by a tensor $\mathbf{G}$, we assume the tensor $\mathbf{G}$ is diagonal and reads:

$$\mathbf{G} = \begin{bmatrix} \frac{1}{p(\mu,\eta)} g(\mu,\eta) & 0 \\ 0 & p(\mu,\eta)\, g(\mu,\eta) \end{bmatrix}, \tag{2.31}$$

where $p(\mu,\eta)$ is the growth anisotropy coefficient, so our case reflects both isotropic and anisotropic growth, and $\det\mathbf{G} = g(\mu,\eta)^2$ is the volumetric growth at the time of observation. When the subject grows, we assume that the displacement of each point is given by the following mapping F_2 such that:

$$z = F_2(k(\mu) + il(\eta)), \tag{2.32}$$

where z represents the new coordinates (x, y). This mapping is not conformal but it gives for x and y

the relationship with the initial shape configuration such as:

$$\begin{cases} x = \frac{1}{2}\left[F_2\left(k\left(\mu\right)+il\left(\eta\right)\right)+\overline{F_2}\left(k\left(\mu\right)-il\left(\eta\right)\right)\right] \\ y = \frac{1}{2i}\left[F_2\left(k\left(\mu\right)+il\left(\eta\right)\right)-\overline{F_2}\left(k\left(\mu\right)-il\left(\eta\right)\right)\right] \end{cases} . \tag{2.33}$$

According to the main hypothesis of the morpho-elasticity theory, see Eq.(1.23) in Chapter1, the geometric gradient of deformation $\mathbf{F}$ and the elastic gradient of deformation tensor $\mathbf{A}$ are related by : $\mathbf{F} = \mathbf{AG}$ [38]. Written in these conformal coordinates, these tensors become:

$$\mathbf{F} = \frac{1}{|\partial_\Xi F_1|}\begin{bmatrix} \frac{\partial x}{\partial \mu} & \frac{\partial x}{\partial \eta} \\ \frac{\partial y}{\partial \mu} & \frac{\partial y}{\partial \eta} \end{bmatrix} \quad , \tag{2.34}$$

and

$$\mathbf{A} = \frac{1}{|\partial_\Xi F_1|}\begin{bmatrix} \frac{p}{g}\frac{\partial x}{\partial \mu} & \frac{1}{pg}\frac{\partial x}{\partial \eta} \\ \frac{p}{g}\frac{\partial y}{\partial \mu} & \frac{1}{pg}\frac{\partial y}{\partial \eta} \end{bmatrix}. \tag{2.35}$$

The first physical constraint concerns the incompressibility of the sample, $\det\mathbf{A} = 1$, which imposes:

$$\frac{\partial x}{\partial \mu}\frac{\partial y}{\partial \eta} - \frac{\partial x}{\partial \eta}\frac{\partial y}{\partial \mu} = g^2|\partial_\Xi F_1|^2. \tag{2.36}$$

In addition, stress-free configuration requires the cancellation of the first invariant,

$$I_1 = Tr\left(\mathbf{C}\right) - 2 = 0, \tag{2.37}$$

where $\mathbf{C}$ is right Cauchy tensor, $\mathbf{C} = \mathbf{A}^T\mathbf{A}$, then we derive:

$$p^2\left(\frac{\partial x}{\partial \mu}\right)^2 + p^2\left(\frac{\partial y}{\partial \mu}\right)^2 + \frac{1}{p^2}\left(\frac{\partial x}{\partial \eta}\right)^2 + \frac{1}{p^2}\left(\frac{\partial y}{\partial \eta}\right)^2 = 2g^2|\partial_\Xi F_1|^2 = 2\left(\frac{\partial x}{\partial \mu}\frac{\partial y}{\partial \eta} - \frac{\partial x}{\partial \eta}\frac{\partial y}{\partial \mu}\right). \tag{2.38}$$

A simple reorganization of Eq.(2.38) leads to:

$$\left(p\frac{\partial x}{\partial \mu} - \frac{1}{p}\frac{\partial y}{\partial \eta}\right)^2 + \left(p\frac{\partial y}{\partial \mu} + \frac{1}{p}\frac{\partial x}{\partial \eta}\right)^2 = 0, \tag{2.39}$$

so we get:

$$p\frac{\partial x}{\partial \mu} - \frac{1}{p}\frac{\partial y}{\partial \eta} = 0 \quad \text{and} \quad p\frac{\partial y}{\partial \mu} + \frac{1}{p}\frac{\partial x}{\partial \eta} = 0. \tag{2.40}$$

If $p = 1$ (isotropic growth), Eq.(2.40) recovers the Cauchy relations and implies that F_2 is an holomorphic function. If $p \neq 1$, an anisotropic growth process may also generate a stress free configuration. The

coefficient of anisotropy for a description ruled by F_2 (see Eq.(2.33)) is obtained with:

$$\begin{aligned} \frac{\partial x}{\partial \mu} &= k'(\mu)\,\frac{F_2{}' + \overline{F_2}'}{2}, \quad \frac{\partial x}{\partial \eta} = l'(\eta)\,i\frac{F_2{}' - \overline{F_2}'}{2}, \\ \frac{\partial y}{\partial \mu} &= k'(\mu)\,\frac{F_2{}' - \overline{F_2}'}{2i}, \quad \frac{\partial y}{\partial \eta} = l'(\eta)\,i\frac{F_2{}' + \overline{F_2}'}{2}, \end{aligned} \tag{2.41}$$

where the symbol prime ($'$) means the first derivative with respect to the natural variable as defined in Eq.(2.33). So introducing the values of the partial derivatives given by Eq.(2.41) into Eq.(2.40) gives:

$$p^2 = \frac{l'(\eta)}{k'(\mu)}. \tag{2.42}$$

We demonstrate that conformal(isotropic growth) or quasi-conformal(anisotropic growth) mappings have the advantage to eliminate the elastic stresses independently of the elastic material properties, among all mappings possible for the shape evolution of a 2D elastic sample.

2.3 Results and Applications

Our theoretical findings establish a connection between stress-free growth in two dimensions and conformal mapping. To further substantiate our conclusions, it is crucial to carefully select appropriate research subjects. A study conducted by K. Alim *et al.* was brought to our attention, they used the particle image velocity algorithm to measure the local displacement field of petunia and tobacco leaves during a period of time, which is rather consistent with their prediction results through conformal mapping, as shown in Fig.2.4. All of their data sets have very high scores of more than 92% correlation, ranging up to 97% for the top specimen. This experiment also measures the growth field, although the comparison with the conformal field is not as accurate as the displacement field, the findings of this research still show that the idea that the growth within the leaf blade follows conformal mapping is not baseless.

2.3.1 Simple experimental validation

In reality, the fact that the leaf is stress-free is rather astonishing since the leaf structure is complex see Fig.2.5. In particular, it "at least" contains two layers (epidermal and extracellular matrix). Examples of bilayer structures in mammal organs or tissues, such as our skin, the imaginal discs of wings, and the interior of the gray matter of the brain, residual stress that existed inside have been proved by many studies.

We conducted a simple cutting experiment, where mature and young leaves were cut in different positions and directions. This method of detecting internal stresses is very common, as shown in Fig. 1.4 (a)-(c) in Chapter 1, and it is also applicable to smaller scale like *C. elegans* embryos, which Vuong-Brender *et al.* cut using the laser to obtain internal stresses [138]. Our experiments were all done when the leaves were freshly removed from the plants to ensure their viability. After cutting, we did not

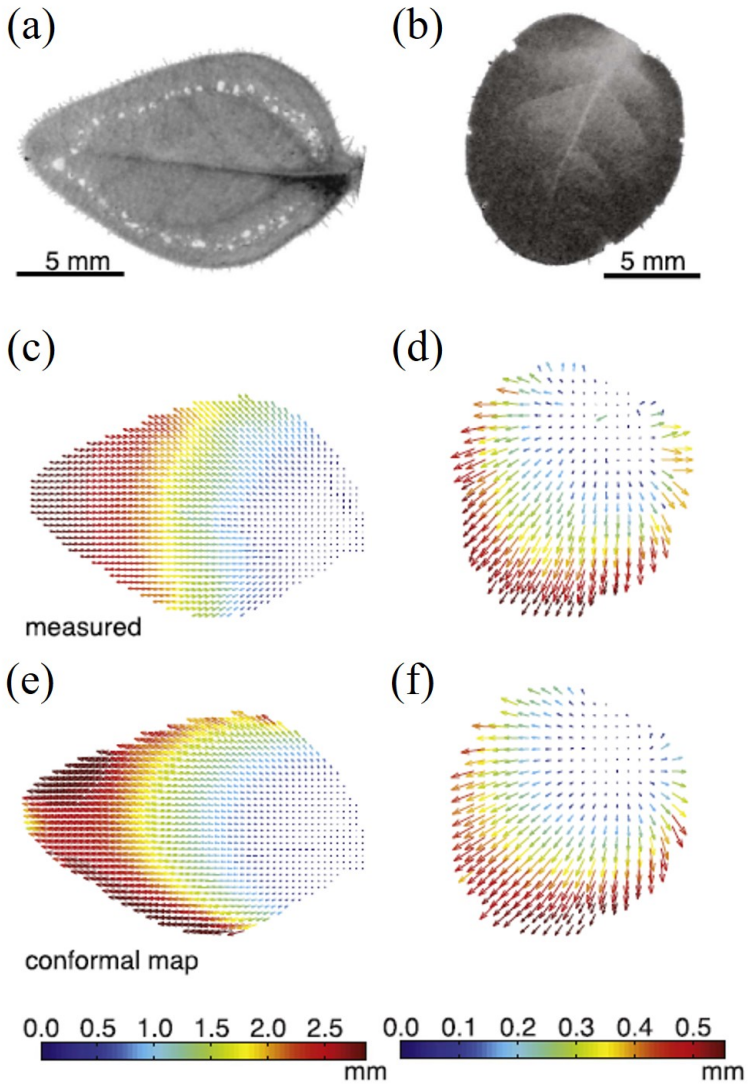

Figure 2.4 – *(a) Petunia leaf before undergoing* 12*h growth. (b) Tobacco leaf before undergoing* 12*h growth. (c), (d) particle image velocity algorithm. (e), (f) displacement fields calculated by conformal mapping.*

observe any opening angle, that is, there is no stress inside the planar leaf, which may be due to the complex internal structure of the leaf, the stress eliminated during growth. The experimental results are shown in Fig.2.6.

So, fresh planar leaves are good examples for our study, because they have no elastic stress inside, and almost no weight, and their shape can be easily represented by holomorphic functions. We recovered the growth process of several leaf species along with their main characteristics, including leaf tips, borders, and veins, even for the fenestration process in the *Monstera* leaf. For more details please refer to the paper [136] and its supplementary (Appendix A).

2.4 buckling leaves

In the previous sections, we recovered the stress-free growth of some leaves by means of conformal mapping. It is worth noting that the leaves we have studied are relatively flat leaves, but there are some

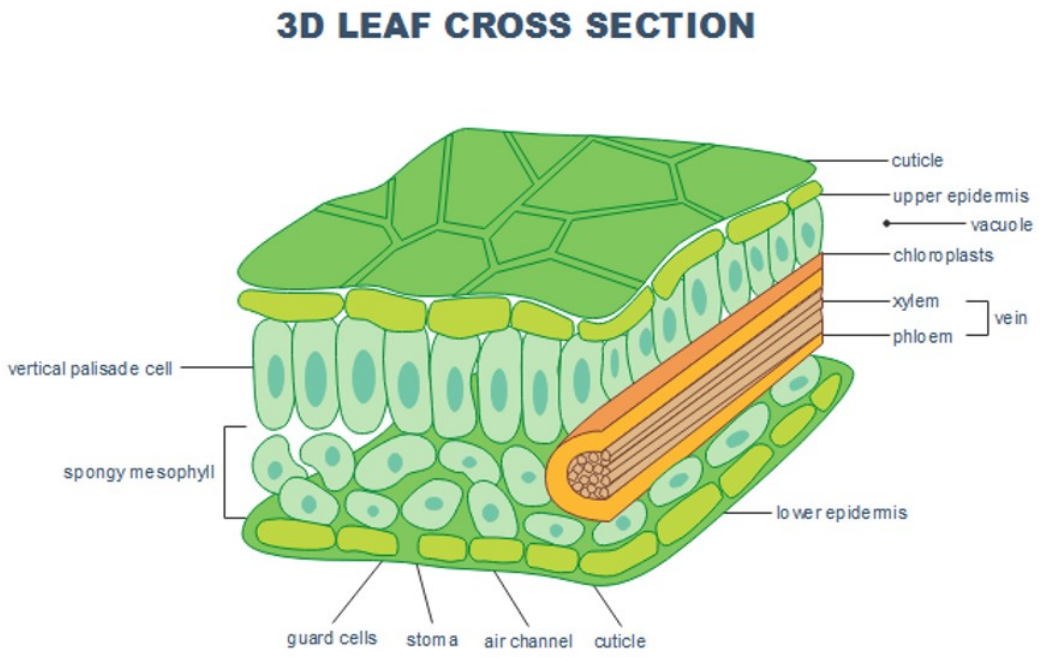

Figure 2.5 – *Cross section of a leaf*

Figure 2.6 – *Internal stress measurement experiment of leaves (opening angle experiment): (a) mature Monstera leaf, (b) young Monstera leaf.*

leaves that exist in nature that are in the crumpling or buckling state, which we will explore in this section.

The form of the undulating leaf blade is easily reminiscent of the morphological instability men-

tioned in Chapter 1, as shown in Fig.1.4 (d)-(f). The difference between the examples we have displayed before is that the undulating leaves are a thin layer. In recent years, researchers also have used the growth of thin layers to explain the diversity of shapes observed in nature, such as grass blades [108], algae [109] and mucosal epithelium [2], Drosophila tissues [139], Please see the Fig. 2.7.

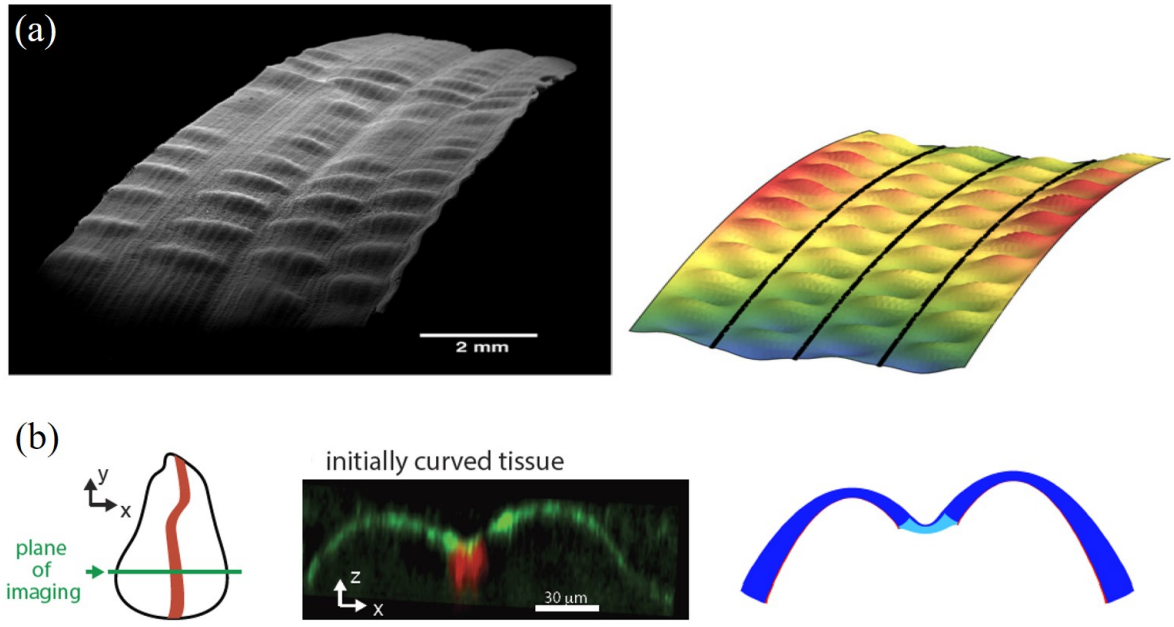

Figure 2.7 – *(a) Left: picture of a grass blade, courtesy of J.Dumais. Right side: representation of several destabilized Euler columns [108]. (b) Left: An xz cross section demonstrates the shape of an initially curved wing imaginal disc under the effect of a localized metalloprotease expression (in the red color region). Right: Cuts of the imaginal wing for the different FEM simulations with defect. The colors reflect the stiffness: red for the basal ECM, blue for the upper membrane and the cell layer, and cyan for the zone of the cell layer around the defect. Imaginal wing and defect with local change in stiffness in the cell layer [139, 140].*

2.4.1 Theoretical research basis

Firstly, it is necessary to introduce the Föppl–von Kármán equations, named after August Föppl and Theodore von Kármán, are a set of nonlinear partial differential equations describing the large deflections of thin flat plates. Martine Ben Amar and her colleagues [108, 109] based their work on the basic growth theory of finite elasticity and then introduced a hyperelastic thin plate subjected to loads and growth. The dimensionality of the problem was reduced by appropriate assumptions and the results show that growth is a source of mean and Gaussian curvature. The resulting equations were found to be an extension of the well-known FvK model, a powerful theory of buckling instability. This theory has been used to now to understand the growth of various flat structures of plants or epidermal tissues in biological systems [112], including all the studies mentioned in Fig.2.7.

Based on previous studies of stress-free growth, we consider that leaves with buckling morphology undergo two processes during the growth process, as shown in Fig.2.8. The leaves complete the first stage of growth without elastic stress and their deformation follows a conformal mapping, where forming their contours and main characteristics. And then, under the influence of growth and elastic stress, the

undulating morphological features appear.

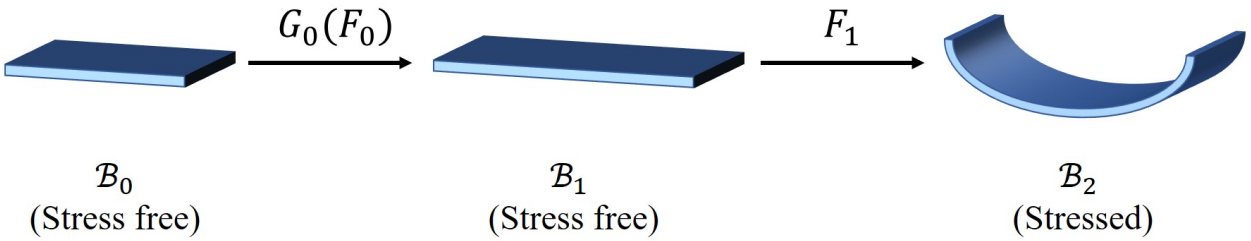

Figure 2.8 – *Initial configuration $\mathcal{B}_0$ undergo stress-free growth arrive at configuration $\mathcal{B}_1$, it becomes final configuration $\mathcal{B}_2$ under the influence of subsequent growth and elastic stress.*

2.4.2 Some examples

According to our idea, we have initially mimicked the buckling morphology on three different leaves, which is rather in agreement with their natural state, as shown in Fig.2.9.

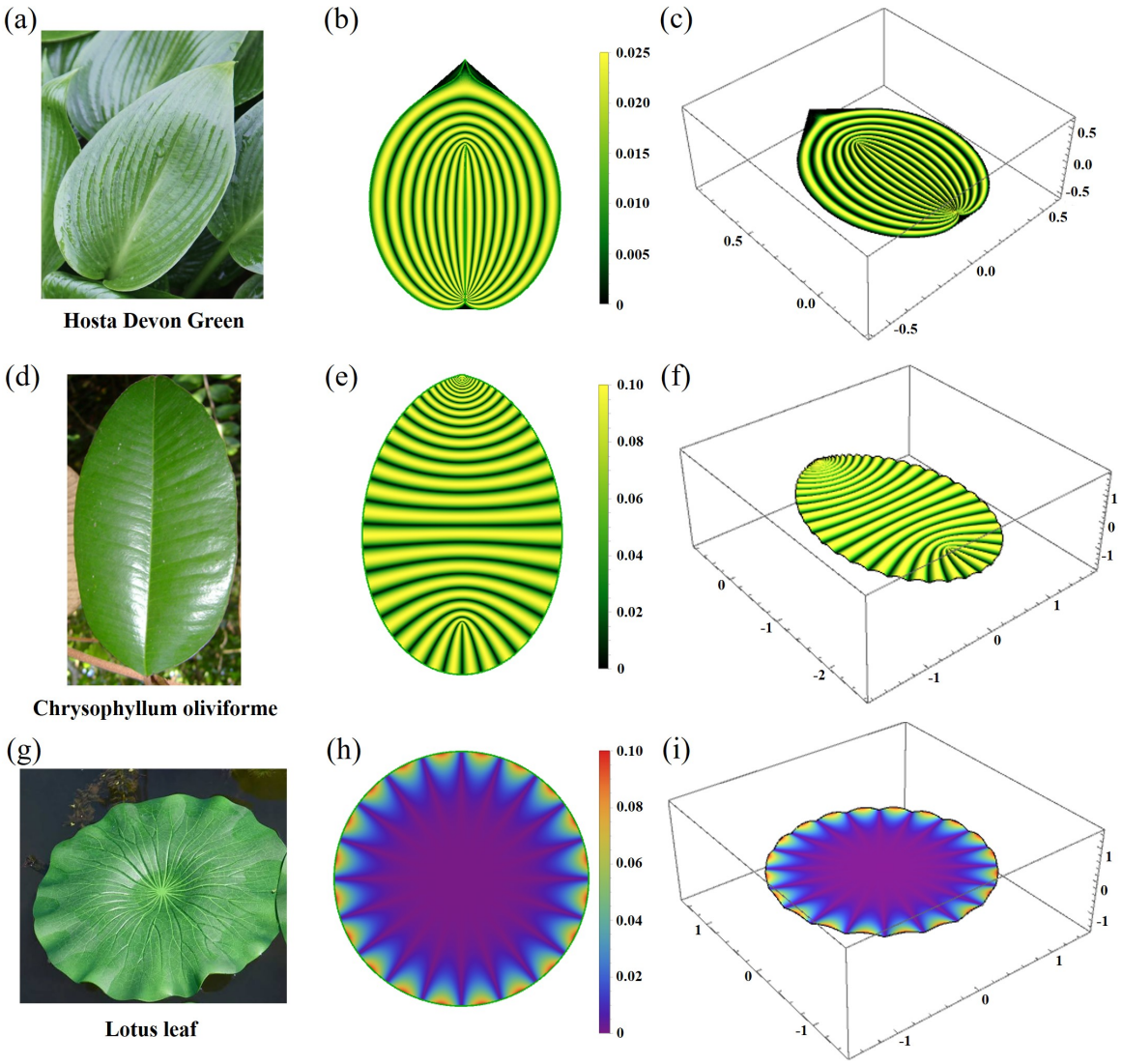

Figure 2.9 – *(a)(d)(g) correspond to the natural leaf, (b)(e)(h) is the top view of the corresponding mimicked leaf blades, and (g)(e)(h) is the 3-dimentional mimicked leaf blades.*

2.5 Discussion and conclusion

In this chapter, we first indicate that a conformal or quasi-conformal mapping between two planar configurations is generated by stress-free growth. This conclusion was then verified on naturally growing leaves such as the *Jujube* leaf, *Redbud* leaf, *Robinia pseudoacacia* leaf. We used conformal mapping to reconstruct the main characteristics of plant leaves such as tips (convex or concave or pointed), undulating borders and veins. Moreover, the process that generates the complex morphology of plant leaves are elucidated, such as the fenestration process in *Monstera* leaves. Our approach extracts information not only on cell proliferation, which is usually restricted to nutrient penetration but also on biological complexity such as tissue remodeling [141]. This formalism allows the accumulation of growth to be assessed in an isotropic or anisotropic case, combined with the mathematical images of leaf veins to establish a relationship with nutrient content.

The theoretical approach developed in this chapter can be extended to the study of morphogenesis in other curved complex structures, such as leaves with buckling morphology. We have a preliminary idea for this part of the work, but two problems still remain, one is how to extend the Fvk equations to the complex plane, and another is to obtain the biological reasons for the buckling morphology of the leaves in order to introduce growth and stress/strain correctly into the model. Furthermore, the findings of this study reveal a new pattern of stress-free growth of biological tissues, the study of the morphological evolution of stress-free growth can be applied not only to the growth of leaves but also to the morphogenesis of other biological tissues. Understanding the growth patterns of biological tissues can provide insights into the design of new bionic soft devices for growth and development.

Part II

An investigation into the embryonic elongation of *C. elegans*

The work of this part is dedicated to the modeling of the elongation in *C. elegans* embryos before hatching. The elongation is made possible via two active networks: the acto-myosin and the muscular network. A full understanding of the role of these muscles is highly significant considering that they are similar to any skeletal muscles of vertebrates. It has been experimentally shown that muscle activities play a crucial role in late elongation, but the intrinsic mechanism continues to puzzle scientists. Indeed, muscles are known to be contractile motors, and it is hard to imagine that a periodic bending due to their contractions performed successively on the left and right can lead to an elongation greater than 200%. We propose an analytical model based on the actual structure of worm biology. This model can recover all the deformations that occur during elongation including bending, twisting, and rotation and it also explains that acto-myosin and muscle contraction leads to a full elongation.

Chapter 3

Actomyosin contractions and early elongation

In this chapter, we focus on the early elongation of the *C.elegans* embryo, which is induced by the contractile forces generated by the actomyosin network. We will briefly introduce the background of its biological and mechanical research in section 3.1, and the simulation work is based on the previous theoretical modeling and results [4] in section 3.2. A new theoretical model is then presented in section 3.3, and during the early elongation, myosin activity is estimated by a dynamical model in section 3.4. The last section 3.5 is the conclusion and discussion.

3.1 Introduction

Over the past few decades, researchers have conducted many studies on complex biological tissues that are all subject to mechanical forces during embryonic development, such as the skin, the brain, and the interior of organs. But, smaller scales make it more difficult to identify and quantify the effects of mechanical stresses added to cellular processes (including division and migration) and tissue organization. For instance, distinct molecular motors, such as myosin II, which is connected to actin filaments and is most abundant during epithelial cell morphogenesis [142] and cell motility [143, 144, 145], may generate stresses independent of growth. The spatial localization and dynamic behavior of Myosin II have been shown to have a significant impact on the morphogenetic process [146] in both Drosophila [147, 148, 149, 150] and *C. elegans* embryo [4, 151, 152].

The embryonic elongation of *C. elegans* represents an attractive model of how matter can reorganize without experiencing a mass increase before eclosion. The embryo elongates along the anterior/posterior axis by four times [153] after the ventral enclosure, taking around 240 minutes to change from a lima-bean shape to an elongated worm shape. The short lifetime of the egg before hatching and its transparency make this system an ideal system for studying the forces that exist in the cortical epithelium or its vicinity. But unlike the embryonic development of Drosophila and Zebrafish, just a conspicuous epidermal elongation drives the entire morphogenetic process of *C. elegans*. There is neither cell migration nor division nor a discernible change in embryonic volume [151, 154]. There are two experimentally discovered driving mechanisms for the elongation, actomyosin contractility in epidermal seam cells, which appears to last throughout the entire elongation process, and muscular activity beneath the epider-

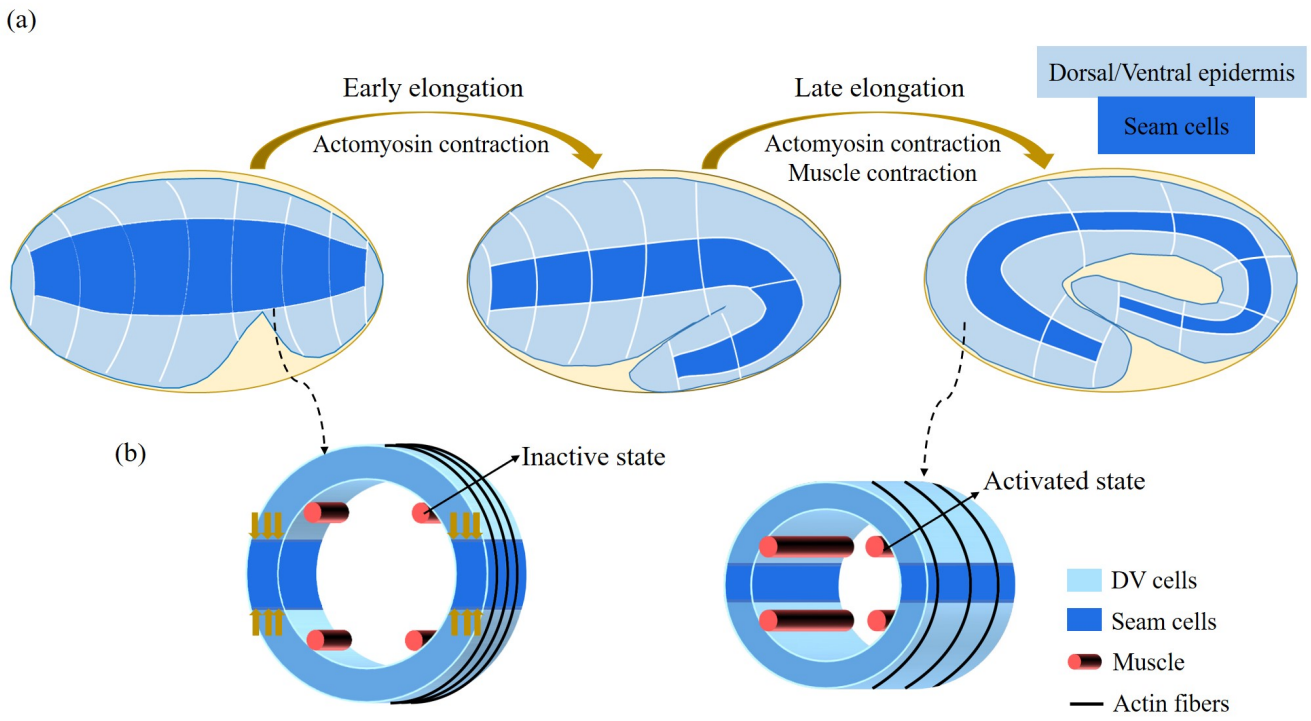

Figure 3.1 – (a) Overview of *C.elegans* embryonic elongation. Three epidermal cell types are found around the circumference: dorsal, ventral and lateral. (b) Schemes showing a *C.elegans* cross-section of the embryo. Small yellow arrows in the left image indicate the contraction force that occurred in the seam cell. Four muscle bands underneath the epidermis and actin bundles surround the outer epidermis.

mis, which begins after the $1.7 \sim 1.8$-fold stage. So, depending on the activation of muscle activity, the elongation process of *C. elegans* might be divided into two stages: early elongation and late elongation, Fig.3.1(A) displays the entire process [138].

3.1.1 Actomyosin activity

Myosin II is an ATP-dependent motor that uses actin as a substrate for bundle contraction and a range of cellular motility, and is generally composed of two heavy chains, two regulatory light chains, and two essential light chains [138, 155]. In *C.elegans*, the two heavy chains are named nmy-1 and nmy-2; the regulatory light chain and the essential light chain are named mlc-4 and mlc-5 respectively [152, 156]. The mechanical motility of myosin is the result of conformational changes in the globular domain. First, ATP-bound myosin binds to actin, and then the hydrolysis of ATP releases phosphate and causes a conformational change in the globular domain. The heavy chain replaces actin in this process. Finally, the replacement of ADP with ATP restores the initial conformation of the globular domain, leading to a renewed interaction between myosin and actin [157]. Myosin begins to walk on actin filaments by binding and rebinding. The binding of these myosin and actin filaments is known as the actomyosin network. Most of the tension or compression generated by actomyosin is responsible for the changes in epithelial morphology that occur during development. The mechanical properties of actomyosin depend on the activity of myosin, the structure of the network, etc. [158, 159, 160].

During morphogenesis, the actin network can drive changes in tissue morphology. In *C.elegans* fertilized eggs, the gradient in actin contractility drives large-scale cortical tension in the viscous cortex to generate anisotropic cortical flow to ensure effective polarization of *C.elegans* fertilized eggs [161]. In turn, this cortical flow causes actin filaments to align to form a furrow [162].

3.1.2 Early elongation of *C.elegans* induced by actomyosin contraction

Early elongation is the stage that occurs between the lima bean and 2-fold phases. During this stage, the epidermis starts to change shape, they shorten itself along the dorsal/ventral (D/V) direction and lengthen itself along the anterior/posterior (A/P) direction. Genetic and pharmaceutical research have demonstrated that actomyosin contractions are essential for early elongation [151, 163, 164, 165]. Treatment with actin polymerization inhibitor cytochalasin D prevents early elongation [151]. It is not difficult to distinguish between the two stages, since the muscle participation makes the embryo rather motile impeding any physical experiments such as laser ablation. However, the early elongation stage of the worm is rather static and this experiment can be performed and achieved during this period [138]. So, during the early elongation phase, researchers [138] obtained some experimental data on the length and circumference of the *C.elegans* in relation to the internal stresses. Our group investigated the role of the actomyosin network in the seam cells during the early elongation of *C. elegans* previously [4]. Based on the geometry of a hollow cylinder composed of four parts (seam and dorsal/ventral cells), a model involving the pre-stress responsible for the enclosure, the passive stress, and the active compressive ortho-radial stress due to acto-myosin network in the seam cells, quantitatively predict the early elongation ($\sim 70\%$ of the initial length).

3.2 Numerical simulation for early elongation

As previously alluded to, our group has undertaken a comprehensive examination of the early elongation stage of *C.elegans* through rigorous theoretical investigations as reported in [4]. Specifically, we proposed an innovative model of actively elongating material, which takes the shape of a hollow cylinder and incorporates pre-stress and passive stresses in a non-linear elasticity framework. Also in this model we consider the *C.elegans* epidermis as consisting of dorsal, ventral and seam cells. By integrating experimental data from laser ablation experiments, we were able to derive the relationship between the active stresses generated by actin-myosin and *C.elegans* elongation, thus providing valuable insights into the underlying mechanics of this fundamental biological process.

To verify the correctness of this relationship, we used finite element software (Comsol) to realize the early elongation process of the *C.elegans* under the same conditions and to obtain the relationship between active stress and elongation. We built a hollow cylinder model and divided it into four parts, two seam cell parts, and two D/V parts, as shown in Fig.3.2. All size and material parameters are the same with the previous research [4], the outer radius is $10\mu m$, the inner radius is $8\mu m$, and the height is $10\mu m$. The material chosen is hyperelastic and incompressible, and the energy function is defined by Eq.(4) of Ref. [4]. We assumed the unit of shear modulus as the value of the seam cell modulus, and the Dorsal/Ventral cell part as 1.44.

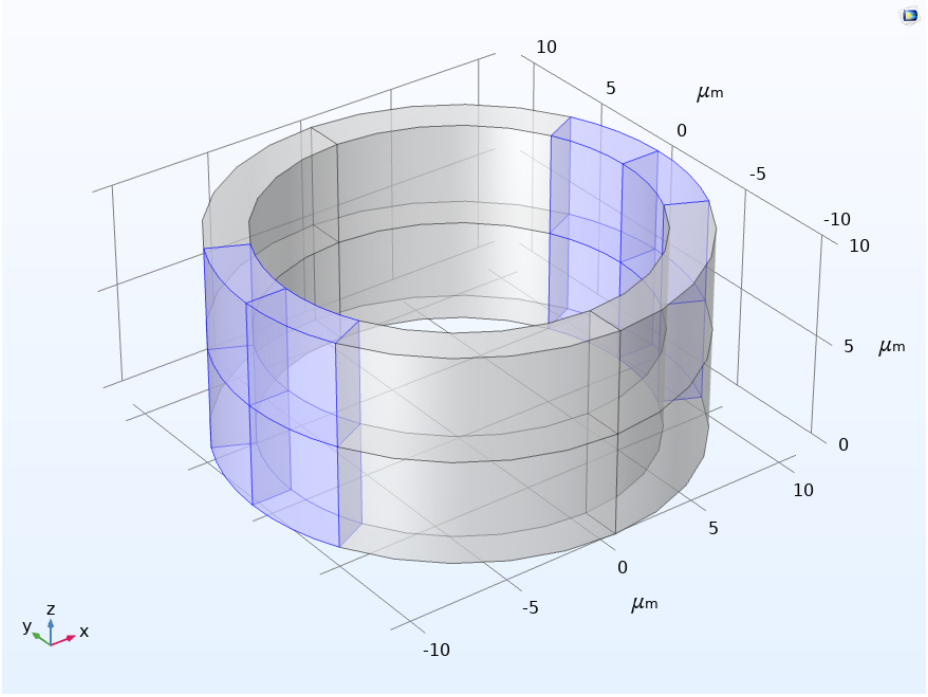

Figure 3.2 – Geometric model of *C.elegans*, Dorsal/Ventral parts are shown in grey, and seam cells parts are shown in blue.

Next, in order to fix the model and prevent rigid body displacements and rotations, we need to impose boundary conditions. We constrain the displacements in the z, y and x directions at the locations of the blue lines in Fig.3.3 (a), (b) and (c) respectively.

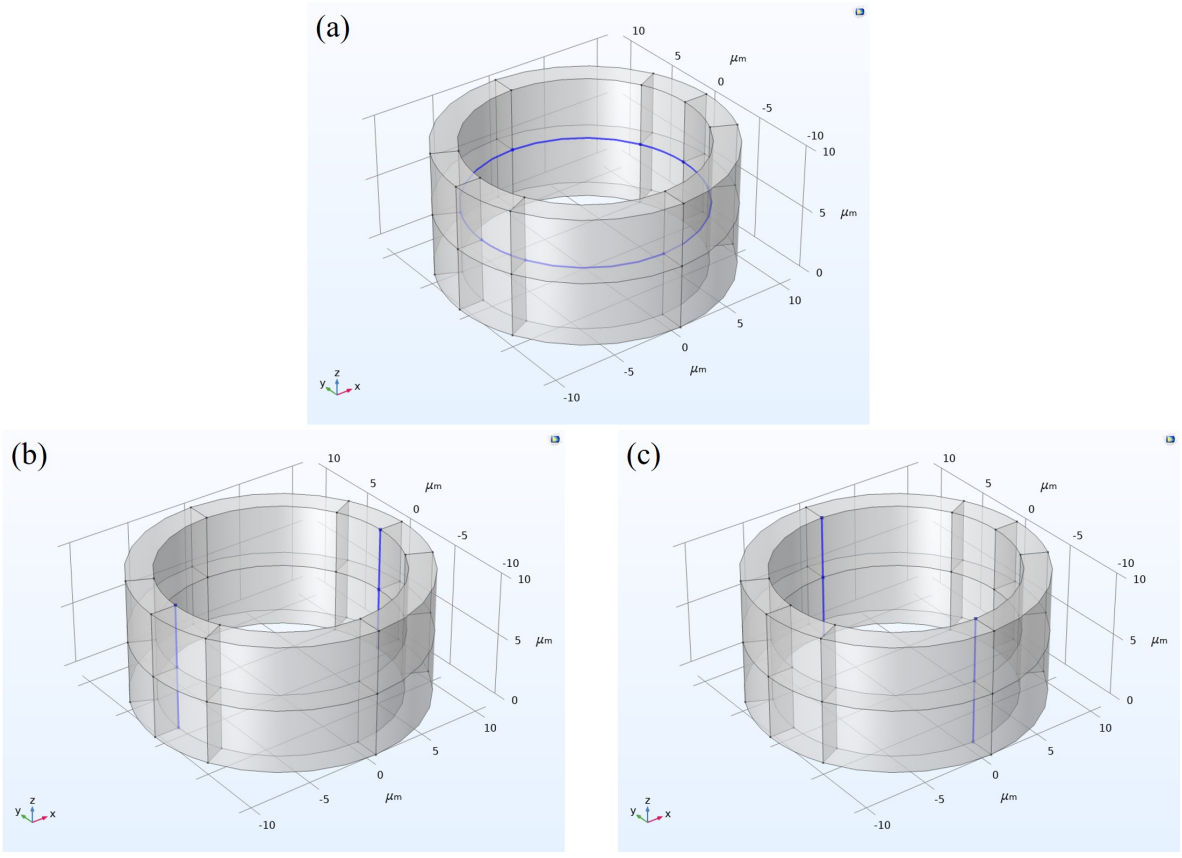

Figure 3.3 – Boundary conditions (The blue line shows the constraint position).

Then, we apply the active stress to the model $\sigma = \zeta\ Diag\,(0, 1, -1)$, ζ range from 0.1 to 1, which is in accordance with the active stress in the previous publications [4]. The deformation image is shown in Fig.3.4.

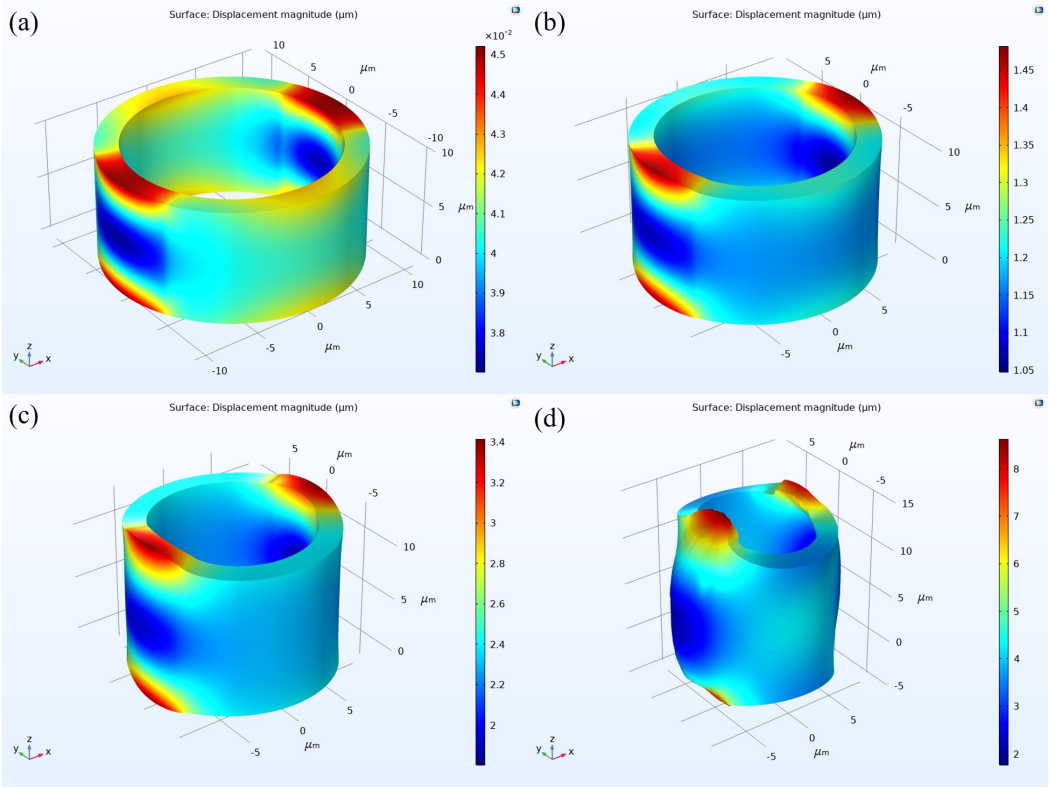

Figure 3.4 – Deformation image: active stress (a) $\zeta = 0.1$, (b) $\zeta = 0.31$, (c) $\zeta = 0.61$, (d) $\zeta = 0.91$.

The relationship between the applied active stress and elongation was extracted from the software and compared with the results obtained in the theoretical study, as shown in Fig.3.5, and they have a good agreement.

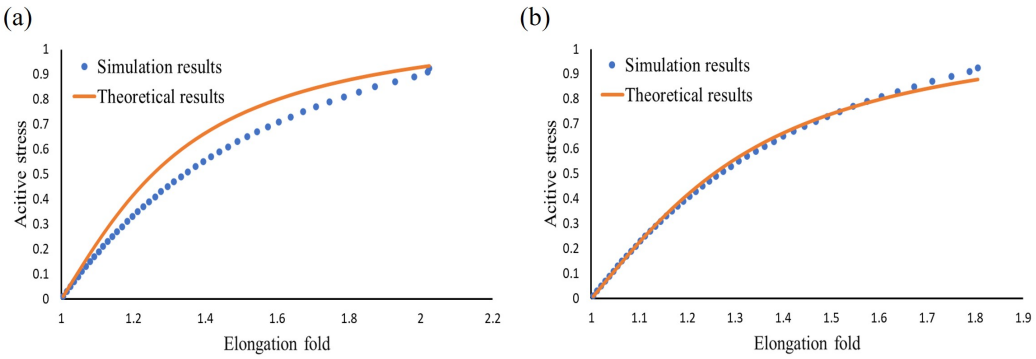

Figure 3.5 – The relationship between elongation fold and active stress. (a) Simulation data is taken from maximum elongation, (b) Simulation data is taken from medium elongation.

3.3 Theoretical model for early elongation

Experimental measurements of the early elongation stages enable the evaluation of the embryo's diameter, as well as its active or passive stress in relation to elongation fold [4, 138]. While this initial stage has been extensively examined in previous studies, we chose to revisit it in the context of our geometry, aiming to provide a simpler model for studying the late elongation of C. elegans embryo. During the late elongation phase, it becomes necessary to consider the influence of muscles. The addition of muscles not only increases the complexity of the internal geometry but also imposes complex dynamic deformations on the model. As a result, the differences between seam cell parts and D/V parts are disregarded in our model.

At the end of early elongation, the embryo undergoes a pre-strain, which we describe in our model as $\mathbf{G}_0$. Geometry and mechanical information are shown in Figure 3.6(a). Here, we need to first accurately determine $\mathbf{G}_0$ with the help of the experimental data [4, 138]. The finite deformation gradient:

$$\mathbf{F}_0 = \begin{pmatrix} r'(R) & 0 & 0 \\ 0 & r(R)/R & 0 \\ 0 & 0 & \lambda \end{pmatrix}, \tag{3.1}$$

where $r(R)$ is the radius after early elongation. $\mathbf{G}_0$ represents the circumferential strain exerted by actin during the early elongation and is a slowly varying function of time,

$$\mathbf{G}_0 = \begin{pmatrix} 1 & 0 & 0 \\ 0 & g_0 & 0 \\ 0 & 0 & 1 \end{pmatrix}, \tag{3.2}$$

where $0 < g_0 < 1$ in the actin layer, and $g_0 = 1$ in the part without actin budles. The real structure as shown in Fig.3.6(a), is divided into three distinct sections: the outer layer is the actin cortex, the thin ring where actin bundles concentrate and work, located within a radius range between ${R_2}'$ and R_3, the middle layer ($R_2 < R < {R_2}'$), which is the epidermis but without actin; and the inner part ($0 < R < R_2$), where the muscle is located, along with some internal organs, tissues, and fluids. As the muscle is not active during the early elongation phase and exists only as a structure, to simplify the calculation, we converted the four muscle parts into thin layers attached to the epidermis in equal proportions to ensure the continuity of the model, and divide our model into four parts, see Fig.3.6(b). The actin layer (${R_2}' < R < R_3$), epidermis layer ($R_2 < R < {R_2}'$) and muscle layer (${R_1}' < R < R_2$) are considered as incompressible materials, and the inner part ($0 < R < {R_1}'$) is compressible. The parameters required for the calculation are shown in the table 3.1.

Table 3.1 – Parameters adopted in this work

Geometry parameters	Normalized radius[1]	R_1=0.7	R_2=0.8	R_2'=0.96	R_3=1
	The location of muscles[2]	$\theta_1 = \frac{2}{3}\pi$ $\theta_2 = \frac{5}{6}\pi$	$\theta_3 = \frac{7}{6}\pi$ $\theta_4 = \frac{4}{3}\pi$	$\theta_5 = \frac{5}{3}\pi$ $\theta_6 = \frac{11}{6}\pi$	$\theta_7 = \frac{1}{6}\pi$ $\theta_8 = \frac{1}{3}\pi$
Material parameters (Shear modulus)[3]	Actin part	$\mu_a = 5$			
	Epidermis part	$\mu_e = 1$			
	Muscles	$\mu_m = 100$			
	Soft inner part	$\mu_i = 1/200$			

[1] The radius are extracted or deduced by the Ref.[4, 166].

[2] The location and size of muscles are deduced by the Ref.[166, 167].

[3] The units of the shear modulus are the KPa and is scaled by the epidermis one. It gives for the muscle, a value consistent with the muscle shear modulus proposed in [168].

The Neo-Hookean energy function is used for the incompressible parts:

$$W = \mu \left[\frac{1}{2} \left(Tr \left(\mathbf{F_e} \mathbf{F_e}^T \right) - 3 \right) - p \left(\det \mathbf{F_e} - 1 \right) \right], \tag{3.3}$$

According to the Euler-Lagrange equations, we can obtain the radius of the actin layer (r_a), epidermis layer (r_e) and muscle layer (r_m):

$$r_a = \sqrt{\frac{g_0 R^2 + A}{\lambda}}, \quad r_e = \sqrt{\frac{R^2 + E}{\lambda}}, \quad r_m = \sqrt{\frac{R^2 + M}{\lambda}}. \tag{3.4}$$

where A, E and M are constant, and the Lagrange multiplier p in the actin, epidermis and muscle layer reads:

$$p_a = \frac{-\log(R) + \frac{1}{2} {g_0}^2 \left(-\frac{A}{A + g_0 R^2} + \log\left(A + g_0 R^2\right) \right)}{g_0 \lambda} + C_a, \tag{3.5}$$

$$p_e = -\frac{\frac{E}{E+R^2} + 2\log(R) - \log\left(E + R^2\right)}{2\lambda} + C_e, \tag{3.6}$$

$$p_m = -\frac{\frac{M}{M+R^2} + 2\log(R) - \log\left(M + R^2\right)}{2\lambda} + C_m. \tag{3.7}$$

For the compressible part, we take the energy function form [169]:

$$W = \frac{\mu}{2} \left(Tr \left(\mathbf{F_e} \mathbf{F_e}^T \right) - 3 + \kappa (\det \mathbf{F_e} - 1)^2 \right) \tag{3.8}$$

where κ is a material constant. The radius of the inner part:

$$r_i = \frac{aR}{\sqrt{\lambda}} \tag{3.9}$$

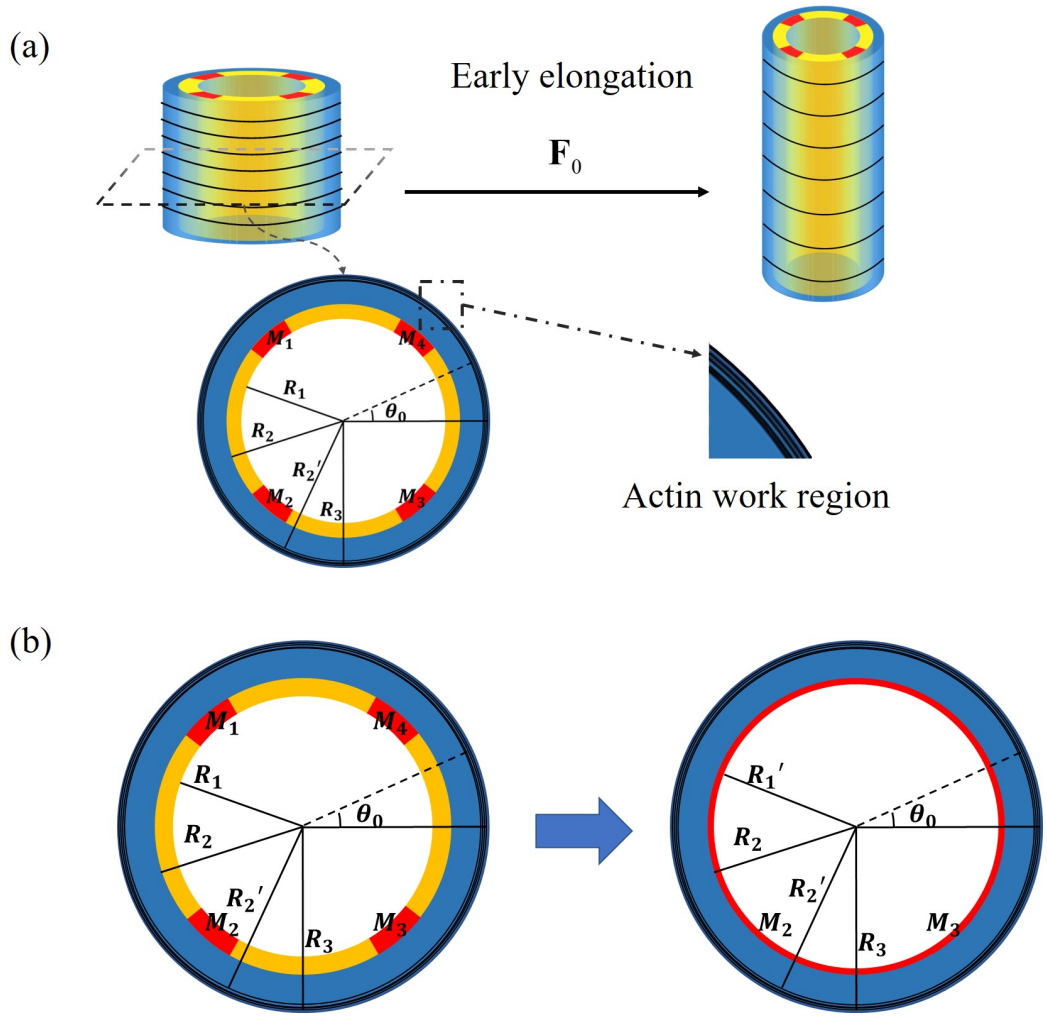

Figure 3.6 – (a) The schematic of early elongation and the cross-section of *C. elegans*. In the cross-section, the black circled part is the actin region ($R_2{}' < R < R_3$, with shear modulus μ_a), and the blue part is the epidermis layer ($R_2 < R < R_2{}'$, shear modulus μ_e). The central or inner part ($0 < R < R_2$) has a shear modulus μ_i, except the muscles which are stiffer. (b) Cross-sectional simplified model with four scattered muscle sections simplified to thin layers ($R_1{}' = 0.768$).

where a is a constant.

By considering the boundary condition $\sigma_{rr} = 0$ on the outer border $R = 1$:

$$\sigma_{arr}(R=1) = \mu_a \left[\left(\frac{\partial r_a(1)}{\partial R} \right)^2 - p_a(1) \right] = 0 \tag{3.10}$$

the continuity of the radius:

$$r_a(\mathrm{R}_2{}') = r_e(\mathrm{R}_2{}'), \quad r_e(\mathrm{R}_2) = r_m(\mathrm{R}_2), \quad r_m(\mathrm{R}_1{}') = r_i(\mathrm{R}_1{}'), \tag{3.11}$$

and the continuity of the radial stresses σ_{rr} in $R_2{}'$ and R_2 :

$$\mu_a \left[\left(\frac{\partial r_a(\mathrm{R}_2{}')}{\partial R} \right)^2 - p_a(\mathrm{R}_2{}') \right] = \mu_e \left[\left(\frac{\partial r_e(\mathrm{R}_2{}')}{\partial R} \right)^2 - p_e(\mathrm{R}_2{}') \right], \tag{3.12}$$

$$\mu_e \left[\left(\frac{\partial r_e \left(\mathrm{R}_2 \right)}{\partial R} \right)^2 - p_e \left(\mathrm{R}_2 \right) \right] = \mu_m \left[\left(\frac{\partial r_m \left(\mathrm{R}_2 \right)}{\partial R} \right)^2 - p_m \left(\mathrm{R}_2 \right) \right]. \tag{3.13}$$

We can obtain expressions for constants E, M, C_a, C_e and C_m from the above equations.

We substitute all size, material parameters and $\kappa = 100$, $\lambda = 1.8$ into the last condition $\sigma_{mrr}\left(\mathrm{R_1}'\right) = \sigma_{irr}\left(\mathrm{R_1}'\right)$:

$$\mu_m \left[\left(\frac{\partial r_m \left(\mathrm{R_1}' \right)}{\partial R} \right)^2 - p_m \left(\mathrm{R_1}' \right) \right] = \mu_i \sigma_{irr} \left(\mathrm{R_1}' \right), \tag{3.14}$$

where σ_{irr}:

$$\sigma_{irr} = \frac{2}{\det \mathbf{F_e}} \left((\det \mathbf{F_e})^2 \frac{\partial W}{\partial (\det \mathbf{F_e})^2} + \frac{\partial W}{\partial \left(tr(\mathbf{F_e} \mathbf{F_e}^T) \right)} r_i'(R)^2 \right). \tag{3.15}$$

and we obtain the relationship between the constant A and g_0.

Finally, by prescribing a zero traction in average condition on the top of the cylinder, noticeably, the muscle part was considered inextensible, so no stress on the top:

$$\int_{R_2'}^{1} \sigma_{azz} r_a r_a' dR + \int_{R_2}^{R_2'} \sigma_{ezz} r_e r_e' dR + \int_{0}^{R_1'} \sigma_{izz} r_i r_i' dR, \tag{3.16}$$

where:

$$\sigma_{azz} = \lambda^2 - p_a, \quad \sigma_{ezz} = \lambda^2 - p_e, \tag{3.17}$$

$$\sigma_{izz} = \frac{2}{\det \mathbf{F_e}} \left((\det \mathbf{F_e})^2 \frac{\partial W}{\partial (\det \mathbf{F_e})^2} + \frac{\partial W}{\partial \left(tr(\mathbf{F_e} \mathbf{F_e}^T) \right)} \lambda^2 \right), \tag{3.18}$$

all solutions $g_0 = 0.88$, $A = 0.08$ and $r_a(1) = 0.73$ can be determined. We can then obtain the radius and elongation fold of the model at different g_0 in the same way, as illustrated in Fig.3.7, the results of our model and the experimental data are in good agreement [4, 138]. This demonstrates the consistency of the geometric and elastic modeling together with the choice of a pre-strain represented by $\mathbf{G}_0$ which gives a good prediction of the early elongation.

3.4 Estimation of myosin activity

From the first stage elongation represented by the brown dots and the brown dashed line in Fig.3.7 we can extract the time evolution of the contractile pre-strain $g_0(t_i)$ derived from our elastic model. To explain quantitatively $g_0(t)$, we suggest a phenomenological dynamical approach for the population

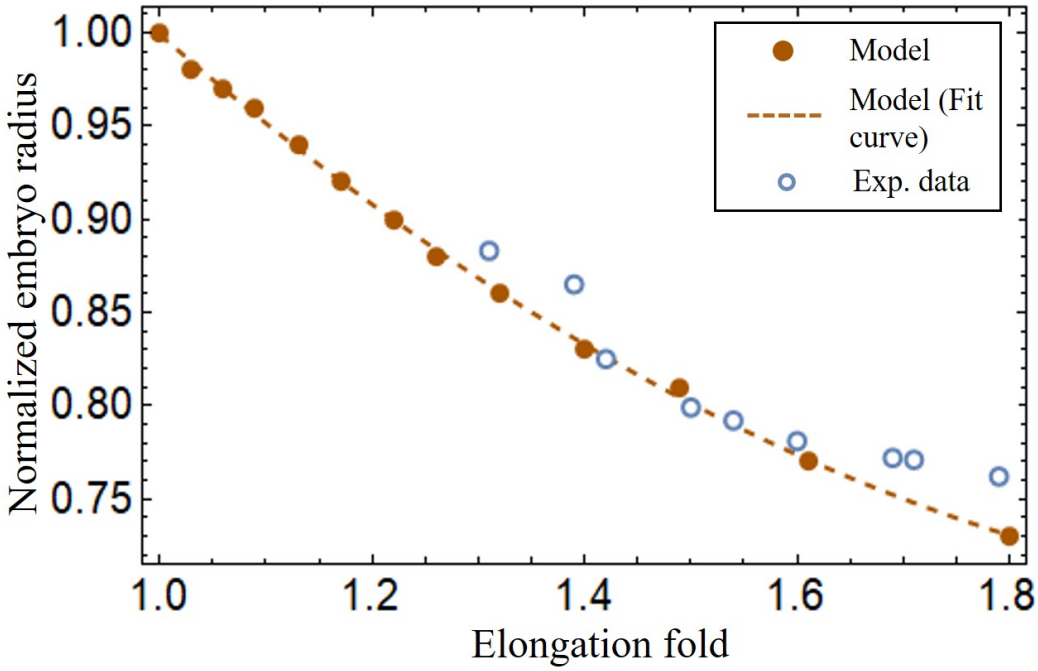

Figure 3.7 – Predictions of normalized embryo radius evolution during early elongation by the pre-strain model compared with experimental data from [138]. For the model, please refer the Eq.(3.4).

of active myosin motors. This equation takes into account the competition between the recruitment of new myosin proteins from the epidermis cytoskeleton necessary to extend more the embryo and the debonding of these myosins from the actin cables, which is damped by the compressive radial stress. It reads:

$$\frac{dX_g(t)}{dt} = \left(p_1 - p_2 X_g(t) e^{-p_3 X_g(t)}\right) \frac{t_v}{t_p} \tag{3.19}$$

with $X_g = 1 - g_0(t)$, p_1 is the ratio between the free available myosin population and the attached ones divided by the time of recruitment (given in minutes), while p_2 is the inverse of the debonding time of the myosin motors from the cable: $p_2 = 6$ min^{-1}. The time required for non-muscle myosin detachment is estimated to be $\tau_0 = 10s$ for free acto-myosin filaments. If the actin filament is submitted to external loading perpendicular to its axis, the detachment can be helped or on the contrary inhibited, see [170], page 169-170. In the present case, the stresses acting in the radial direction of an actin bundle are compressive and thus will delay the detachment. This energy has to be compared to the energy of detachment of all myosin motors from the bundle. The corresponding elastic energy associated with the radial deformation for an actin cable of length l_a of radius $r_b = 0.05\mu m$ (estimated from [166]) and shear modulus $\mu_a = 5\ KPa$ is given by $1/2\mu_a(1 - g_0(t))\pi l_a r_b^2 = 210^{-11} l_a\ J$. This result must be compared to the individual energy of detachment times the number of myosin motors on a cable. This number is uneasy to fix but estimation is given by the length of the cable l_a divided by the distance between 2 anchoring sites of myosin which is about $5nm$ while the attachment energy per motor is about $6k_bT$. These indications are for skeletal muscle myosins [170] and have to be taken with caution. Nevertheless, the order of magnitude of the debonding energy for a collection of myosin heads from actin cable can be estimated to be order of $4.8 l_a 10^{-12} J$. Then the ratio between both quantities is of order $4(1 - g_0(t))$ which explains that the time-scale of debonding for a cable in compressive stress in

the orthogonal direction of its axis is then:

$$\tau_{deb} = \tau_0 e^{p_3(1-g_0(t))} \tag{3.20}$$

where p_3 is a positive constant of order one which cannot be predicted exactly. This time scale justifies the exponential correction in Eq.(3.19).

The debonding time increases (or decreases) when the actin cable is in radial compressive (or tensile) stress, see Eq.(3.20). τ_v is the visco-elastic time estimated from laser ablation fracture operated in the epidermis [171]: $t_v = 6s$ and τ_p is the time required for the activation of the myosin motors $t_p = 1200s$ [170]. This equation is similar to the model derived by Serra *et al.* [172] for the viscous stress occurring in gastrulation.

Notice that only p_1 and p_3 must be obtained by comparison of $g_0(t)$ deduced from Eq.(3.19) with the values deduced from our elastic model. The result of Eq.(3.19) with $p_1 = 0.6$ and $p_3 = 0.75$ are shown in Fig.3.8 with a rather good agreement.

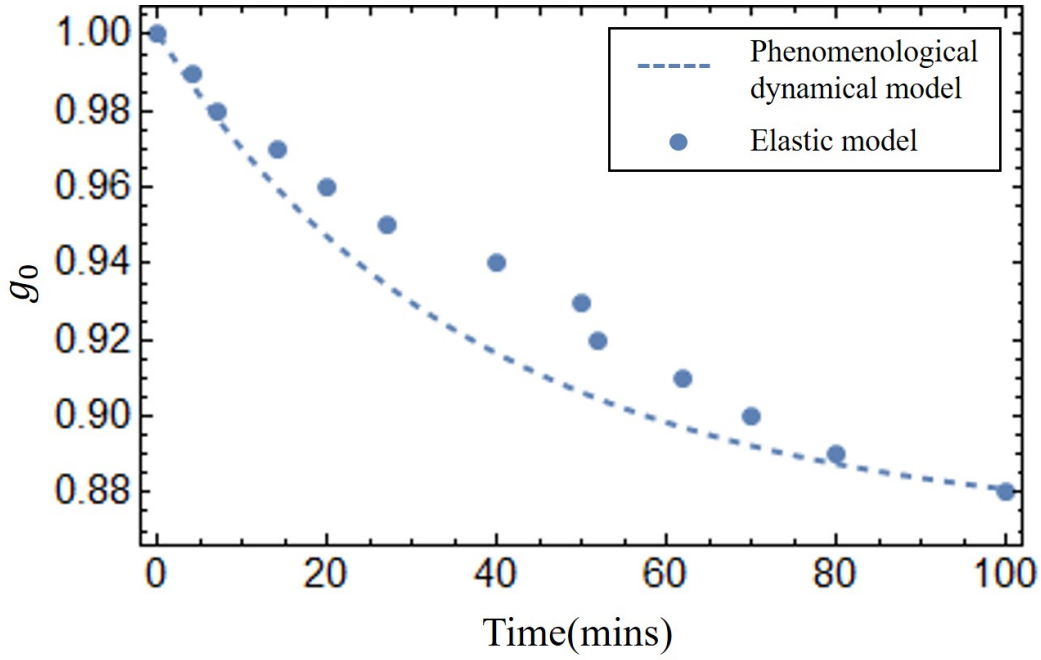

Figure 3.8 – Comparison of elastic and dynamical model results. Blue dots: extraction of the parameter $g_0(t)$ from Eq.(3.14) and Eq.(3.16). Blue dash line, refer to the Eq.(3.19).

3.5 Conclusion and discussion

The elongation process in the early stages of the nematode is caused by circumferential contractions caused by the acto-myosin network. We have previously studied early elongation in *C. elegans* embryos characterized by an inner cylinder [4] surrounded by epithelial cells located in a cortical position. The cortex consists of three distinct cell types - seam cells, dorsal cells and ventral cells - which exhibit a unique cytoskeletal organization and actin network configuration. Of these, only the seam cells possess an active myosin motor that functions in the positive radial direction to contract the circumferential body,

thereby triggering the early elongation process. We have recovered this process by means of COMSOL software and obtained good agreement with the theoretical results.

During the late elongation phase, it is crucial to consider the influence of muscles. To mitigate the effects of increasingly complex structures, we propose a novel elastic theoretical model for calculating pre-strain induced by acto-myosin contraction. In this model, we no longer differentiate between the three distinct cells of the epidermis; instead, we treat them as homogeneous matter, and the effect of inactive muscle structure is also taken into account. The final results also agree well with the experimental data. The study of this model is the basis for our study of *C.elegans* late elongation, which will be discussed in the next chapter. In addition, we present a model for the recruitment of active myosin motors under force, which estimates the activity of the early actomyosin network through a kinetic model of the phenomenon. The proposed model can be extended to biological tissues and organs where myosin controls growth and development.

Chapter 4

Muscle contractions and late elongation

The chapter focuses on muscle activity leading to late elongation. It begins with a brief background discussion in section 4.1, followed by a detailed description of the theoretical model and its deformation under active dynamics in section 4.2. Sections 4.3 and 4.4 explain the principles of energy conversion leading to elongation and the generation of frictional dissipation. Finally, section 4.5 presents the conclusion and discussion.

4.1 Introduction

Muscle is found in most animals, including the simple invertebrate *C. elegans*. Muscle fibers consist of myofibrils, which contain mainly actin filaments and myosin. Muscle fibers produce contraction, which may change their own length or shape, or maintain their shape to resist extrinsic tension. Typically, its active deformation is dominated by contraction. They play a very crucial role in the development of the *C. elegans* embryo. When it elongates to the 1.8-fold stage, the muscles under the dorsal and ventral epidermis begin to contract and relax, which leads to an active embryo. Although the contractility of acto-myosin is still present, it is believed to play a secondary role in elongation, whereas the role of muscle activity is essential to embryonic late elongation. BD Williams and RH Waterston demonstrated that mutants with muscle defects (Pat mutant [163]) are unable to complete the elongation process even though the acto-myosin network is functioning properly [166]. Fig.3.1(b) shows the schematic image of *C. elegans* body [173] with four rows of muscles, two of which are underneath the dorsal epidermis and the other two are under the ventral epidermis.

As observed *in vivo*, *C. elegans* exhibits systematic rotations accompanying each contraction [174], and deformations such as bending and twisting. Eventually, the *C. elegans* embryo will complete an elongation from 1.8-fold to 4-fold. We can imagine that once the muscle is activated on one side, it can only contract, and then the contraction forces will be transmitted to the epidermis on this side. So one can wonder how an elongation can occur since striated muscles can only perform cycles of contraction and relaxation, their action will tend to reduce the length of the embryo. Therefore, it is necessary to understand how the embryo elongates during each contraction and how the muscle contractions couple to the acto-myosin activity. This work aims to answer this paradox within the framework of finite elas-

ticity without invoking cell plasticity and stochasticity which cannot be considered as driving forces. In addition, several important issues at this stage remain unsettled. First of all, we may also observe a torsion of the embryo but if the muscle activity suggests a bending, it cannot explain alone a substantial torsion. Secondly, a small deviation of the muscle axis [167] is responsible for a series of rotations, how to relate these rotations to the muscle activation [174]. Since any measurement on a motile embryo at this scale is difficult, it is meaningful to explore the mechanism of late elongation theoretically. Furthermore, muscle contraction is crucial in both biological development and activities and has been studied extensively by researchers [175, 176], but how it works at small scales remains a challenge.

Using a finite elasticity model and assuming the embryonic body shape is cylindrical, we can evaluate the geometric bending deformation and the energy released during each muscular contraction on one side since after each contraction, the muscles have time to relax and then muscles on the opposite side undergo a new contraction. This cyclic process leads to a tiny elongation of the cylinder along its symmetry axis at each contraction. Each of them is correlated with the rotational movements of the embryo [174]. By repeating these pairs of contractions more than two hundred times, a cumulative extension is achieved. In the case of muscle activation, the worm becomes deformed and is unable to avoid friction with the egg shell, which also can be evaluated by the model. Furthermore, the mechanical model explains the existence of a torque operating at the position of the head or tail by the coupling of muscle contraction with the ortho-radial acto-myosin forces. Finally, the small deviation between the muscles and the central axis experimentally detected [167] induces cyclic rotations and possibly torsion leading to fluid viscous flow inside the egg. Quantifying all these processes allows evaluating the physical quantities of the embryo such as the shear modulus of each component, the osmolarity of the interstitial fluid and the active forces exerted by the acto-myosin network and the muscles which are sparsely known in the embryonic stages.

4.2 Theoretical model for late elongation

For the above-mentioned unresolved problems, we propose a simple mechanical model, which accounts for the dynamical deformations of a layered soft cylinder, and enables us to make accurate quantitative predictions about the activities of the actomyosin and muscle networks of the embryo.

4.2.1 Filamentary model

The early elongation of *C. elegans* embryo was previously discussed in the last Chapter 3. We continue to use the cylindrical model and treat the epidermis in the same way with effective activity localized along the circumference, supported by four muscles distributed beneath the epidermis. Muscles play no role in the early elongation stage so were not considered previously [4, 138]. After this period of approximately 80% increase in length, muscles parallel to the main axis and actin bundles organized along the circumference will collaborate to facilitate further elongation. Table 4.1 provides the size parameters of *C. elegans* which will be introduced hereafter.

Table 4.1 – Adopted real size parameters of the *C. elegans* [4, 138]

	Initial	1.8-fold
Radius	$11.1\mu m$	$8.2\mu m$
Length	$50\mu m$	$90\mu m$

We focus on the overall deformation of a full cylinder or a thin rod, having a length L greater than the radius R and a central vertical axis along the Z direction. Contrary to previous works [4, 177], here we decide to simplify the geometrical aspect because of the mechanical complexity. The biological activity induced by the acto-myosin network and muscles is represented by active strains, and the global shape is the result of the coupling between elastic and active strains, modulated by dissipation. Active strains are generated through non-mechanical processes (e.g., biochemical processes): myosin motors and striated muscles receive their energy from ATP hydrolysis, which is converted to mechanical contractions of fibers.

This framework of the theoretical model has been presented in a series of articles by A. Goriely and collaborators [178, 179, 180, 181, 182]. As one imagines, it is far from triviality and most of the literature on this subject concerns either full cylinders or cylindrical shells in torsion around the axis of symmetry, the case of bending is more overlooked. However, the geometry of the muscles in *C. elegans* leads automatically to a bending process that cannot be discarded. We take advantage of these previous works and apply the methodology to our model.

Deformation gradient

We consider the muscles and the actin bundles of the *C. elegans* embryo as filamentary structures. When they are activated, these fibers will generate internal stresses that will create bending and torsion of the entire structure. We define the initial configuration $\mathcal{B}_0$ with material points (X, Y, Z), and the mapping function $\chi(\mathbf{X})$ which links the initial configuration $\mathcal{B}_0$ to the current configuration $\mathcal{B}$. Herein, we concentrate on the overall deformation, so the model can be simplified to a single filament in space with its centerline being $\mathbf{r}(\mathbf{Z})$, as shown in Fig.4.1(a), from which, a local director basis can be defined: $(\mathbf{d}_1(Z), \mathbf{d}_2(Z), \mathbf{d}_3(Z))$. The axial extension ζ is obtained by $\mathbf{r}'(Z) = \zeta \mathbf{d}_3$, where $'$ denotes the derivative with respect to the material coordinate Z. From the director basis, the Darboux curvature vector reads:

$$\mathbf{u} = u_1 \mathbf{d}_1 + u_2 \mathbf{d}_2 + u_3 \mathbf{d}_3. \tag{4.1}$$

So, this vector gives the evolution of the director basis along the filamentary line as:

$$\mathbf{d}_i{}'(Z) = \zeta \mathbf{u} \times \mathbf{d}_i, \tag{4.2}$$

The geometric mapping χ is then:

$$\chi(\mathbf{X}) = \mathbf{r}(Z) + \sum_{i=1}^{3} \varepsilon a_i(\varepsilon R, \Theta, Z)\, \mathbf{d}_i(Z), \tag{4.3}$$

where the a_i represents the deformation in each direction of the section with $a_i\,(0,0,Z) = 0$ so that the Z-axis maps to the centerline $\mathbf{r}\,(Z)$. The small quantity ε is the ratio between the radius R and the length L of the cylinder.

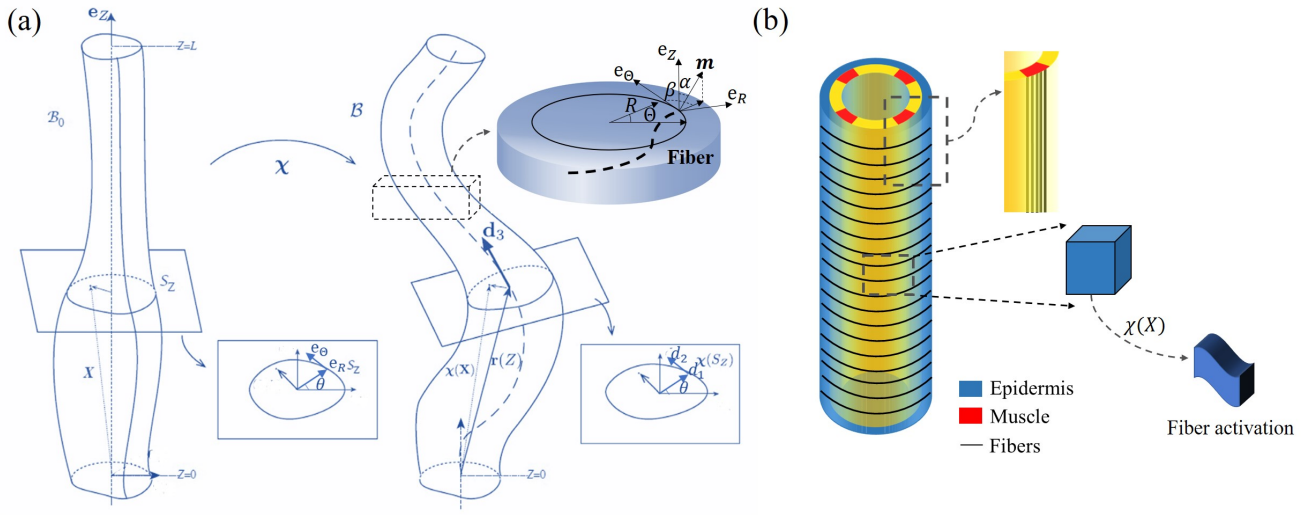

Figure 4.1 – (a) Cylindrical structure in the reference configuration (left) with a vertical central axis and its deformation in the current configuration (right). The deformed configuration is fully parameterized by the centerline $\mathbf{r}\,(Z)$ (resulting from the distortion of the central axis) and the deformation of each cross-section [181]. (b) Schematic representation of the body shape of the *C. elegans* embryo with the cortical epidermis and the four muscles. The fibers are embedded in the cortex. The blue part representing the epidermis shows the outer distribution of the actin organized into horizontal hoop bundles when the muscles are not activated. The yellow part includes the vertical red muscles, represented by axial fibers.

The geometric deformation gradient is [183]

$$\mathbf{F} = Grad\chi = \mathbf{F_e}\mathbf{G} \tag{4.4}$$

where $\mathbf{G}$ represents the active strain generated by the fibers: the actomyosin or the muscles, and $\mathbf{F_e}$ is the elastic strain tensor. Notice that this relationship also applies to growing materials and G in this case means the local amount of growth. However, in this period of elongation and more generally in the whole egg lifespan there is no nutrient and there is no growth.

Activation is naturally expressed as a map from the cylindrical coordinates $(\varepsilon R, \Theta, Z)$ of the reference configuration to the cylindrical coordinates (r, θ, z):

$$\mathbf{G} = (\mathbf{1} + \varepsilon\mathbf{G}_1\,(\mathbf{X}))\,\mathbf{G}_0 = G_{ij}\mathbf{e}_i \otimes \mathbf{e}_j, \qquad i \in \{r,\theta,z\}\,, \quad j \in \{R,\Theta,Z\} \tag{4.5}$$

where $(\mathbf{e}_r, \mathbf{e}_\theta, \mathbf{e}_z)$ and $(\mathbf{e}_R, \mathbf{e}_\Theta, \mathbf{e}_Z)$ are the unit vectors in the current and reference configuration respectively. If we only focus on the late elongation, the pre-strain is not taken into account, $\mathbf{G}_0 = \mathbf{I}$. But, if we consider the whole elongation process, the elongation induced by myosin during early elongation can not be ignored, where $\mathbf{G}_0$ refers to the pre-strain of the early elongation period and $\mathbf{G}_1$ is the muscle-actomyosin supplementary active strain in the late period. Actin is distributed in a circular pattern in the outer epidermis, see Fig.4.1(b), so the finite strain $\mathbf{G}_0$ is defined as $\mathbf{G}_0 = Diag\,(1, g_0(t), 1)$, where $0 < g_0 < 1$ is the time-dependent decreasing eigenvalue, operating in the actin zone, and is equal to

unity $g_0 = 1$ in the other parts. We will discuss two cases without pre-strain and pre-strain after.

Taking $\zeta = 1 + \varepsilon\xi$, the deformation gradient follows the description of Eq.(4.3) :$\mathbf{F} = F_{ij}\mathbf{d}_i \otimes \mathbf{e}_j$, where $i \in \{1, 2, 3\}$, and j labels the reference coordinates $\{R, \Theta, Z\}$ finally reads:

$$\mathbf{F} = \begin{bmatrix} a_{1R} & \frac{1}{R}a_{1\Theta} & \varepsilon\left(1+\varepsilon\xi\right)\left(u_2 a_3 - u_3 a_1 \sin a_2\right) \\ a_1 a_{2R} & \frac{a_1}{R}a_{2\Theta} & \varepsilon\left(1+\varepsilon\xi\right)\left(u_3 a_1 \cos a_2 - u_1 a_3\right) \\ a_{3R} & \frac{1}{R}a_{3\Theta} & \left(1+\varepsilon\xi\right)\left(1+\varepsilon\left(u_1 a_1 \sin a_2 - u_2 a_1 \cos a_2\right)\right) \end{bmatrix}. \tag{4.6}$$

When considering a filamentary structure with different fiber directions $\mathbf{m}$, these directions are specified by two angles α and β, as outlined in [169]:

$$\mathbf{m} = \sin\alpha \sin\beta \mathbf{e_R} + \sin\alpha \cos\beta \mathbf{e_\Theta} + \cos\alpha \mathbf{e_Z}, \quad \alpha, \beta \in [-\pi/2, \pi/2]. \tag{4.7}$$

where α and β lie in the range $[-\pi/2, \pi/2]$. For muscle fibers, $\alpha_m = 0$ and $\beta_m = 0$, whereas for hoop fibers of the actin network, $\alpha_a = \pi/2$ and $\beta_a = 0$. When all fiber orientations are included, the incremental strain $\mathbf{G}_1$ in cylindrical coordinates is related to the amplitude of the active strain g and the orientation angles: α, and β. Considering all the different orientations of fiber cases, the active filamentary tensor in cylindrical coordinates is:

$$\mathbf{G}_1 = g_i \begin{bmatrix} \sin^2\alpha\sin^2\beta & \sin^2\alpha \sin\beta\cos\beta & \sin\alpha\cos\alpha\sin\beta \\ \sin^2\alpha \sin\beta\cos\beta & \sin^2\alpha\cos^2\beta & \sin\alpha\cos\alpha\cos\beta \\ \sin\alpha\cos\alpha\sin\beta & \sin\alpha\cos\alpha\cos\beta & \cos^2\alpha \end{bmatrix} \tag{4.8}$$

where g_i represents the activity (g_m for the muscles and g_a for acto-myosin), and since both are contractile, their incremental activities are negative.

The energy density

To relate the deformations to the active forces induced by muscles and the acto-myosin network, we assume that the cylindrical body is a hyperelastic material with strain-energy density $W = W(\mathbf{F_e})$. The material is assumed incompressible. The total energy of the system is

$$\mathcal{W} = \int_{B_0} W(\mathbf{F_e})\, \mathrm{d}X\mathrm{d}Y\mathrm{d}Z, \tag{4.9}$$

where $\mathbf{F_e} = \mathbf{F}\mathbf{G}^{-1}$, which can be written as:

$$\mathcal{W} = \int_{B_0} V(\mathbf{F}\mathbf{G}^{-1}, \mathbf{G})\, \mathrm{d}X\mathrm{d}Y\mathrm{d}Z, \qquad V = W\left(\mathbf{F}\mathbf{G}^{-1}\right) - p(J-1). \tag{4.10}$$

where $J = \det \mathbf{F}_e$, p is a Lagrange multiplier which ensures the incompressibility of the sample, a physical property assumed in living matter. And we use the Neo-Hookean energy function:

$$W(\mathbf{F}_e) = \frac{\mu}{2}\left(tr\left(\mathbf{F}_e {\mathbf{F}_e}^T\right) - 3\right), \tag{4.11}$$

The problem now is to minimize the energy over each section for a given active force. In cylindrical coordinates, the energy functional can be written

$$\mathcal{W} = \varepsilon^2 \int_0^L \mathrm{d}Z \int_S V(\mathbf{F}\mathbf{G}^{-1}, \mathbf{G}) R \, \mathrm{d}R \, \mathrm{d}\Theta \tag{4.12}$$

The auxiliary strain-energy density can be obtained by expanding the inner variables a_i, p_i and the potential V as:

$$\mathbf{a} = \mathbf{a}^{(0)} + \varepsilon \mathbf{a}^{(1)} + \varepsilon^2 \mathbf{a}^{(2)} + \mathcal{O}\left(\varepsilon^3\right), \tag{4.13}$$

$$p = p^{(0)} + \varepsilon p^{(1)} + \varepsilon^2 p^{(2)} + O\left(\varepsilon^3\right), \tag{4.14}$$

$$V(\mathbf{F}_e, \mathbf{G}) = V_0 + \varepsilon V_1 + \varepsilon^2 V_2 + O\left(\varepsilon^3\right). \tag{4.15}$$

For each cross-section, the associated Euler-Lagrange equations take the following form:

$$\frac{\partial}{\partial R}\frac{\partial V_i R}{\partial a_{jR}^{(k)}} + \frac{1}{R}\frac{\partial V_i R}{\partial a_{jR}^{(k)}} + \frac{\partial}{\partial \Theta}\frac{\partial V_i R}{\partial a_{j\Theta}^{(k)}} - \frac{\partial V_i R}{\partial a_j^{(k)}} = 0, j = 1, 2, 3, k = 0, 1, \tag{4.16}$$

in association with boundary conditions at each order $k = 0, 1$ on the outer radius R_i:

$$\left.\frac{\partial V_i R}{\partial a_{jR}^{(k)}}\right|_{R=R_i} = 0, j = 1, 2, 3. \tag{4.17}$$

Deformation of the model initially free of stress

Firstly, we ignored the influence induced by early elongation, and take $\mathbf{G}_0 = \mathbf{I}$. We solve these equations order by order and consider incompressibility. To lowest order, the solution of the Euler–Lagrange equations is obviously given by $\mathbf{a}^{(0)} = (R, \Theta, 0)$, and $p^{(0)} = 1$ so there is no deformation. It is easy to know the zero and first order energy vanish. At order $\mathcal{O}\left(\varepsilon^2\right)$ of the elastic energy, the solution for the active strain components are:

$$a_1^{(1)} = -\frac{R}{2}\xi - \frac{R^2}{8}\left(u_1 \sin\Theta - u_2 \cos\Theta\right) + f_1\left(R\right), \tag{4.18}$$

$$a_2^{(1)} = \frac{5R}{8}\left(u_1 \cos\Theta + u_2 \sin\Theta\right) + f_2\left(R\right), \tag{4.19}$$

$$a_3^{(1)} = \xi, \tag{4.20}$$

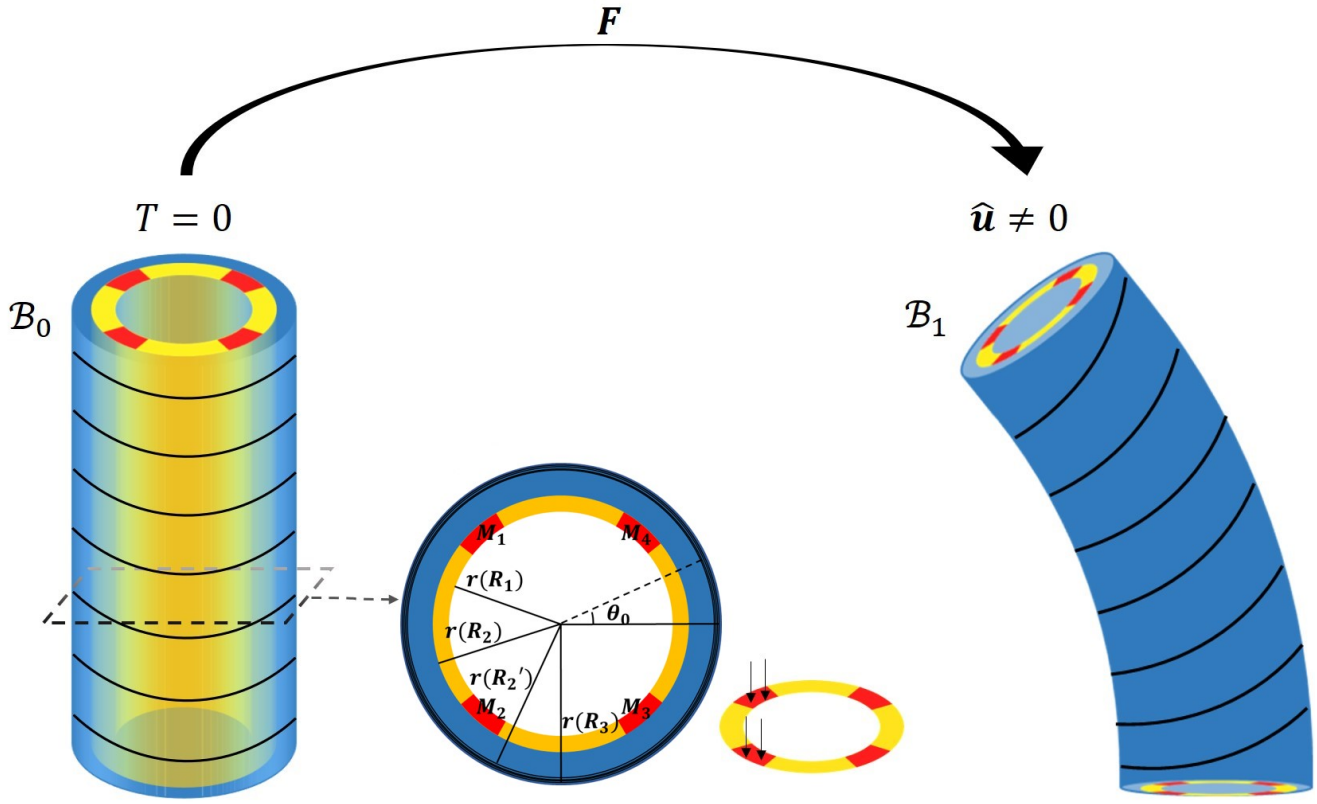

Figure 4.2 – The *C. elegans* model undergoes muscle contraction (incremental strain) in the absence of initial stress to generate curvature. $r(R)$ is the radius after early elongation, all values can be obtained by Eq.(3.4).

$$p^{(1)} = f_3\left(R\right). \tag{4.21}$$

where $f_{1,2,3}$ are functions related to the active stress R.

With the solutions for the active strains $\mathbf{a}^{(0)}$ and $\mathbf{a}^{(1)}$, the energy takes the form:

$$\mathcal{E} = \varepsilon^4 \int_0^L \mathrm{d}Z \int_S V_2\left(\mathbf{a}^{(0)}, \mathbf{a}^{(1)}; \mathrm{u}_1, \mathrm{u}_2, \mathrm{u}_3, \xi\right) R\mathrm{d}R\,\mathrm{d}\Theta + \mathcal{O}\left(\varepsilon^5\right), \tag{4.22}$$

and after integration

$$\mathcal{E} = \frac{1}{2}\int_0^L K_0(\zeta - \hat{\zeta})^2 + K_1(\mathrm{u}_1 - \widehat{\mathrm{u}}_1)^2 + K_2(\mathrm{u}_1 - \widehat{\mathrm{u}}_2)^2 + K_3(\mathrm{u}_3 - \widehat{\mathrm{u}}_3)^2\,\mathrm{d}Z. \tag{4.23}$$

After calculations, the second order energy density takes the form:

$$V_2 R = A_1\xi + A_2\xi^2 + B_1 u_1 + B_2 {u_1}^2 + C_1 u_2 + C_2 {u_2}^2 + D_1 u_3 + D_2 {u_3}^2 + E_1, \tag{4.24}$$

where A_i, B_i, C_i, D_i and E_1 are function of R and Θ. Comparing with the energy of an extensible elastic rod [184, 185, 186, 187, 188], we recognize the classic extensional K_0, bending K_1, K_2 and torsional

stiffness K_3 coefficients:

$$K_0 = \int_{S_K} A_2 dRd\Theta,\ K_1 = \int_{S_K} B_2 dRd\Theta,\ K_2 = \int_{S_K} C_2 dRd\Theta,\ K_3 = \int_{S_K} D_2 dRd\Theta, \tag{4.25}$$

where A_2, B_2, C_2 and D_2 are related to the shear modulus μ, so for a uniform material with no variations of shear modulus, S_K represents the cross-section of the cylinder. But if not, we need to divide different regions to perform the integration.

We now focus on the intrinsic extension and curvatures of the cylindrical object induced by the active strains, this requires the competition of the active forces with the stiffness of the cylindrical bar following the relationships,

$$\widehat{\zeta} = 1 - H_0/K_0,\ \widehat{u}_1 = -H_1/K_1,\ \widehat{u}_2 = H_2/K_2,\ \widehat{u}_3 = -H_3/K_3, \tag{4.26}$$

where the expression of H_i:

$$\begin{aligned} H_0 &= \frac{1}{2}\int_{S_H} A_1 dRd\Theta,\ H_1 = \frac{1}{2}\int_{S_H} B_1 dRd\Theta, \\ H_2 &= \frac{1}{2}\int_{S_H} C_1 dRd\Theta,\ H_3 = \frac{1}{2}\int_{S_H} D_1 dRd\Theta. \end{aligned} \tag{4.27}$$

where A_1, B_1, C_1 and D_1 are related to the shear modulus μ, the fiber angles α and β, and the activation g. So, the integration region S_H is divided into the different parts of the embryo which all contribute to the deformation. All calculation detail in APPENDICES 4.A.

Finally, we can obtain the second energy form with Eq.(4.24). The stiffness and curvatures are found by integrating over the cross-section. The intrinsic extension and curvature are

$$\hat{\zeta} = 1 - \frac{H_0}{K_0}, \quad \hat{u}_1 = -\frac{H_1}{K_1}, \quad \hat{u}_2 = \frac{H_2}{K_2}, \quad \hat{u}_3 = -\frac{H_3}{K_3}. \tag{4.28}$$

where K_i and H_i are calculated by Eq.(4.25) and Eq.(4.27). All calculation detail in APPENDICES 4.B.

To calculate the intrinsic Frenet curvature and torsion, we use the following equation:

$$\widehat{\kappa} = \sqrt{\widehat{u}_1^2 + \widehat{u}_2^2} \quad \text{and} \quad \widehat{\tau} = \frac{\widehat{u}_3}{\widehat{\zeta}}. \tag{4.29}$$

For the case of activated left side muscles, we can calculate intrinsic extension and curvatures by Eq.(4.28):

$$\hat{u}_{1m} = 0,\ \hat{u}_{3m} = 0, \tag{4.30}$$

so the intrinsic Frenet curvature and torsion Eq.(4.29):

$$\hat{\kappa}_m = \hat{u}_{2m},\ \hat{\tau}_m = 0. \tag{4.31}$$

Then, for the activated actin case, we can calculate intrinsic extension and curvatures by Eq.(4.28):

$$\hat{u}_{1a} = 0, \ \hat{u}_{2a} = 0, \tag{4.32}$$

and the intrinsic Frenet curvature and torsion Eq.(4.29):

$$\hat{\kappa}_a = 0, \ \hat{\tau}_a = \frac{\hat{u}_{3a}}{\hat{\zeta}_a}. \tag{4.33}$$

From these results, it can be seen that the curvature of the deformation is controlled only by muscle activation, while torsion is controlled only by actin activation.

Late elongation model based on the pre-strained configuration

Our model can consider an initial without strain/stress state, the case is displayed above. But indeed, the late elongation model needs to account for the effect of pre-strain induced by acto-myosin contractions in the first period. We consider the complex case of combining incremental strain due to muscle contraction and finite strain due to acto-myosin contraction at 1.8-fold to assess the effects of coupling muscle and actomyosin networks. The finite strain $\mathbf{G}_0$ can map the initial stress-free state $\mathcal{B}_0$ to a state $\mathcal{B}_1$. After in the residually stressed $\mathcal{B}_1$, we impose an incremental strain field $\mathbf{G}_1$, which represents the internal muscle contraction and maps the body to $\mathcal{B}_2$. The whole process is shown in Fig.4.3. So, the deformation gradient can be expressed as: $\mathbf{F} = \mathbf{F}_e\mathbf{G}_1\mathbf{G}_0$ [189].

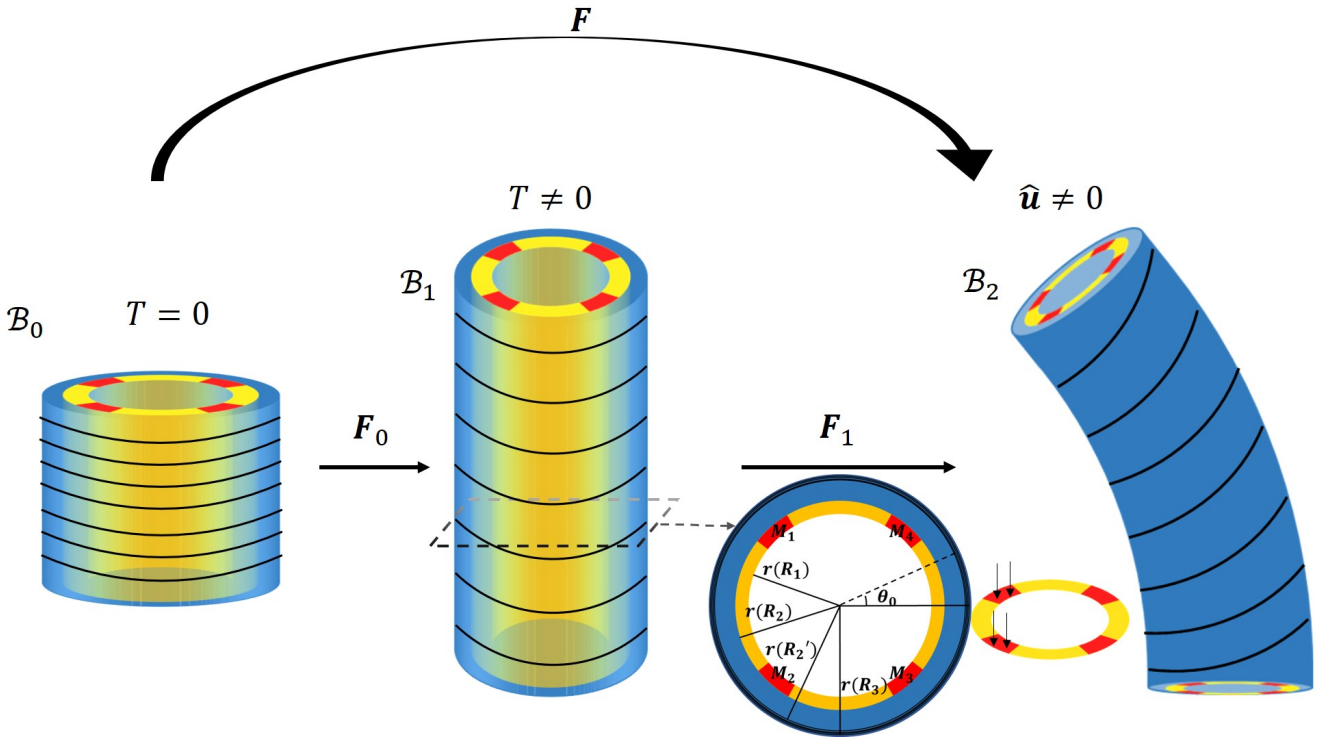

Figure 4.3 – The *C. elegans* model undergoes muscle contraction (incremental strain) in the absence of initial stress to generate curvature.

The deformation gradient becomes:

$$\mathbf{F}=\begin{bmatrix} a_{1R} & \frac{1}{R}a_{1\Theta} & \lambda\varepsilon\left(1+\varepsilon\xi\right)\left(u_2a_3-u_3a_1\sin a_2\right) \\ a_1a_{2R} & \frac{a_1}{R}a_{2\Theta} & \lambda\varepsilon\left(1+\varepsilon\xi\right)\left(u_3a_1\cos a_2-u_1a_3\right) \\ a_{3R} & \frac{1}{R}a_{3\Theta} & \lambda\left(1+\varepsilon\xi\right)\left(1+\varepsilon\left(u_1a_1\sin a_2-u_2a_1\cos a_2\right)\right) \end{bmatrix}, \tag{4.34}$$

where λ is the axial extension due to the pre-strain. $\mathbf{G}_1$ is given by Eq.(4.8), and we can know that $g_0 = 0.88$ when the muscle starts to contract which is the end of the early elongation, see Section 3.3.

To simplify the calculation, we write g_0 in the form of $1+\varepsilon c$ ($\varepsilon \approx 0.2$, $c \approx -0.6$). Here, we still use the Neo-Hookean energy function and expand the energy order by order as the Jacobian $J = \det(\mathbf{F_e})$. At the lowest order, the incompressibility imposes the deformation: $\mathbf{a}^{(0)} = \left(r\left(R\right), \Theta, 0\right)$ and the Euler-Lagrange equation gives the Lagrange parameter $P_0'(R)$ which finally read:

$$r'\left(R\right)=\frac{R}{\lambda r\left(R\right)}, \tag{4.35}$$

$$P_0{}'\left(R\right)=0, \tag{4.36}$$

and the boundary condition $\sigma_{rr}(R=1)=0$ gives the value of $P_0(R) = 1/\lambda$. At $\mathcal{O}\left(\varepsilon\right)$, the Euler-Lagrange equations are again automatically satisfied, and at $\mathcal{O}\left(\varepsilon^2\right)$, the crucial question is to get the correct expression for $a_i^{(1)}$ and $p^{(1)}$. Based on the previous subsection, the following form is intuited:

$$a_1^{(1)}=-\frac{1}{2}r\left(R\right)\xi+q_1r(R)^2\left(u_1\sin\Theta-u_2\cos\Theta\right)+h_1\left(R\right) \tag{4.37}$$

$$a_2^{(1)}=q_2r\left(R\right)\left(u_1\cos\Theta+u_2\sin\Theta\right)+h_2\left(R\right) \tag{4.38}$$

$$a_3^{(1)}=\lambda\xi \tag{4.39}$$

$$p^{(1)}=h_3\left(R\right) \tag{4.40}$$

As before, the Euler-Lagrange equations and incompressibility condition give the two constants:

$$q_1=\frac{1}{8}\left(-2+\lambda^3\right),\ q_2=\frac{1}{8}\left(2+3\lambda^3\right) \tag{4.41}$$

and h_1, h_2, h_3 are function of R.

After the solutions for the active strains $\mathbf{a}^{(0)}$ and $\mathbf{a}^{(1)}$ are obtained, the curvature and torsion of the model is calculated in the same way as in the case of without pre-strain case.

4.2.2 Shape of the embryo under muscles and acto-myosin contraction

Based on the model that we derived in the previous section 4.2.1, we specifically consider the case of *C. elegans* activities and obtain their deformation. The regulation of the muscle contraction in *C. elegans* detected experimentally [174] indicates a cyclic process, where two muscles contract on one side of the embryo quite simultaneously and then stop, while on the opposite side, the two muscles start their contractions, the time interval between contractions is approximately 40 seconds [174]. Let us consider first that only muscles are active (see the schematic Fig.4.4(a) for the structure, then (b) and (c) for the bending). In this case, due to the geometry, only a bending deformation occurs on the left for active muscles localized on the left and then on the right for the symmetric muscles on the right.

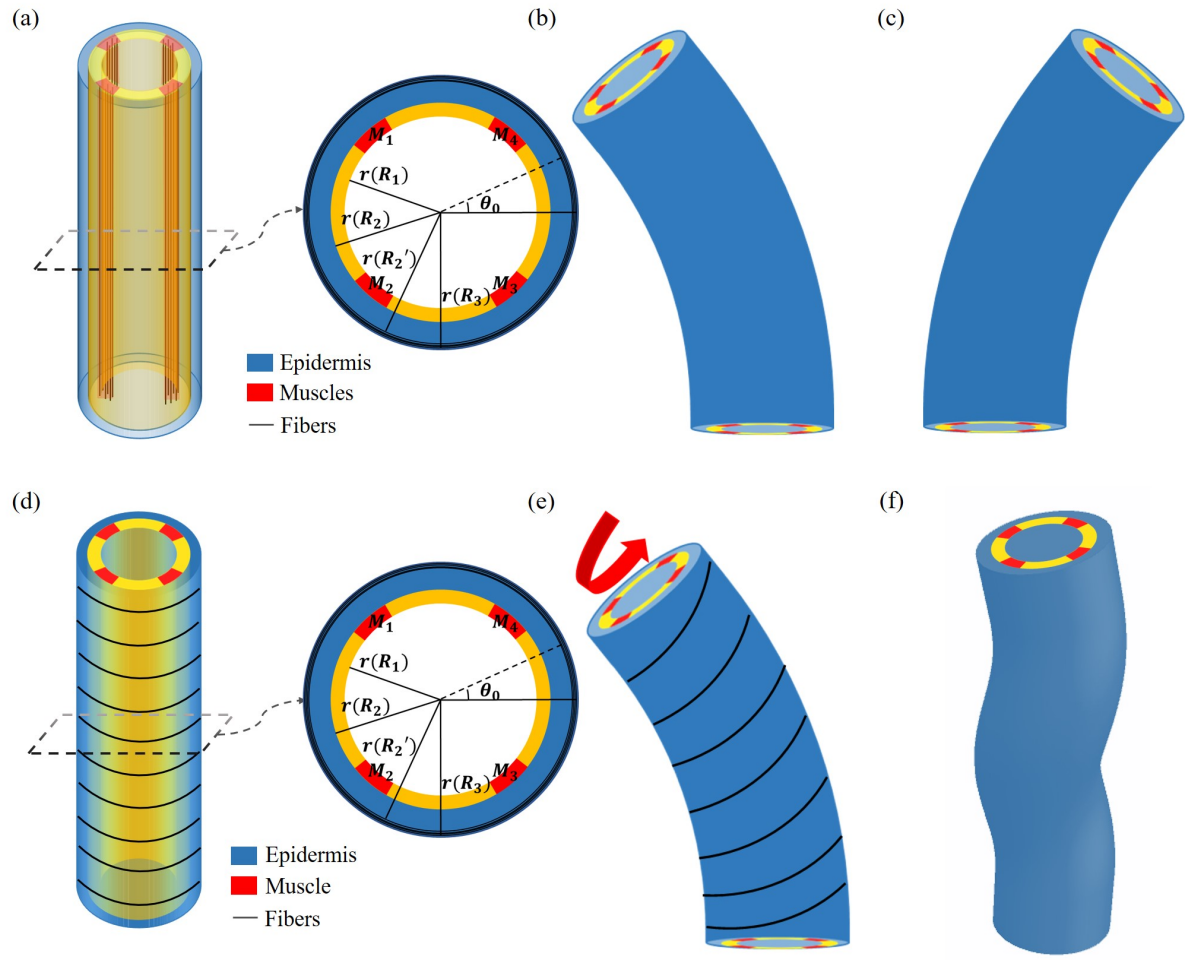

Figure 4.4 – (a) Schematic diagram of *C. elegans* muscle fibers and its cross section, and it does not show the actin fibers. Four muscle bands exist in the yellow layer. But, the yellow region is not an actual tissue layer and it is simply to define the position of muscles. (b) Deformation diagram, when left side muscles $M_1(\theta_1 \leq \theta_0 \leq \theta_2)$ and $M_2(\theta_3 \leq \theta_0 \leq \theta_4)$. (c) Deformation diagram, when right side muscles $M_3(\theta_5 \leq \theta_0 \leq \theta_6)$ and $M_4(\theta_7 \leq \theta_0 \leq \theta_8)$. (d) Schematic diagram of *C. elegans* actin fibers and cross-section. (e) Once the muscle is activated, the actin fiber orientation changes from the 'loop' to the 'slope', which results in torque. (f) Schematic diagram of torsional and bending deformation. (d) Schematic diagram of *C. elegans* actin fibers and cross-section. (e) Once the muscle is activated, the actin fiber orientation changes from the 'loop' to the 'slope', which result in torque. (f) Schematic diagram of torsional and bending deformation.

To be more quantitative, we assume that the left side muscles are activated during a short period with

an active constant strain value g_m in the region M_1 and M_2, as shown in Fig.4.4(a)-(b); if the muscles are perfectly vertical, $\alpha_m = \beta_m = 0$ in the initial configuration. In fact, the two muscles on the same side are not always fully in phase and one may present of small delay. For simplification, we assume they are perfectly synchronous. During the full initial period where muscles are not activated, the actin fibers are distributed in a horizontal loop on the outer surface of the epidermis, but once the muscle starts to contract, the acto-myosin network will be re-orientated [166]. The fibers will be then distributed in a sloping pattern causing eventually the twisting of the embryo, see the schematic diagram shown in Fig.4.4(d)-(f). When this region is activated with a constant strain value, g_a, the angle of the actin fibers will change following the amplitude of the bending by the muscle contraction. In this situation, the angle of the actin fibers may change from $\alpha_a \in \left[0, \frac{\pi}{2}\right]$ but β_a is not modified and $\beta_a = 0$.

Throughout the entire process, the muscle and acto-myosin activities are assumed to work almost simultaneously. Our modeling allows us to evaluate the bending and torsion generated independently by muscles and actin bundles, culminating in a complete deformation under coupling. We then discuss the deformation with and without pre-strain separately.

Without pre-strain case

Firstly, we consider the initial without the pre-strain case and calculate the curvature and torsion by Eq.(4.29) and parameters in Table.3.1. Fig.4.5(a)-(b) show that the curvature of the model rises as muscle activation increases and the torsion is not simply related to the activation amplitude of the actin but follows the angle α_a change, reaching a maximum at approximately $\pi/4$.

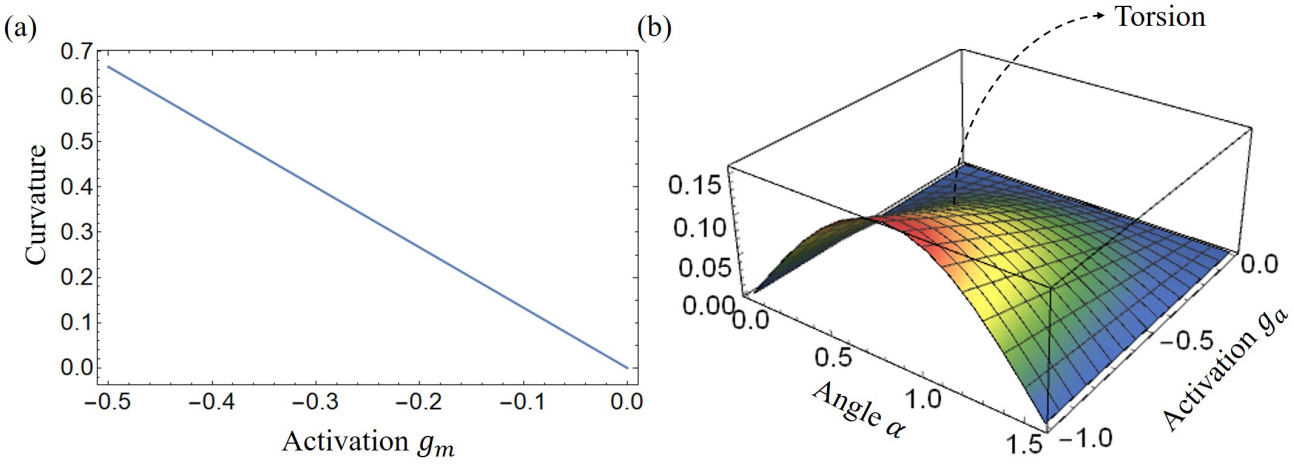

Figure 4.5 – Without pre-strain: (a) Curvature is plotted as a function of muscle activation. (b) Torsion is plotted as a function of the actin activation and angle of actin fibers.

Then, we show some deformation images of the model at different values of muscle activation g_m and acto-myosin activation g_a in Fig.4.6-Fig.4.8. These images demonstrate that our model can achieve different states of bending and torsional deformation.

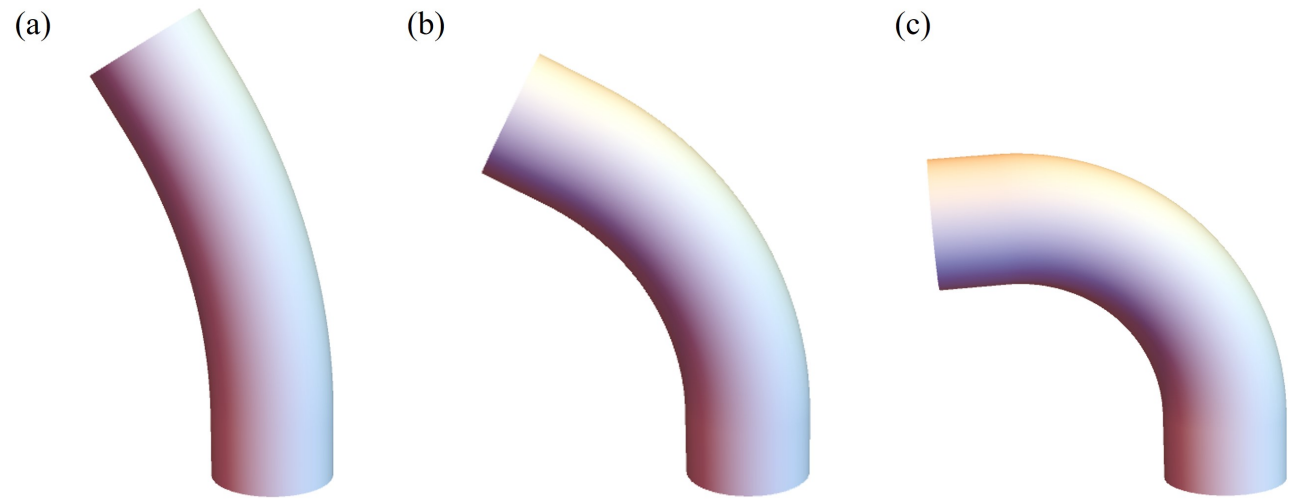

Figure 4.6 – Deformation images at different muscle activation ($g_a = -0.01$, $\alpha_a = \pi/3$): (a) $g_m = -0.005$, (b) $g_m = -0.01$, (c) $g_m = -0.015$.

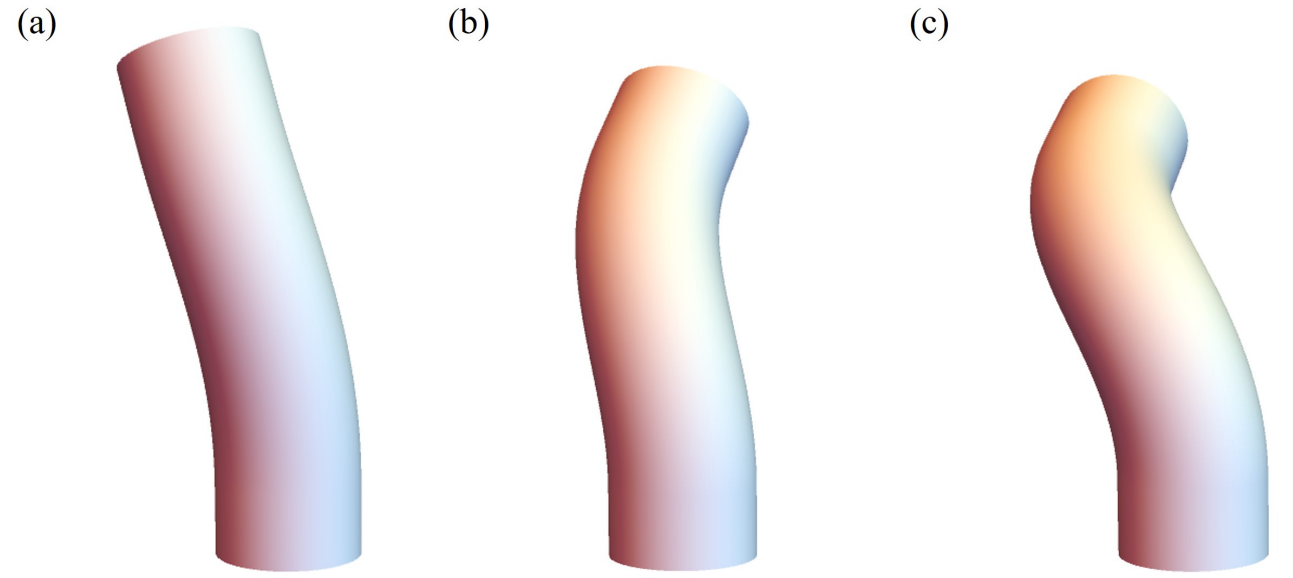

Figure 4.7 – Deformation images at different muscle activation ($g_a = -0.25$, $\alpha_a = \pi/3$): (a) $g_m = -0.005$, (b) $g_m = -0.01$, (c) $g_m = -0.015$.

Pre-strain case

To obtain an accurate depiction of the *C. elegans* deformation during the late elongation stage, it is imperative to account for the pre-strain of the early elongation phase. By employing Eq.(4.29) and the parameters specified in Table.3.1, we calculated the curvature and torsion of the worm and observed that the regulatory trends remained consistent with those observed in the absence of pre-strain. However, the magnitude of the bending and twisting values were notably different, as demonstrated in Fig.4.9. Specifically, we found that the absence of pre-strain led to greater bending and twisting for the same level of activation (g_a, g_m). This observation can be attributed to the fact that the model is constrained to maintain an elongated state in the presence of pre-strain, making it more resistant to deformation,

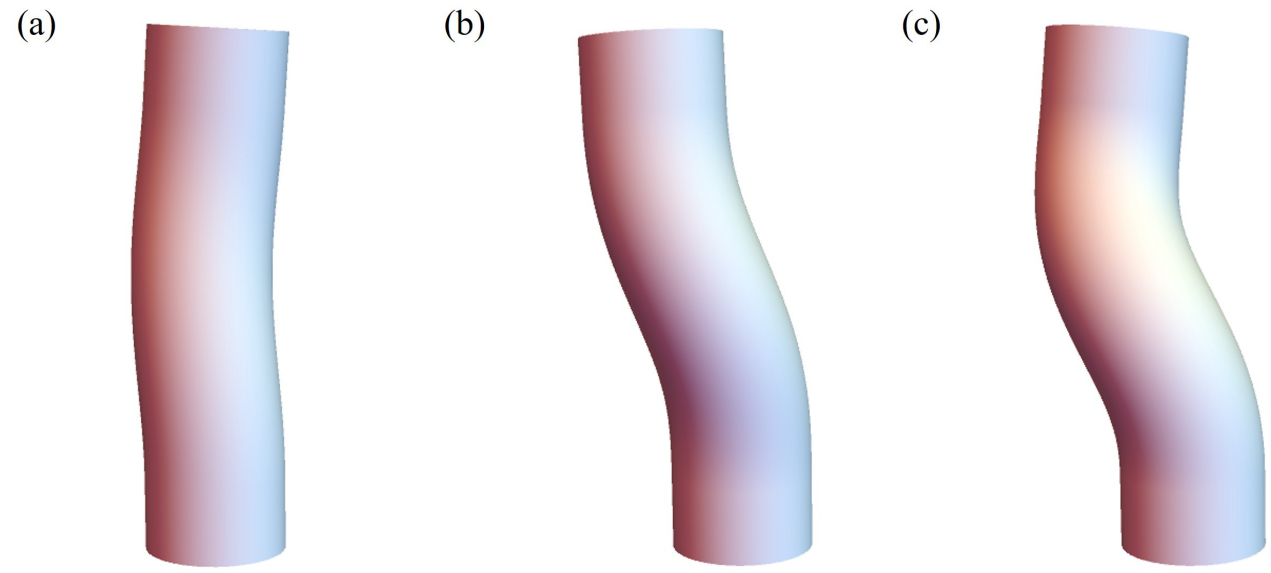

Figure 4.8 – Deformation images at different muscle activation ($g_a = -0.5$, $\alpha_a = \pi/3$): (a) $g_m = -0.005$, (b) $g_m = -0.01$, (c) $g_m = -0.015$.

including bending and twisting.

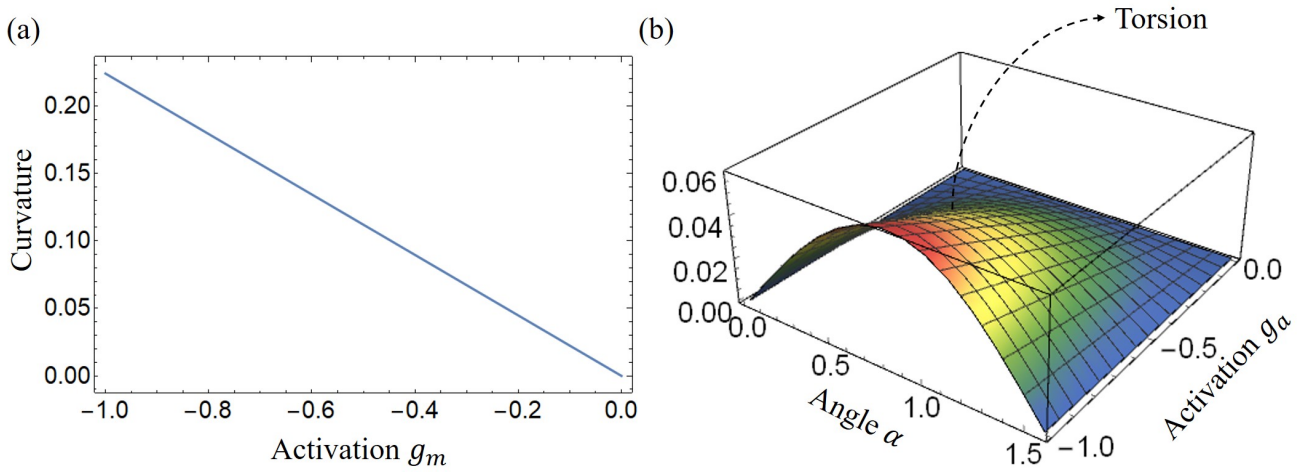

Figure 4.9 – The presence of pre-strain: (a) Curvature is plotted as a function of muscle activation. (b) Torsion is plotted as a function of the actin activation and angle of actin fibers.

To provide further evidence of the impact of the pre-strain on the deformation of the *C. elegans* model, we present a series of images in Figs.4.10-4.12. Notably, Fig.4.12(c) depicts a significant twisting deformation, which is closely similar to deformations observed in the DIC-optic video screenshot of *C. elegans* embryos captured at a temperature of 20^0C (Fig.4.13). However, it is important to mention that significant torsional deformations are not consistently present. Other factors, such as the lack of symmetry in the muscle axis, can also contribute to torsion, which we will discuss in detail later.

The outcomes of our study prove that pre-strain has a great influence on the deformation of the *C. elegans* model during the late elongation phase (after the muscle has been activated). This finding emphasizes the need to account for pre-strain while delving into the underlying mechanisms of late

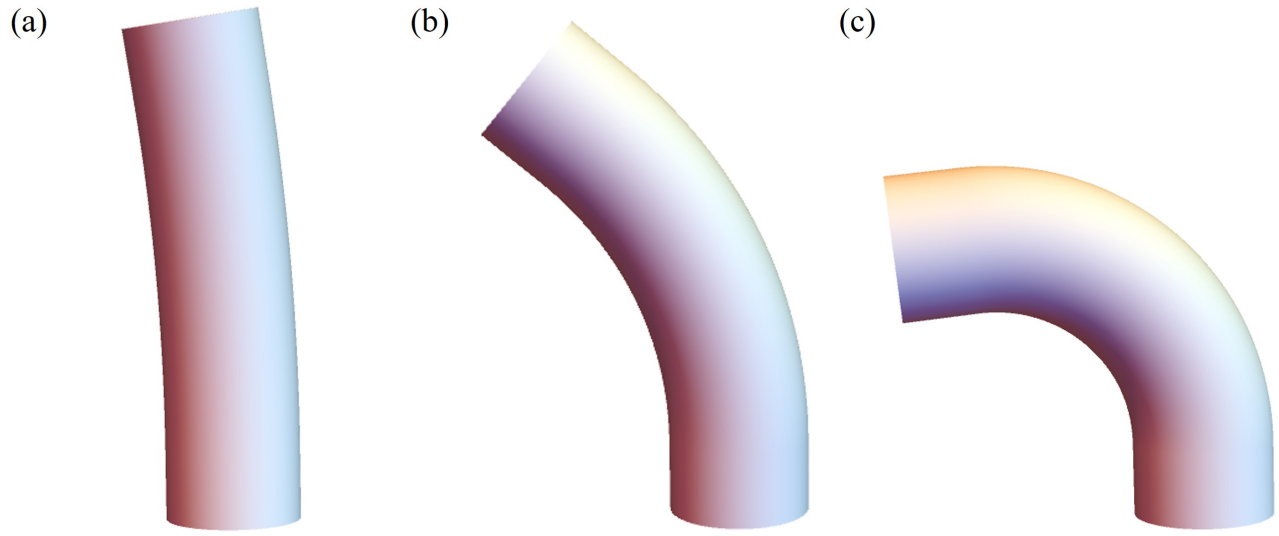

Figure 4.10 – Deformation images at different muscle activation ($g_a = -0.01$, $\alpha_a = \pi/3$): (a) $g_m = -0.01$, (b) $g_m = -0.05$, (c) $g_m = -0.1$.

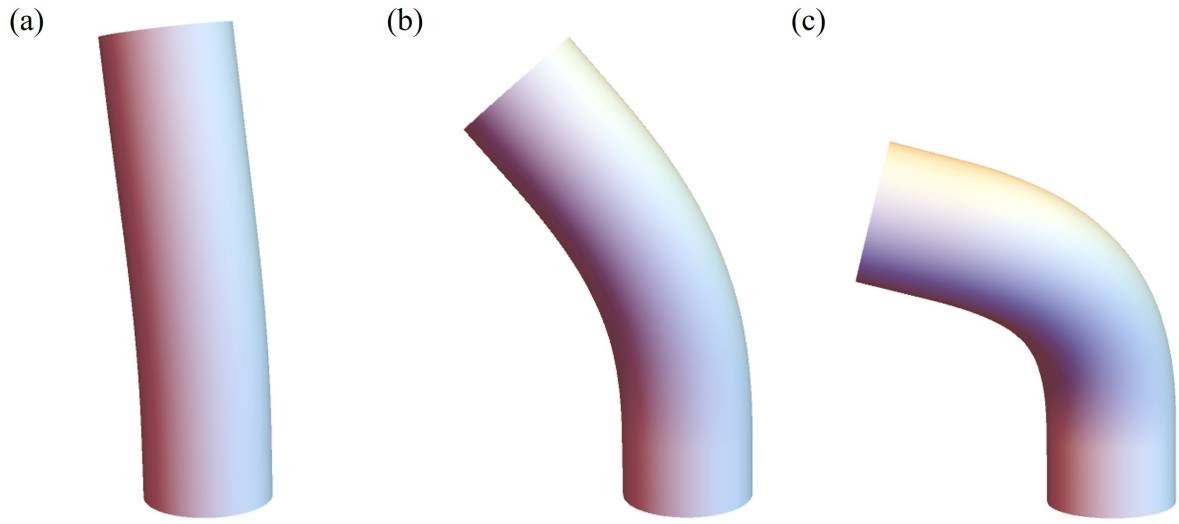

Figure 4.11 – Deformation images at different muscle activation ($g_a = -0.5$, $\alpha_a = \pi/3$): (a) $g_m = -0.01$, (b) $g_m = -0.05$, (c) $g_m = -0.1$.

elongation. Consequently, in the subsequent sections, we exclusively consider the pre-strain scenario.

Active matter similar to *C. elegans* can often be found in biological systems, from animals to plants as illustrated in Fig.4.14(a)-(c), they have a structure that generates internal stress/strain when growing or activity. Combining anatomy and measurement techniques, we can transform the mechanics of the body under study into a soft sample submitted to localized internal active stresses or localized internal active strains and then deduce its overall deformation mechanisms, some examples are presented in Fig.4.14(d)-(f).

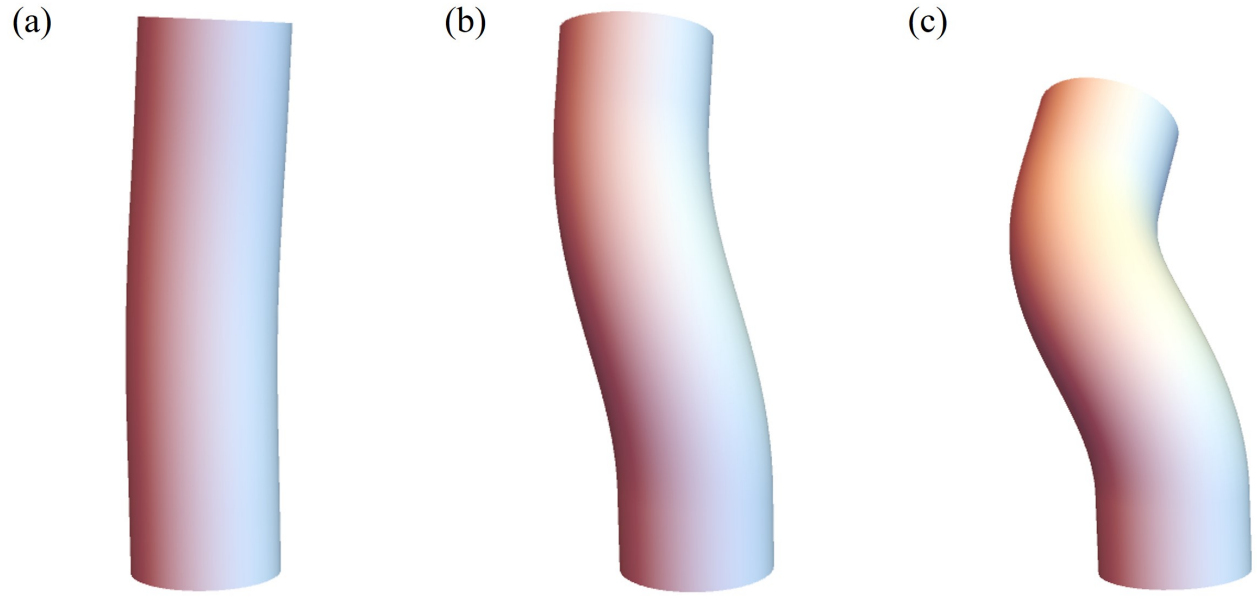

Figure 4.12 – Deformation images at different muscle activation ($g_a = -1$, $\alpha_a = \pi/3$): (a) $g_m = -0.01$, (b) $g_m = -0.05$, (c) $g_m = -0.1$.

Figure 4.13 – The graphs were captured from the Hymanlab and website: https://www.youtube.com/watch?v=M2ApXHhYbaw.

4.3 Energy transformation and Elongation

During the late elongation process, the four internal muscle bands cyclically contract in pairs [163, 174]. Each contraction of a pair increases the energy of the system under investigation, which is then rapidly released to the body. This energy exchange causes the torsion-bending energy to convert into elongation energy, leading to a length increase during the relaxation phase, as depicted in Fig.4.15. With all deformations obtained, Eq.(4.67) in Appendix4.C can be used to calculate the accumulated energy W_c produced by both the muscles and the acto-myosin activities during a contraction. Subsequently, when the muscles on one side relax, the worm body reverts to its original shape but with a tiny elongation corresponding to the transferred elastic energy. This new state involves the actin network adopting a 'loop' configuration with a strain of εg_{a1} once relaxation is complete. If all accumulated energy from the bending-torsion deformation goes towards elongating the worm body, the accumulated energy W_c and energy W_r following muscle relaxation are equivalent. The activation of actin fibers g_{a1} after muscle relaxation can be calculated and determined by our model.

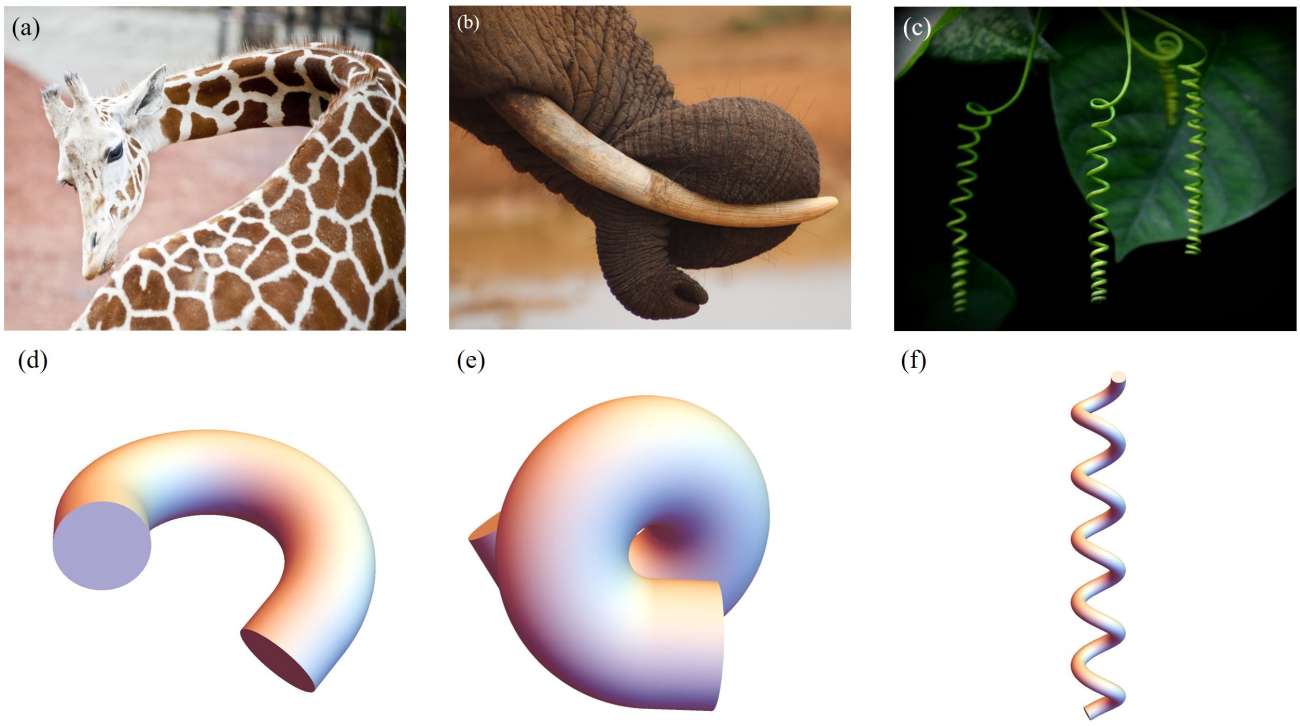

Figure 4.14 – (a) Bending of a Giraffe neck. (b) Torsion of an Elephant trunk. (c) Plant vine twisting. (d) to (f) Deformation configuration under different activations obtained by our simulations for bending and torsion of large rods, twisting and torsion of thin rods.

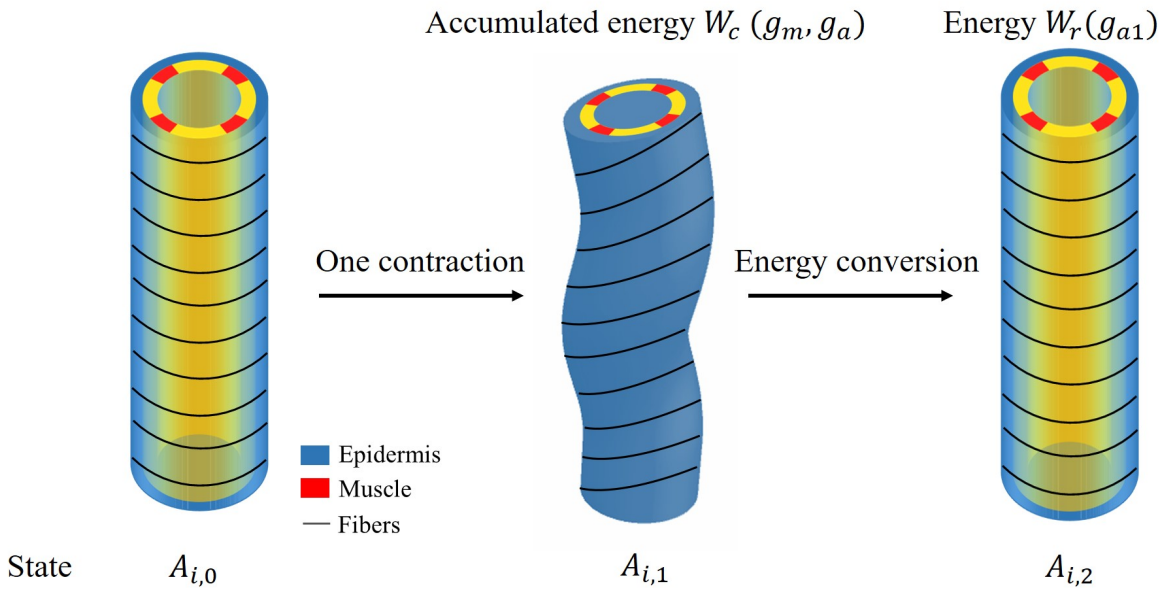

Figure 4.15 – Schematic diagram of energy conversion.

Once the first stage is well characterized, we can quantify the total energy resulting from both muscles and acto-myosin after each contraction. Then, we used our model to predict elongation in the wild-type *C. elegans*, unc-112(RNAi) mutant and spc-1(RNAi) pak-1(tm403) mutant and further compared the results with experimental observations. The length of the wild type elongates from approximately $90\ \mu m$ to $210\ \mu m$ during the muscle-activated phase [166], the phase lasts about 140 minutes, and the

average time interval between two contractions is about 40 seconds [174], so the number of contractions can be estimated to be around 210 times. Unfortunately, due to the difficulty of realizing quantitative experiments on an embryo always in agitation in the egg shell between bending, torsion, and rotations around its central axis, one can hypothesize several scenarios: at each step i between state $A_{i,0}$ to $A_{i,1}$ and then $A_{i,2}$, the whole mechanical muscle-myosin energy is transferred to the elongated step $A_{i,2}$, leading to a small $\delta\zeta_i$.

Considering the experimental results shown in Fig.4.16(b), we determine the optimal values for the activation parameters: $g_m = -0.15$ and $g_a = -0.01$ assuming that all the accumulated energy during muscle activation is transferred to elongation($W_r = W_c$). The elementary elongation $\delta\zeta_i$ will be gradually increased with time, which is shown as the black line in Fig.4.16(a). At the beginning, $\delta\zeta_i$ is about $0.5\mu m$, but at the end of this process, $\delta\zeta_i$ is about $1.5\mu m$, indicating that the worm will elongate up to $290\mu m$. The result is significantly higher than our actual size $210\mu m$. When the elongation proceeds, we assume a transfer of energy between bending-torsion-contraction and elongation but it may be not fully effective, which means a significant part of the energy is lost. From the experimental data, we evaluate that the energy loss gradually increases, from full conversion at the beginning to only 40% of the accumulated energy used for elongation at the end of the process ($W_r = 0.4W_c$). It induces for $\delta\zeta_i$ a first increase and then a decrease, which is shown as the blue line in Fig.4.16(a) and is responsible for the slowdown around 200 mins. This option, which may be not the only possible one, leads to the estimated elongation having a good agreement with experimental data (see the blue-dashed curve in Fig.4.16(b)). Indeed it is possible that the *C. elegans* elongation requires other transformations which will cost energy. As the embryo gradually elongates, energy dissipation and the biomechanical energy required to reorganize the actin bundles may be two factors that contribute to the increased energy loss that underlies the hypothesis.

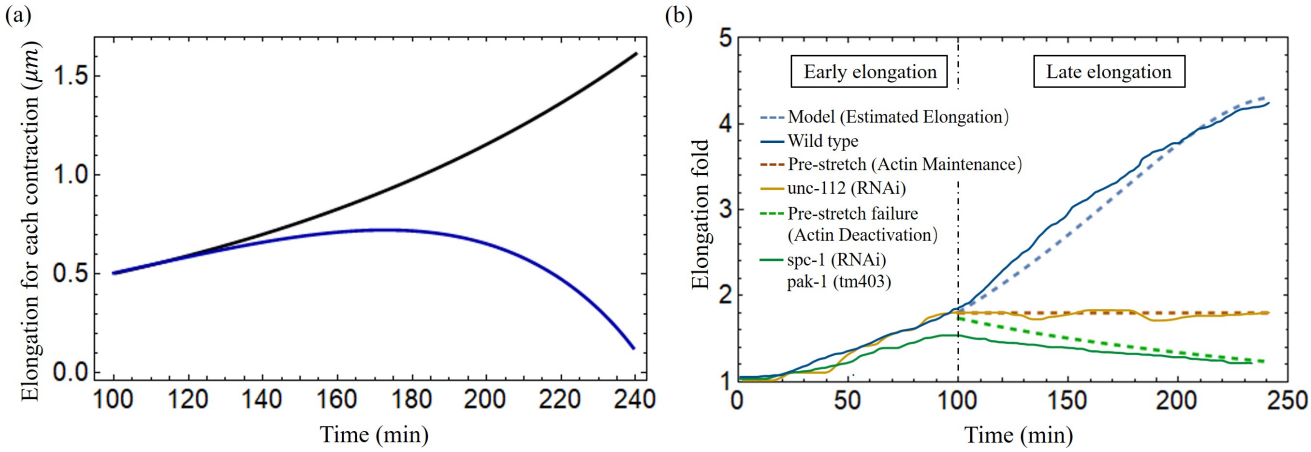

Figure 4.16 – (a) The elongation for each contraction varies with time. Black line: all energy converted to the elongation, blue line: partial energy converted to the elongation. The activation: $g_m = -0.15$, $g_a = -0.01$. (b) The model predicted results agree well with the experimental data of wild-type and different mutant *C. elegans* embryos [166]. The activation of wild type model (blue dashed line): $g_m = -0.15$, $g_a = -0.01$. The activation of unc-112(RNAi) (brown dashed line): $g_m = 0$, $g_a = 0$. In the pre-stretch failure case (green dashed line), λ will decrease from 1.8.

Moreover, it was reported in [190] that the knockdown of unc-112(RNAi), known for impairing

muscle contractions, results in the arrest of elongation of embryos at the twofold stage, indicating that muscles have no activation, $g_m = 0$ in our model, and no accumulated energy can be converted into elongation. Another mutation concerning the embryos consisting of mutant cells with pak-1(tm403), known to regulate the activity of myosin motors leads to a retraction of the embryo, so the pre-stretch caused by myosin will not be maintained and will decrease. These aforementioned findings are fully consistent with a variety of experimental observations and are shown in Fig.4.16(b). More calculation details in Appendix4.C.

4.4 Embryo rotations and dissipation

The main manifestation of the muscle activity, independently of the elongation, is probably the constant rotations of the embryo despite its confinement in the egg. This can be explained by a small angular deviation of the muscle sarcomeres from the central axis due to their attachment to the inner boundary of the cell epidermis, the so-called "dense bodies" [167]. Since they cross the horizontal plane at approximately $\pm 45°$ and the deviation β_m from the vertical axis is estimated to be about $6°$ each active muscle on the left (or on the right) contributes to the torque via a geometrical factor about $a_g = \sin(6\pi/180)\cos(\pi/4)$. Then a simple estimation of the muscle activity in terms of torque reads

$$\Lambda_m \sim \mu_m \pi R^3 s_m p_m a_g(\varepsilon g_m), \tag{4.42}$$

where s_m is the surface of the muscle pair on the left (or right) compared to the section of the cylinder: $s_m = 0.025$ and p_m is the distance of the muscles from the central axis of the embryo: $p_m = 0.75$ while $g_m = 0.15$ according to the analysis of the elongation. So the muscles on one side contribute to a torque Λ_m along the axis of symmetry given by $\Lambda_m = 4.657\mu_m \pi R^3 \cdot 10^{-5}$.

Let us consider now the dissipative torque, assuming that the dynamics of rotation is stopped by friction after one bending event. Two cases can be considered: either the dissipation comes from viscous flow or from the rubbing of the embryo when it folds. The fluid dissipation results from the rotations in the interstitial fluid inside and along the egg shell. The interstitial fluid, of viscosity η contains a significant amount of sugar and other molecules which are required for embryo survival and then is more viscous than water [191]. However, values for sucrose or sorbitol at the concentration of 1 mole/liter indicates a viscosity of order a few times the viscosity of water, which is 1 mPas. For example at 0.9 mole/liter and temperature of $20°$, an aqueous solution with sorbitol has a viscosity of 1.6 mPas, which can be extrapolated to $\eta = 1.9$ mPas at 1.2 mole/liter [192]. The estimation given by an embryo located in the middle of the egg-shell, gives a weaker viscous torque once evaluated by

$$\Lambda_v = 4\pi\eta\Omega_e L R^2 \left(R_{egg}^2/(R_{egg}^2 - R^2)\right), \tag{4.43}$$

according to a classical result reported by Landau *et al.* [193, 194]. It has to be mentioned that this estimation assumes that the two cylinders: the egg shell and the embryo have the same axis of symmetry and concerns the beginning of the muscle activity where the radius is about $8.2\,\mu m$, the length is $90\,\mu m$,the radius of the shell about $R_{egg} = 15\mu m$ and the length $L_{egg} = 54\mu m$, see Fig.4.13. The angular velocity Ω_e is more difficult to evaluate but it is about $90°$ per two seconds deduced from videos. When the em-

bryo approaches the egg shell, the friction increases, and two eccentric cylinders of different radii have to be considered with the two axes of symmetry separated by a distance d. The hydrodynamic study in this case is far from being trivial, and seems to have been initiated first by Zhukoski [195] who suggested the use of bipolar coordinates for the mathematical treatment. Many following contributions established with different simplified assumptions have been published after and the study was fully revisited by Ballal and Rivlin [196]. Here we focus on the limit of a small gap δ between the rotating body-shape and the egg and by considering an asymptotic analysis at small δ of the general result derived in [196]. Thus, the viscous torque reads

$$\tilde{\Lambda}_v = 2\sqrt{2}\pi\eta\Omega_e L_c R_{egg}^2\sqrt{R_{egg}/\delta}\sqrt{(R_{egg}-d)/d}. \tag{4.44}$$

L_c is the zone of contact with the egg and $d = R_{egg} - \delta - R$. This approach is an approximation since the embryo has more of a torus shape than a cylinder [174] but the evaluation of the dissipation is satisfactory for $\delta = 0.5\mu m, \Omega_e \sim \pi/4\, s^{-1}$ and $\mu = 10^5 Pa$. Coming back to the first model of dissipation with the same data, the ratio between the dissipative viscous torque and the active one gives: $\Lambda_v/\Lambda_m = 0.02$, which is obviously unsatisfactory. Finally, the dissipative energy $\mathcal{E}_{diss}$ during one bending event leading to an angle of $\pi/2$ is $\mathcal{E}_{diss} = 1/2\Lambda_m \times (\pi/2)^2$ which represents 4% of the muscle elastic energy during the bending so at the beginning of the muscle activity (Appendix4.C, Eq (4.69)), the dissipation exits but is negligible. At the very end of the process, this ratio becomes 60% but as yet mentioned our estimation for the dissipation becomes very approximate, increases a lot due to the embryo confinement, and does not involve the numerous biochemistry steps necessary to reorganize the active network: acto-myosin and muscles.

4.5 Discussion and conclusion

Since the discovery of the muscle activity before the egg hatch of the *C. elegans* embryo, it has become critical to explain the role of mechanical forces generated by muscle contraction on the behavioral and functional aspects of the epidermis. We provide a mechanical model in which the *C. elegans* is simplified as a cylinder, and the muscle bands and actin that drive its elongation are modeled as active structures in a realistic position. We determine the fiber orientation using experimental observations and then calculate the deformation by tensorial analysis involving the strains generated by the active components. Although a special focus is made on late elongation, its quantitative treatment cannot avoid the influence of the first stage of elongation due to the acto-myosin network, which is responsible for a pre-strain of the embryo. In a finite elasticity formalism, the deformations induced by muscles in a second step are coupled to the level of strains of the initial elongation period. For that, we need to revisit the theory of the acto-myosin contraction and previous results [4, 138, 177] to unify the full treatment. We discuss the early elongation induced by pre-strain in the chapter 3.

The elongation process of *C. elegans* during the late period is much more complex than the early elongation stage which is caused only by actin contraction. During the late elongation, the worm is distorted by the combined action of muscle and acto-myosin, resulting in an energy-accumulating process. Bending deformation is a phenomenon resulting from unilateral muscular contraction, and during

the late elongation, significant torsional deformation is observed, indicating that the bending process induces a reorientation of the actin fibers. It is worth noting that the embryo is always rotating in tandem with the muscle activity making difficult any experimental measurements. However, our model can predict that if the muscles are not perfectly vertical, torque exits that causes rotation and eventually torsion. The accumulated energy is then partly turned into energy for the ongoing action of actin, allowing the embryo to elongate when the muscle relaxes. Both sides of the *C. elegans* muscles contract in a sequential cycle, repeating the energy conversion process, and eventually completing the elongation process. However, the energy exchange between bending and elongation is limited, among other factors, by the viscous dissipation induced by rotation, which is also evaluated in this study. Not investigated in detail here is the necessary re-organization of the active networks (acto-myosin and muscles) due to this tremendous shape transformation of the embryo. In parallel to elongation, the cuticle is built around the body [197]. This very thin and stiff membrane ensures protection and locomotion post-hatching. Clearly, these processes will perturb muscle activity. These two aspects which intervene in the final stage of the worm confinement play a very important role at the frontier across scales between genetics, biochemistry and mechanics. The architecture of the work in Part II is illustrated in Fig.4.17.

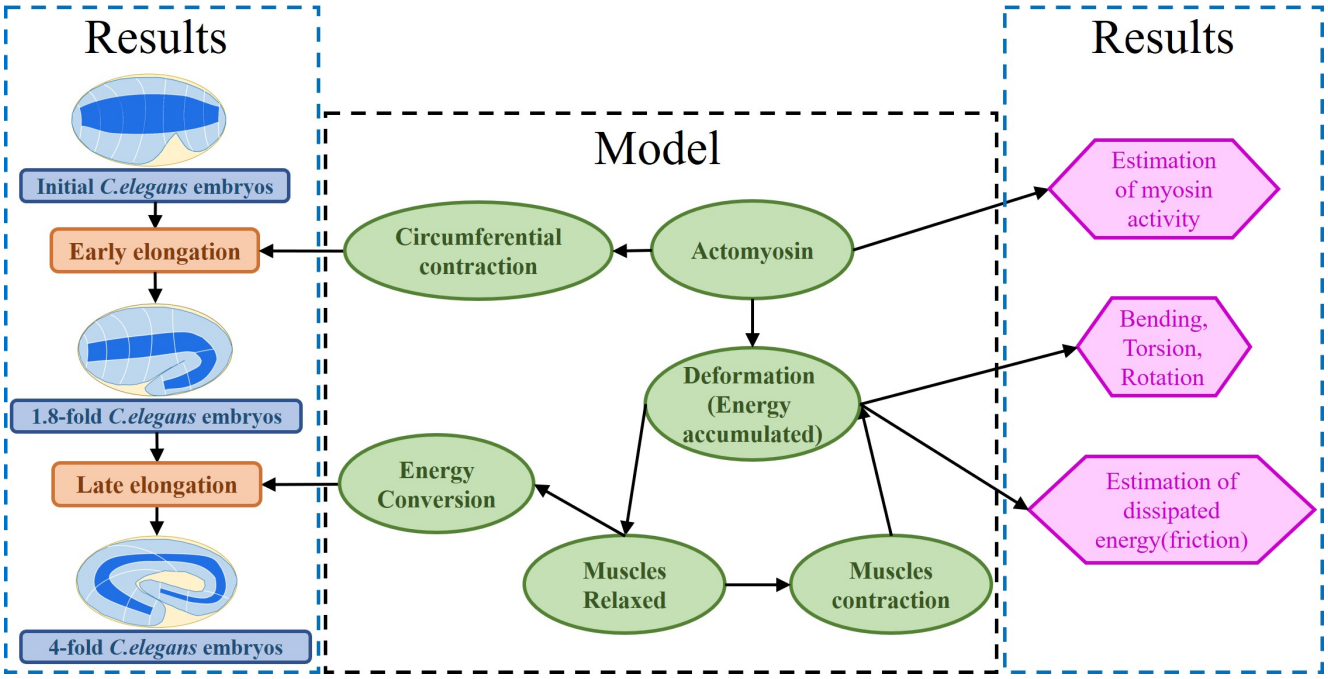

Figure 4.17 – Architecture of the program. The program reflects the framework of research. On the one hand, the proposed model explains the early and late elongation of the *C. elegans*, on the other hand, the early myosin activity is estimated, the deformations (bending, twisting, rotation) happening in the late period is recovered, and the estimation of energy dissipated during muscle activity is achieved.

Finally, the framework presented here not only provides a theoretical explanation for embryonic elongation in *C. elegans*, it can also be used to model other biological behaviors, such as plant tropism [180] and elongated elephant trunk [198, 199] and bending. Our ideas could potentially be used in the emerging field of soft robotics, like octopus legs-inspired robots [200, 201, 202], which is soft and its deformation induced by muscles activation. We can reliably predict deformation by knowing the position of activation and the magnitude of forces in the model. Furthermore, residual stresses can be incorporated into our model to fulfill design objectives.

APPENDICES

Appendix 4.A Modelling details of without pre-strain case

The first order solutions of the theory with the pre-strain case, $f_{1,2,3}(R)$ are related to activation g and fiber angles α and β:

$$f_1(R) = \frac{gR}{2}, \tag{4.45}$$

$$f_2(R) = glog(R)\sin^2\alpha\sin(2\beta), \tag{4.46}$$

$$f_3(R) = 2g\mu log(R)\sin^2\alpha\sin(2\beta). \tag{4.47}$$

The coefficients for determining stiffness:

$$A_2 = \frac{9\mu R}{8}, \tag{4.48}$$

$$B_2 = \frac{81}{128}\mu R^3\sin^2\Theta, \tag{4.49}$$

$$C_2 = \frac{81}{128}\mu R^3\cos^2\Theta, \tag{4.50}$$

$$D_2 = \frac{\mu R^3}{2}. \tag{4.51}$$

The coefficients for determining deformation:

$$A_1 = -\frac{1}{8}g\mu R\left[4 + 5\cos(2\alpha) + 2\cos(2\beta)(-1 + 2\log(R))\sin^2\alpha\right], \tag{4.52}$$

$$B_1 = -\frac{1}{16}g\mu R^2\left[10 + 17\cos(2\alpha) + 2\cos(2\beta)(-1 + 14\log(R))\sin^2\alpha\right]\sin\Theta, \tag{4.53}$$

$$C_1 = \frac{1}{16}g\mu R^2\left[10 + 17\cos(2\alpha) + 2\cos(2\beta)(-1 + 14\log(R))\sin^2\alpha\right]\cos\Theta, \tag{4.54}$$

$$D_1 = -g\mu R^2 \cos\beta \sin(2\alpha). \tag{4.55}$$

Appendix 4.B Modelling details of with pre-strain case

The first order solutions of the theory with the pre-strain case, $h_{1,2,3}(R)$ are related to activation g and fiber angles α and β:

$$h_1(R) = \frac{R(c+g)}{2\sqrt{\lambda}}, \tag{4.56}$$

$$h_2(R) = g\log(R)\sin^2\alpha \sin(2\beta), \tag{4.57}$$

$$h_3(R) = \frac{2\mu log(R)\left[c + g\cos(2\beta)\sin^2\alpha\right]}{\lambda}. \tag{4.58}$$

The coefficients for determining stiffness:

$$A_2 = (0.278 + 1.689\mu) R, \tag{4.59}$$

$$B_2 = 1.294R^3\left[-0.405 + 2.389\mu + (-0.176+\mu)\cos(2\Theta)\right], \tag{4.60}$$

$$C_2 = -1.294R^3\left[0.405 - 2.389\mu + (-0.176+\mu)\cos(2\Theta)\right], \tag{4.61}$$

$$D_2 = 0.9\mu R^3. \tag{4.62}$$

The coefficients for determining deformation:

$$\begin{aligned} A_1 = \mu R\big[&0.417c - 0.139g - 6.48g\cos^2\alpha - 0.556c\log(R) \\ &+ g\left(0.556\cos^2\beta - 0.556\cos(2\beta)\log(R)\right)\sin^2\alpha\big], \end{aligned} \tag{4.63}$$

$$\begin{aligned} B_1 = R^2 \big\{ & g\left(-0.828+4.830\mu\right)\cos\beta\log\left(R\right)\sin^2\alpha\sin\beta\cos\Theta + 0.198c\sin\Theta \\ & + \big[0.198g + 0.910c\mu + 1.307g\mu - 4.830g\mu\cos^2\alpha - 1.225c\mu\log\left(R\right) \\ & + g\mu\left(-0.397\cos^2\beta - 1.225\cos\left(2\beta\right)\log\left(R\right)\right)\sin^2\alpha\big]\sin\Theta\big\}, \end{aligned} \tag{4.64}$$

$$\begin{aligned} C_1 = R^2 \big\{ & g\left(-0.828+4.830\mu\right)\cos\beta\log\left(R\right)\sin^2\alpha\sin\beta\sin\Theta - 0.198c\cos\Theta \\ & + \big[-0.198g - 0.910c\mu - 1.307g\mu + 4.830g\mu\cos^2\alpha + 1.225c\mu\log\left(R\right) \\ & + g\mu\left(0.397\cos^2\beta + 1.225\cos\left(2\beta\right)\log\left(R\right)\right)\sin^2\alpha\big]\cos\Theta\big\}, \end{aligned} \tag{4.65}$$

$$D_1 = -g\mu R^2\cos\beta\sin\left(2\alpha\right). \tag{4.66}$$

Appendix 4.C Energy transformation calculations

To obtain the elongation $\delta\zeta_i$ after each muscle contraction, we need to calculate the energy, and the total energy takes the following form:

$$\mathcal{E} = \varepsilon^2\int_0^L \mathrm{d}Z\int_S \left(V_0 + \varepsilon V_1 + \varepsilon^2 V_2\right)R\,\mathrm{d}R\,\mathrm{d}\Theta + O\left(\varepsilon^5\right) \tag{4.67}$$

where the integration region S is related to each part of the cylinder with a different shear modulus μ, so the model must be divided into 3 different parts for integration.

The final part of the energy conversion per unit volume is then:

$$\mathcal{E}_\prime = \int_S \left(\varepsilon V_1 + \varepsilon^2 V_2\right)R\,\mathrm{d}R\,\mathrm{d}\Theta \tag{4.68}$$

where V_1 is not the whole first order energy, we only consider the energy induced by activation of acto-myosin g_a and muscles g_m. After obtaining solutions $\mathbf{a}^{(0)}$,$\mathbf{a}^{(1)}$ and deformations from Eq.(4.35)-(4.40), the accumulated energy during the contractile period W_c that we define is:

$$\begin{aligned} W_c &= \int_S \left(\varepsilon V_1 + \varepsilon^2 V_2\right)R\,\mathrm{d}R\,\mathrm{d}\Theta \\ &= \varepsilon\left(-10.70g_a - 7.73g_m\right) + \varepsilon^2\left[\left(-3.31 + 26.75g_a\right)g_a + 11.95{g_m}^2\right]. \end{aligned} \tag{4.69}$$

When the muscles are relaxed and only acto-myosin is activated, the total increase of volumetric energy W_r is then:

$$\begin{aligned} W_r &= \int_S \left(\varepsilon V_1 + \varepsilon^2 V_2\right)R\,\mathrm{d}R\,\mathrm{d}\Theta \\ &= -0.41\varepsilon g_{a1} + \varepsilon^2\left(-5.19 + 6.96g_{a1}\right)g_{a1}. \end{aligned} \tag{4.70}$$

By calculating energy conversion, we obtain $g_{a1} = -0.66$ at the beginning of the late elongation phase,

Fig.4.16(a)-(b) shows the elongation for each contraction and total elongation varies with time.

Chapter 5

Conclusions and perspectives

The central focus of this chapter is to summarize and discuss all the work of this thesis, while also providing a concise outlook on the research implications and directions for future investigation.

Conclusion

In Chapter 1, our primary focus lies in elucidating the background of our study, encompassing the current research landscape as well as the theoretical underpinnings. Subsequently, our thesis consists of two parts work, with the first part, i.e., Chapter 2, devoted to a comprehensive exploration of stress-free growth. Based on the principle of energy minimization, we have rigorously demonstrated theoretically that a conformal or quasi-conformal mapping between two planar configurations can eliminate the effect of elastic stress on soft tissue growth. Darcy Thompson hypothesized over a century ago that the morphological evolution of organisms correlates with the evolution of shape, and our conclusions make the first connection between morphological change and shape transformation in stress-free growth and are verified by naturally growing planar leaves. The second part is devoted to studying a model of the elongation process in *C. elegans* embryos before hatching. Chapter 3 focuses on the early elongation of the *C. elegans* under the influence of acto-myosin and is the basis for the study of the late elongation stages. Chapter 4 continues the study in Chapter 3 and focuses on the role of muscle activity in late elongation. We present a coupled bio-mechanical analytical model that considers the actual structure of worm biology. The model translates biochemical stimuli into driving forces and describes in detail all the deformations that occur during elongation. It also explains that actin contraction leads to partial elongation (80%), followed by successive bending events accompanied by twisting and rotation due to periodic contraction of the muscle. Each event accumulates elastic energy that is transferred to the circumferential actin network, which then causes the embryo to increase in length. Our model shows good agreement with experimental results for both wild-type and mutants. We demonstrate that the balance of energy encompasses the entire elongation process and dissipation and retains the remaining energy, which could explain the actin reorganization induced by this very important elongation process. Notably, for the first time, the non-negligible rotation based on muscle activity and the viscous torque generated by the interstitial fluid inside the egg shell was evaluated.

Personal thoughts

This thesis investigates the development of two biological species, one of them is a plant and the other is an animal, and the scales differ greatly. However, both studies are based on the same basic theory and both are dedicated to the study of how stress or growth of biological tissues acts to influence their morphological development and changes.

The study of morphological changes in stress-free growth of 2D dimensional organisms was initiated by extending the theoretical derivation proposed by Xiaoyi Chen *et al.* [3]. Although the derivation process was initially complicated, we still continued to explore its application after obtaining the desired conclusion. Eventually, after a long time, we discovered that the same conclusion could be reached through a simpler derivation. This realization led us to understand that if a conclusion is correct, there must be more than one way to prove it. This approach allows us to use different methods to verify the results, while also finding the most concise way to prove them. Simple theoretical derivations not only make the research easier to understand and use, but also have profound implications for its application.

The second point I realize is that when attempting to establish a relationship between the morphology of biological tissues and mathematical functions, intuition and experience play a crucial role. In our research on stress-free growth of leaves [136], we did not explained in detail how we arrived at the correct function to recover the contours of leaves and their main characteristic, as it was not a straightforward task. Fortunately, Martine possessed significant experience, particularly with Hele-Shaw bubbles. With the aid of many previous research [203, 204, 205, 206, 207, 208, 209], we eventually accomplished the task by continuously attempting to determine the appropriate parameters. Notably, the coincidence of using the analytical solution to a classic hydrodynamics problem to understand the fenestration process of the *Monstera* leaf is a remarkable natural phenomenon.

Finally, working with biologists is very interesting and challenging. Despite their extensive experience, experimental results are often difficult to control. This uncontrolled nature can often make theoretical work difficult to carry out. Nonetheless, it is necessary to work together, as the experience and intuition of the theoretician can often provide ideas for conducting experiments, and the experimental results can validate the theory. This is where the second part of our work comes in.

Perspectives

While this thesis has made progress in advancing our understanding of the two-dimensional stress-free growth of leaves, there remain several directions for future research. One such area pertains to leaves exhibiting buckling morphology, which demands further exploration and refinement of the Föppl-vonKármán theory. Specifically, we plan to extend this theory to the complex plane to more accurately model stress-free growth followed by buckling under stress. Additionally, the crumpling phenomenon of dead leaves during autumn draws our attention, further research will be carried out afterward.

In this thesis, the study of the growth and development of organisms such as *C. elegans* focus on their morphogenesis as a result of the driving forces generated by biological signals. In fact, during their growth and development, organisms achieve growth through the absorption of nutrients or other factors

that enable an increase in biochemical energy, while these active substances can sense the surrounding mechanical and biochemical environment, gradually adjusting the temporal and spatial distribution of growth and releasing biochemical signals that produce active deformations capable of adapting to environmental changes. This true state of activity and the fundamental characteristics of growth are required to consider how stress and biochemical signals interact. Therefore, it is necessary to experimentally track the spatial and temporal distribution patterns of biochemical and mechanical signals and to build a theoretical model of mechanical-chemical-growth coupling. This research will help to understand the relevant life processes at different scales and provide new ideas for disease diagnosis and treatment. The research results can deepen the understanding of important physiological processes such as embryonic development, tissue/organ growth and wound healing, and further provide new possible avenues for quantitative research and clinical prevention and treatment of related diseases such as tumors.

Appendix A

Publications

Featured in Physics

Minimizing the Elastic Energy of Growing Leaves by Conformal Mapping

Anna Dai and Martine Ben Amar*
Laboratoire de Physique de l'Ecole normale supérieure, ENS, Université PSL, CNRS, Sorbonne Université, Université Paris Cité, F-75005 Paris, France

(Received 20 March 2022; accepted 5 October 2022; published 16 November 2022)

During morphogenesis, the shape of living species results from growth, stress relaxation, and remodeling. When the growth does not generate any stress, the body shape only reflects the growth density. In two dimensions, we show that stress free configurations are simply determined by the time evolution of a conformal mapping which concerns not only the boundary but also the displacement field during an arbitrary period of time inside the sample. Fresh planar leaves are good examples for our study: they have no elastic stress, almost no weight, and their shape can be easily represented by holomorphic functions. The growth factor, isotropic or anisotropic, is related to the metrics between the initial and current conformal maps. By adjusting the mathematical shape function, main characteristics such as tips (convex or concave or sharp-pointed), undulating borders, and veins can be mathematically recovered, which are in good agreement with observations. It is worth mentioning that this flexible method allows us to study complex morphologies of growing leaves such as the fenestration process in *Monstera deliciosa*, and can also shed light on many other 2D biological patterns.

DOI: 10.1103/PhysRevLett.129.218101

During morphogenesis or embryogenesis, biological species grow very slowly, often creating important shape transformations at the origin of elastic stresses. In recent years, the theoretical framework of finite elasticity with multiplicative decomposition [1–3] was employed to understand and mimic these shape transformations; for instance, the development of leaves or flowers [4–6], the morphological instabilities of human organs in fetal life, including the brain cortex [7], the fingerprints [8,9], the oesophagus mucosa [10], and the intestine villi [11–13]. For slender soft bodies with initially a rather symmetric shape, the growth may change drastically their aspect with curling and buckling [10,14,15], and these instabilities perfectly illustrate the successive bifurcation steps induced by the relative volume increase G. Thin bilayers exhibit zigzag instabilities [12,16–18] in the same way as fluids in Rayleigh-Bénard convection [19,20] or localized solitonic patterns in the presence of defects [21]. However, due to the complexity of finite elasticity, most of the theoretical works describe simple highly symmetric bodies, such as thin plates or shells, with the space-independent parameter G, which grows slowly with time. The elastic stresses are in the order of $\mu V_0(G-1)$, μ being the shear modulus and V_0 the initial volume: this estimate causes a significant increase of energy in the soft material if the stress relaxation and the shape remodeling are inhibited by the boundaries [3], but it may not coincide with true situations.

Recently Chen *et al.* [22,23] have proposed that the change of geometric shape is only induced by the volumetric growth $G(t)$ without the generation of elastic stresses. This strategy implies the definition of a mapping that connects the initial position of points to their current position at time t, and then $G(t)$ is determined by imposing a zero-stress condition. Their derivation is rather technical and their examples are based on initial circular geometry. Nevertheless, they derive a variety of stress-free mathematical geometries that mimic different biological patterns.

With the same objective but limiting ourselves to two-dimensional thin samples of arbitrary initial and final shapes, like fresh leaves, we propose a general formalism based on conformal mapping techniques. Indeed, regular planar close curves $\partial\Omega$ limiting a domain Ω can be related to the unit circle by a holomorphic function according to the Riemann theorem. This function also associates the points inside Ω to the Riemann disc, and it gives a way to construct the geometric deformation field during the growth process. Then the shape will evolve from Cartesian coordinates to a rectangular curvilinear system of coordinates. D'Arcy Thompson [24] made the hypothesis that these coordinates represent the velocity of shaping. Although conformal mapping is not explicitly mentioned in his original work, the pictures drawn in Ref. [24] concerning the growth and evolution between neighbor species strongly suggest such a hypothesis. The idea behind conformal mapping for growing leaves was revisited more recently [25] and also tested experimentally. For example, Alim *et al.* [26] predict the local displacement field of petunia and tobacco leaves through a conformal mapping, which is rather consistent with their experimental results.

The aim of this Letter is to prove that conformal mappings can recover the shape of leaves without generating elastic stress and can determine the growth laws,

independently of the nonlinear elasticity model. Herein, different shapes of common leaves are selected, with a special focus on the *Monstera deliciosa* family.

The formalism.—We consider a 2D formalism where the leaf thickness remains constant during the growth without deformation in the thickness direction. Growth is a very slow process so that the deformations adjust immediately to the growth. The initial leaf shape is represented by Ω_0 and the material points by $\mathbf{X}$, the current shape at time t becomes Ω_t with the current point coordinates $\mathbf{x}$. The geometric deformation gradient is the second order tensor defined by: $\mathbf{F} = \partial\mathbf{x}/\partial\mathbf{X}$, and $\mathbf{F} = \mathbf{F_e}\mathbf{G}$, where $\mathbf{G}$ is the growth and $\mathbf{F_e}$ the elastic tensor [1]. The right Cauchy tensor $\mathbf{C}$ only depends on $\mathbf{F_e}$ and is given by $\mathbf{C} = \mathbf{F_e^T}\mathbf{F_e}$ [2]. Using the curvilinear coordinates of the initial configuration with $Z = X + iY = F_1(\Xi) = F_1(\mu + i\eta)$, we choose z for the current configuration, such as $z = x + iy = F_2[k(\mu) + il(\eta)]$ where conformal mapping is preserved only if $k(\mu) = \mu$ and $l(\eta) = \eta$. $F_2(\mu + i\eta)$ is determined by the outer leaf shape $\partial\Omega_t$ which corresponds to $\mu = \mu_0 = k(\mu_0)$ at the time t of observation. Introducing $k(\mu)$ and $l(\eta)$ for z simply broadens the ensemble of mappings between the two domain boundaries F_1 and F_2.

Local growth rate of living tissues can be inhomogeneous (dependent on the coordinates μ and η) and anisotropic, which explains the tensorial mathematical representation of $\mathbf{G}$. To respect the leaf geometry, this tensor $\mathbf{G}$ must be diagonal: $\mathbf{G} = \mathrm{diag}[g(\mu,\eta)/p(\mu,\eta), p(\mu,\eta)g(\mu,\eta)]$, where $p(\mu,\eta)$ is the growth anisotropy coefficient, and $g(\mu,\eta)^2$ is the local volumetric growth at time t. For simplicity, we suppress the μ, η, and t dependence in p and g functions. Then the elastic tensor becomes

$$\mathbf{F_e} = \frac{1}{|\partial_\Xi F_1|}\begin{pmatrix} \frac{p}{g}\frac{\partial x}{\partial \mu} & \frac{1}{pg}\frac{\partial x}{\partial \eta} \\ \frac{p}{g}\frac{\partial y}{\partial \mu} & \frac{1}{pg}\frac{\partial y}{\partial \eta} \end{pmatrix}. \tag{1}$$

For incompressible living species, the third invariant $I_3 = \det \mathbf{F}_e = 1$, so imposing the local growth eigenvalue g:

$$G = g^2 = \left(\frac{\partial x}{\partial \mu}\frac{\partial y}{\partial \eta} - \frac{\partial x}{\partial \eta}\frac{\partial y}{\partial \mu}\right)/|\partial_\Xi F_1|^2. \tag{2}$$

A stress free configuration requires the cancellation of the first invariant I_1: $I_1 = \mathrm{Trace}\,\mathbf{C} - 2 = 0$ which, with the constraint $I_3 = 1$, leads to

$$\left(p\frac{\partial x}{\partial \mu} - \frac{1}{p}\frac{\partial y}{\partial \eta}\right)^2 + \left(p\frac{\partial y}{\partial \mu} + \frac{1}{p}\frac{\partial x}{\partial \eta}\right)^2 = 0. \tag{3}$$

If $p = 1$, the growth is isotropic, and Eq. (3) recovers the Cauchy relations implying that the current configuration z is an holomorphic function. If $p \neq 1$,the growth is anisotropic and $p^2 = l'(\eta)/k'(\mu)$. The derivation can be found in the Supplemental Material [27], Sec. I. In finite elasticity, the elastic strain depends on invariants (invariant under a rotation) traditionally called I_1, I_2, and I_3 [28,29], also eventually on pseudoinvariants I_4 and I_5 for transversely isotropic fibrous materials [30]. All these invariants are functions of the right Cauchy tensor $\mathbf{C}$ which is reduced to the unity tensor. So as long as Eq. (3) is satisfied, the growth process will generate no stress, even in the case of anisotropic growth.

As a conclusion, for 2D materials, it exists an infinite space of stress-free conformal maps associated to a growth tensor satisfying simultaneously Eqs. (2) and (3). Incompressibility is not mandatory since material compressibility is controlled by I_3 that is equal to unity in our case. In the following, we focus on fresh leaves which are extremely diverse in nature with quasiplanar shapes independently of the connection to the branch. The vein size depends on the species, most of them have a central prominent and rigid vein with a network of weaker lateral veins [31]. Having its own characteristics, each species requires an adaptation of our model to recover its shapes, which is perfectly doable with holomorphic functions. In particular, when very rigid veins appear, a partition following the big veins may be necessary and the modeling should be applied piece by piece. Hereafter, we focus on botanic traits, such as the tip, the margin, and the existence of internal holes. The knowledge of the initial and current shape contours specifies both functions F_1 and F_2 and also the growth density g. However, despite the mathematical proofs of existence of such functions, their precise determination remains a challenge in practice requiring to solve a rather difficult inverse problem [32–35], and the accuracy of numerical methods depends strongly on the complexity of the domain geometry. Therefore, our choice will consist of summing a restricted number of hyperbolic cosine functions $-i\Sigma_k b_k(t)S^k$ with $S = \cosh[a(\mu + i\eta)]$, the coefficient b_k being obtained by simple fitting of the contour. In practice, 3 modes k were sufficient to mimic a variety of leaf shapes during their growth. The schematic diagram is shown in Fig. 1.

Tips and margins of leaves.—Tips play a major role in physical growth processes in various fields such as dendritic growth [36], viscous fingering [37], fractures [38–40], and filamentary organisms [41]. Tips are often considered as being responsible for not only the growth dynamics but also the stability of the global shape. However, leaves [42] exhibit almost all kinds of shapes at the tip such as sharp pointed, convex, or concave, see Figs. 2(a)–2(c), the last case being much less common. Also, leaf margins are rather diverse, being either smooth such as lily leaves or undulated such as apple leaves. All these morphologies can be recovered with our formalism based on the expansion in powers of S, by fixing the central vein at $\mu = 0$ and the outer contour at $\mu = \mu_0$. The coefficient a characterizes the plant species and the parameters b_k at initial and final time t are adjusted to the observed contours, then generating both functions F_1 and F_2

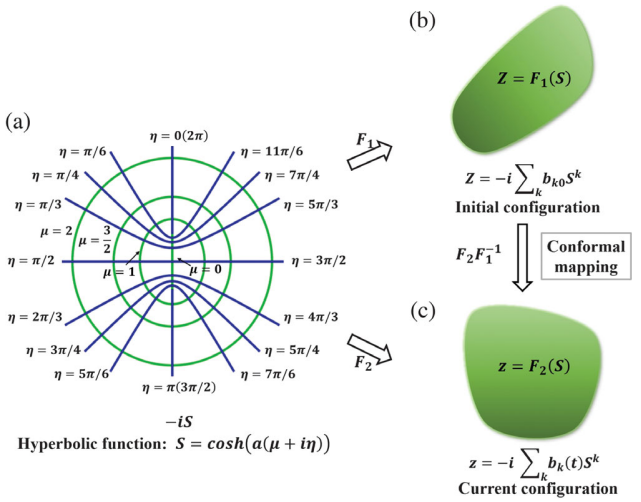

FIG. 1. Schematic diagram: (a) μ and η are the curvilinear coordinates, $\mu = \mu_0$ corresponds to a green curve and $\eta = \eta_0$ to a blue curve. (b) Parameters b_{k0} depend on the leaf contour at $t = 0$, (F_1). (c) Parameters $b_k(t)$ are determined by the contour at time t, (F_2).

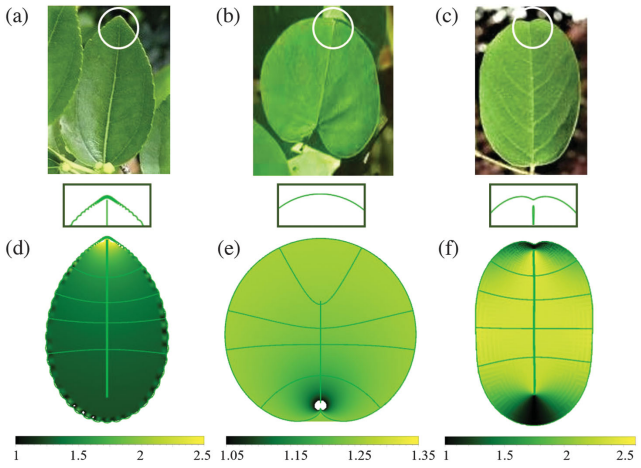

FIG. 2. Natural leaves: (a) *Jujube* leaf with sharp tip and oscillatory border. (b) *Redbud* leaf with rounded tip and smooth border. (c) *Robinia pseudoacacia* leaf with concave tip and smooth border. Mathematical images: (d)–(f) simulated by shape function (see Supplemental Material [27], Sec. SII). Level of green colors shows the local growth density in different regions, lighter color indicating more growth intensity. *Jujube* leaf [(a) and (d)] grows more at the tip while the top and bottom of *Robinia pseudoacacia* leaf [(c) and (f)] have a weak level of growth. *Redbud* leaf [(b) and (e)] shows a relatively uniform growth in the entire area, except near the petiole.

(see Supplemental Material [27], Sec. SII). Nevertheless, tips with a central dip or undulating margins require an additive correction $S_c = -ic(t)Se^{d(t)(\mu+i\eta-0.6)}$ to our expansion. The period and the amplitude of oscillations are easily controlled by $c(t)$ and $d(t)$, respectively, see Fig. 3, where we focus on the margins of the *Jujube* and the *White Sapote* leaves. For the *Robinia* shown in Fig. 2(f), the term S_c plays two roles, i.e., controlling tip and margin. Once the shape of the leaves is obtained with enough accuracy, the volumetric growth can be evaluated using Eq. (2). In particular, in Figs. 2(d)–2(f), color variation from dark green (weak growth amount) to light green or yellow indicates the heterogeneity of the growth intensity, less pronounced for the most rounded leaf [Fig. 2(e)].

Blade perforation.—Surprisingly, the initiation and evolution of holes in leaves also called fenestration is a rather rare event across the plant world, and it mostly happens in the family of *Monstera deliciosa*, commonly used as a decorative vine. The blade perforation remains difficult to interpret in terms of adaptive function to its natural environment, that consists in tropical forests, and different hypotheses have been considered such as water uptake or sun flecks [43]. There are some biological evidences that the blade perforation is generated by a regulated program of cell death [44] and in this case, we must take the hole distribution as a matter of fact occurring in rather big leaves (more than 10 cm): physics and mechanics cannot explain or justify their existence and distribution. Indeed, even in the same vine, the leaves have no symmetry: some present holes on both sides of the central veins, some only on one side, and the number of holes per leaf is highly variable. Most of the time, the perforation is not visible and happens when the leaf is still inside the sheath of an old one, see Supplemental Material [27]. The emergence of a hole in a mature leaf is a rare event but not impossible, in this case the central zone of the domain between two lateral veins becomes thinner and thinner in the middle, and ultimately one hole appears. The typical timescale for this event is about 1 month.

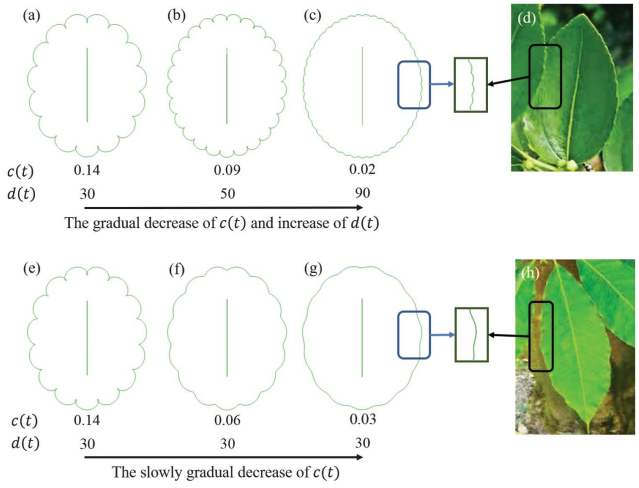

FIG. 3. Different leaf borders, shape function of all contours: $z = -ib_1S + S_c$, where $\mu_0 = 0.6$, $a = 2$ and $b_1 = 2$. (a)–(c): Boundary shapes changing with decreasing values of $\alpha(t)$ and $\beta(t)$. (d) *Jujube* leaves showing similar edges with (c). (e)–(g) Boundary shapes evolving with only decreasing values of $\alpha(t)$. (h) *White Sapote* leaves show similar edges as (g).

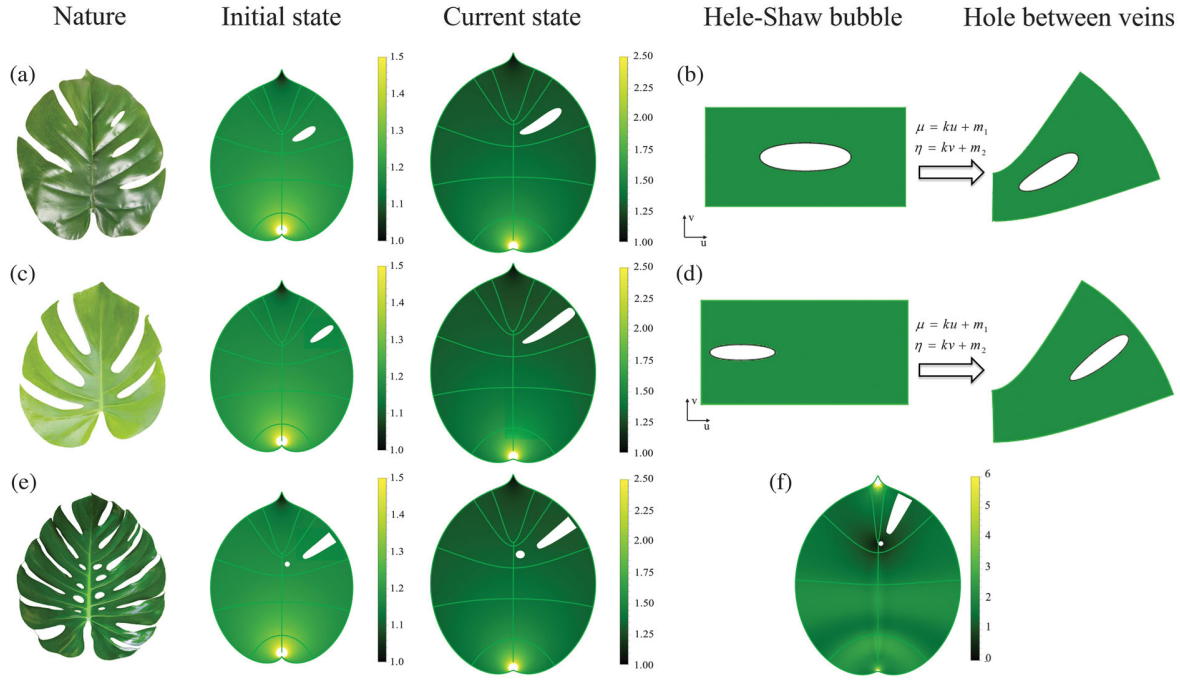

FIG. 4. (a) On left, natural *Monstera* deliciosa leaf with holes located either at the center (on top right) or connected to the border. On the same level on top, initial and current state of a mathematical leaf with one hole, located at the center in a chosen area. (b) A rectangle including a hole on left mapped into a specific curvilinear rectangle with boundaries defined by μ and η. The selected conformal mapping is a solution of the periodic Darcy flow with periodic and symmetric bubbles. Selection of constant k and c_2 are made in relation with (a). (c) Natural *Monstera* leaf with "fingerslike" shape holes. The initial and current state of a mathematical leaf with asymmetrical hole. (d) Conformal mapping generating an asymmetric bubble. The hole is closer to the outer boundary. (e) Natural Mexico *Monstera* leaf with holes and fingers and the initial and current state of mathematical leaf with two holes. (f) Anisotropic growth of the mathematical leaves with two holes, the functions $k(\mu)$ and $l(\eta)$ are detailed in [49], notice the changes of vein position between (e) and (f).

We have noticed the similarity of hole shapes with viscous fingers or bubbles in Hele-Shaw cells [45,46]. From the viewpoint of modeling, they have in common to be generated with conformal fields, of course due to totally different physical reasons. The studies more connected to our Letter concern series of steady bubbles of velocity U traveling periodically in an infinite linear Hele-Shaw cell. When surface tension is neglected, their shapes are defined by 2 (for symmetric and centered bubbles, [47]) or 7 parameters (for non symmetric bubbles, [48–50]), each of them allowing a time-dependent adjustment. The periodic flow field is Laplacian, satisfies the imposed boundary conditions on the two sides of a rectangle which corresponds to one period of the flow and is limited by the parallel horizontal walls of the experimental cell. Such a rectangle can be easily mapped to a domain enclosed by two lateral veins (defined by η), the central vein and the outer contour. At the bubble boundary, the pressure vanishes, which is also relevant to the elastic fenestration problem without stress. Calling ζ the Riemann unit disc coordinates, z_b the position of an arbitrary point in the flow, Burgess and Tanveer establish the following relation [47]:

$$\frac{dz_b}{d\zeta} = \frac{K(2/U + A(1+\zeta^2))}{\sqrt{(\zeta^2-\beta^2)(\zeta^2-\alpha^2)(1-\alpha^2\zeta^2)(1-\beta^2\zeta^2)}}, \quad (4)$$

where K and A are constants determined by the three parameters U, α, and β; they are responsible for the length and width of the hole through Eq. (4). The transformation process and the mapping functions are displayed in Fig. 4(b). The leaf shape functions are fully determined at two different times of their evolution and are shown in Fig. 4(a), in which the maximum growth rate G is predicted near the petiole while the tip corresponds to a minimal growth. These solutions have symmetric holes (for-aft, up-down) and centered in the middle, but in reality holes may appear closer to the edge where they broaden, see Fig. 4(c). In this case, they lose the for-aft symmetry and display finger shapes, the previous approach [47] ceases to be valid and more complex shape functions involving 8 parameters are required [48–50]; see Supplemental Material [27]. The mapping process between the bubble and the hole is the same for the symmetric or asymmetric case, see Figs. 4(b) and 4(d). In addition, a peculiar variety of *Monstera* exhibits a finger facing a small hole which reminds us of viscous fingering experiments in Hele-Shaw cells [51–54]. Figure 4(e) displays

an example of such leaves, comparing to our mathematical shapes at two different times. To sum up, our formalism applies to any kind of planar leaves. The shape complexity may require elaborated mapping functions that can be found either in the literature or in classical specialized books [55–57]. Numerical methods have also been established [33,34,58]. The amount of growth, isotropic or anisotropic, is obtained as displayed in Fig. 4 and in Supplemental Material [27].

Leaf vein.—Veins provide structure and support to leaves while also playing a vital role in transporting water and nutrients to the leaf blade. The region closer to the major vein may have access to more nutrients, which will be evenly transmitted into lateral veins with a nutrient content equivalent in each location [31]. Such unequal nutrient distribution is responsible for an anisotropic growth process represented in Ref. [59]. It further leads to a change of the leaf vein locations and consequently of the hole shape, as shown by the comparison of Figs. 4(f) and 4(e). Besides, in the anisotropic case, the growth rate G is more homogeneous across the whole leaf, except near the petiole and the tip.

Conclusion.—Among all mappings possible for the shape evolution of a 2D elastic sample, we demonstrate that conformal or quasiconformal mappings have the advantage to eliminate the elastic stresses independently of the elastic material properties. Contrary to other cases studied recently [3,5,6], leaves without exterior loading and growing in a quiet environment sustain this approach. In this Letter, we exploit the hypothesis of conformal mapping [24–26] on plant leaves, recovering the boundary and further obtaining the displacement field which establishes the growth kinematics. Our method extracts information not only on the cell proliferation which is often restricted to the nutrient penetration but also on the biological complexity, such as tissue remodeling [43]. This formalism allows us to evaluate the growth accumulation in case of isotropy or anisotropy. Veins can also be simulated and their relationship with nutrient contents can be established. Understanding the stress-free morphological evolution induced by growth is not limited to the morphogenesis of leaves or other biological tissues, but can also shed light on the design of new biomimetic soft devices.

The authors acknowledge the support of ANR (Agence Nationale de la Recherche) under the contract MecaTiss (ANR-17-CE30-0007) and the contract EpiMorph (ANR-2018-CE13-0008). A. D. acknowledges the support of the CSC (China Scholarship Council), file No. 201906250173.

*Corresponding author.
benamar@phys.ens.fr

[1] E. K. Rodriguez, A. Hoger, and A. D. McCulloch, Stress-dependent finite growth in soft elastic tissues, J. Biomech. **27**, 455 (1994).
[2] A. Goriely, *The Mathematics and Mechanics of Biological Growth* (Springer, New York, 2017), Vol. 45.
[3] D. Ambrosi, M. Ben Amar, C. J. Cyron, A. DeSimone, A. Goriely, J. D. Humphrey, and E. Kuhl, Growth and remodelling of living tissues: Perspectives, challenges and opportunities, J. R. Soc. Interface **16**, 20190233 (2019).
[4] M. Ben Amar, M. M. Müller, and M. Trejo, Petal shapes of sympetalous flowers: the interplay between growth, geometry and elasticity, New J. Phys. **14**, 085014 (2012).
[5] F. Xu, C. Fu, and Y. Yang, Water Affects Morphogenesis of Growing Aquatic Plant Leaves, Phys. Rev. Lett. **124**, 038003 (2020).
[6] D. E. Moulton, H. Oliveri, and A. Goriely, Multiscale integration of environmental stimuli in plant tropism produces complex behaviors, Proc. Natl. Acad. Sci. U.S.A. **117**, 32226 (2020).
[7] T. Tallinen, J. Y. Chung, F. Rousseau, N. Girard, J. Lefèvre, and L. Mahadevan, On the growth and form of cortical convolutions, Nat. Phys. **12**, 588 (2016).
[8] M. Kücken and A. C. Newell, Fingerprint formation, J. Theor. Biol. **235**, 71 (2005).
[9] P. Ciarletta and M. Ben Amar, Papillary networks in the dermal–epidermal junction of skin: A biomechanical model, Mech. Res. Commun. **42**, 68 (2012).
[10] B. Li, Y.-P. Cao, X.-Q. Feng, and H. Gao, Surface wrinkling of mucosa induced by volumetric growth: Theory, simulation and experiment, J. Mech. Phys. Solids **59**, 758 (2011).
[11] A. J. Coulombre and J. L. Coulombre, Intestinal development: I. Morphogenesis of the villi and musculature, Journal of Embryology and Experimental Morphology **6**, 403 (1958).
[12] M. Ben Amar and F. Jia, Anisotropic growth shapes intestinal tissues during embryogenesis, Proc. Natl. Acad. Sci. U.S.A. **110**, 10525 (2013).
[13] A. E. Shyer, T. Tallinen, N. L. Nerurkar, Z. Wei, E. S. Gil, D. L. Kaplan, C. J. Tabin, and L. Mahadevan, Villification: How the gut gets its villi, Science **342**, 212 (2013).
[14] J. Dervaux and M. Ben Amar, Morphogenesis of Growing Soft Tissues, Phys. Rev. Lett. **101**, 068101 (2008).
[15] B. Li, Y.-P. Cao, X.-Q. Feng, and H. Gao, Mechanics of morphological instabilities and surface wrinkling in soft materials: A review, Soft Matter **8**, 5728 (2012).
[16] J. Yin, J. L. Yagüe, D. Eggenspieler, K. K. Gleason, and M. C. Boyce, Deterministic order in surface micro-topologies through sequential wrinkling, Adv. Mater. **24**, 5441 (2012).
[17] M. R. Nelson, J. R. King, and O. E. Jensen, Buckling of a growing tissue and the emergence of two-dimensional patterns, Math. Biosci. **246**, 229 (2013).
[18] A. M. Chin, D. R. Hill, M. Aurora, and J. R. Spence, Morphogenesis and maturation of the embryonic and postnatal intestine, in *Seminars in Cell & Developmental Biology* (Elsevier, New York, 2017), Vol. 66, pp. 81–93.
[19] P. Manneville, Rayleigh-bénard convection: Thirty years of experimental, theoretical, and modeling work, in *Dynamics of Spatio-Temporal Cellular Structures* (Springer, New York, 2006), pp. 41–65.
[20] F. Charru, *Hydrodynamic Instabilities* (Cambridge University Press, Cambridge, England, 2011), Vol. 37.

[21] J. Ackermann, P.-Q. Qu, L. LeGoff, and M. Ben Amar, Modeling the mechanics of growing epithelia with a bilayer plate theory, Eur. Phys. J. Plus **137**, 8 (2022).

[22] X. Chen and H.-H. Dai, Stress-free configurations induced by a family of locally incompatible growth functions, J. Mech. Phys. Solids **137**, 103834 (2020).

[23] X. Chen, Y. Shen, Z. Li, D. Gu, and J. Wang, Generating complex fold patterns through stress-free deformation induced by growth, J. Mech. Phys. Solids **159**, 104702 (2022).

[24] D. W. Thompson, *On Growth and Form*, (Cambridge University Press, Cambridge, England, 1917).

[25] S. Nechaev and R. Voituriez, On the plant leaf's boundary, jupe à godets' and conformal embeddings, J. Phys. A **34**, 11069 (2001).

[26] K. Alim, S. Armon, B. I. Shraiman, and A. Boudaoud, Leaf growth is conformal, Phys. Biol. **13**, 05LT01 (2016).

[27] See Supplemental Material at http://link.aps.org/supplemental/10.1103/PhysRevLett.129.218101 for the detailed presentation of the theory and proofs concerning nonlinear elasticity. Application of the theory to the selected leaves of the Letter with data.

[28] R. W. Ogden, *Non-Linear Elastic Deformations* (Dover Publications, INC., Mineola, New York, 1997).

[29] A. G. Holzapfel, *Nonlinear Solid Mechanics II* (John Wiley & Sons, Inc., Chichester, West Sussex, 2000).

[30] M. Destrade, B. Mac Donald, J. Murphy, and G. Saccomandi, At least three invariants are necessary to model the mechanical response of incompressible, transversely isotropic materials, Comput. Mech. **52**, 959 (2013).

[31] E. Katifori, The transport network of a leaf, C. R. Phys. **19**, 244 (2018).

[32] T. K. DeLillo and A. R. Elcrat, Numerical conformal mapping methods for exterior regions with corners, J. Comput. Phys. **108**, 199 (1993).

[33] T. K. Delillo, The accuracy of numerical conformal mapping methods: a survey of examples and results, SIAM J. Numer. Anal. **31**, 788 (1994).

[34] T. K. DeLillo, A. R. Elcrat, and J. Pfaltzgraff, Schwarz-Christoffel mapping of multiply connected domains, J. Anal. Math. **94**, 17 (2004).

[35] T. K. DeLillo and S. Sahraei, Computation of plane potential flow past multi-element airfoils using conformal mapping, revisited, J. Comput. Appl. Math. **362**, 246 (2019).

[36] G. Caginalp and E. Socolovsky, Phase field computations of single-needle crystals, crystal growth, and motion by mean curvature, SIAM J. Sci. Comput. **15**, 106 (1994).

[37] E. Lajeunesse and Y. Couder, On the tip-splitting instability of viscous fingers, J. Fluid Mech. **419**, 125 (2000).

[38] J. Rice and E. P. Sorensen, Continuing crack-tip deformation and fracture for plane-strain crack growth in elastic-plastic solids, J. Mech. Phys. Solids **26**, 163 (1978).

[39] Y. Morishita, K. Tsunoda, and K. Urayama, Crack-tip shape in the crack-growth rate transition of filled elastomers, Polymer **108**, 230 (2017).

[40] D. I. Garagash, E. Detournay, and J. I. Adachi, Multiscale tip asymptotics in hydraulic fracture with leak-off, J. Fluid Mech. **669**, 260 (2011).

[41] A. Goriely and M. Tabor, Self-Similar Tip Growth in Filamentary Organisms, Phys. Rev. Lett. **90**, 108101 (2003).

[42] M. Ben Amar and J. Dervaux, Tip growth in morpho-elasticity, C. R. Méc. **348**, 613 (2020).

[43] J. Dkhar and A. Pareek, What determines a leaf's shape?, EvoDevo **5**, 1 (2014).

[44] A. H. Gunawardena, K. Sault, P. Donnelly, J. S. Greenwood, and N. G. Dengler, Programmed cell death and leaf morphogenesis in monstera obliqua (araceae), Planta **221**, 607 (2005).

[45] P. G. Saffman and G. I. Taylor, The penetration of a fluid into a porous medium or Hele-Shaw cell containing a more viscous liquid, Proc. R. Soc. A **245**, 312 (1958).

[46] G. Taylor and P. Saffman, A note on the motion of bubbles in a Hele-Shaw cell and porous medium, Q. J. Mech. Appl. Math. **12**, 265 (1959).

[47] D. Burgess and S. Tanveer, Infinite stream of Hele-Shaw bubbles, Phys. Fluids A **3**, 367 (1991).

[48] D. Crowdy, Multiple steady bubbles in a Hele-Shaw cell, Proc. R. Soc. A **465**, 421 (2009).

[49] A. M. Silva and G. L. Vasconcelos, Doubly periodic array of bubbles in a Hele-Shaw cell, Proc. R. Soc. A **467**, 346 (2011).

[50] G. L. Vasconcelos, Multiple bubbles and fingers in a Hele-Shaw channel: Complete set of steady solutions, J. Fluid Mech. **780**, 299 (2015).

[51] Y. Couder, N. Gerard, and M. Rabaud, Narrow fingers in the Saffman-Taylor instability, Phys. Rev. A **34**, 5175 (1986).

[52] M. Rabaud, Y. Couder, and N. Gerard, Dynamics and stability of anomalous Saffman-Taylor fingers, Phys. Rev. A **37**, 935 (1988).

[53] G. L. Vasconcelos, Exact solutions for steady bubbles in a Hele-Shaw cell with rectangular geometry, J. Fluid Mech. **444**, 175 (2001).

[54] D. Crowdy, An assembly of steadily translating bubbles in a Hele-Shaw channel, Nonlinearity **22**, 51 (2009).

[55] E. Durand, *Électrostatique: Problèmes généraux. Conducteurs* (Masson, Paris, 1964), Vol. 2.

[56] E. Durand, *Electrostatique. 2. Problèmes généraux conducteurs* (Masson, Paris, 1966).

[57] V. I. Ivanov and M. K. Trubetskov, *Handbook of Conformal Mapping with Computer-Aided Visualization* (CRC Press, Boca Raton, 1994).

[58] T. K. DeLillo, J. Mears, and A. Silva-Trujillo, Potential flow in a multiply connected circle domain using series methods, J. Comput. Appl. Math. **391**, 113445 (2021).

[59] $k(\mu) = \mu(1 + 0.1e^{-100\mu^2})$ and $l(\eta) = \eta[1 + 0.1(e^{-12(-7\pi/8+\eta)^2} + e^{-12(-3\pi/4+\eta)^2} + e^{-12(-5\pi/8+\eta)^2} + e^{-12(-\pi/2+\eta)^2} + e^{-12(-5\pi/16+\eta)^2})]$.

Supplemental Material: Minimizing the elastic energy of growing leaves by conformal mapping

Anna Dai[1] and Martine Ben Amar[1]

[1]*Laboratoire de Physique, Ecole Normale Supérieure, CNRS, Sorbonne Université, 24 rue Lhomond, 75005 Paris*

(Dated: October 6, 2022)

I. STRESS-FREE GROWTH

We assume that the initial shape of the leaf is given by:

$$Z = F_1(\Xi) = F_1(\mu + \mathrm{i}\eta) \quad \text{so} \quad \Xi = \mu + i\eta \quad \text{and} \quad G_1 = F_1^{-1} \tag{1}$$

where $i^2 = -1$, F_1 represents the mapping between cartesian coordinates and curvilinear coordinates of the interior of the leaf, μ and η are conformal coordinates and $\mu = \mu_0$ gives the initial outer shape. Here, we restrict to leaf shapes simply described by a enough regular contour. We will explain later domains with holes which must be treated with appropriate methods [1–3]. Knowing the outer boundary, it is always possible to define the function F_1 from the boundary, which is not always an easy task and this mapping is unique, for regular contour. To take the inverse of an holomorphic function F_1 is always doable formally and gives G_1 also an holomorphic function. As a consequence, we get the following Cauchy relations:

$$\frac{\partial \mu}{\partial X} = \frac{\partial \eta}{\partial Y} \quad \text{and} \quad \frac{\partial \mu}{\partial Y} = -\frac{\partial \eta}{\partial X} \tag{2}$$

In morpho-elasticity, growth is represented by a tensor $\mathbf{G}$ which is inhomogeneous most of the time (that means space dependent) and also anisotropic. We assume that the growth respects the leaf geometry so the tensor $\mathbf{G}$ is diagonal and reads:

$$\mathbf{G} = \begin{bmatrix} \frac{1}{p(\mu,\eta)} g(\mu,\eta) & 0 \\ 0 & p(\mu,\eta)\, g(\mu,\eta) \end{bmatrix} \tag{3}$$

where $p(\mu,\eta)$ is the growth anisotropy coefficient and $\mathrm{Det}(\mathbf{G}) = g(\mu,\eta)^2$ is the volumetric growth at the time of observation. When the leaf grows, we assume that the displacement of each point is given by the following mapping F_2 such that:

$$z = F_2(k(\mu) + il(\eta)) \tag{4}$$

where z represents the new coordinates (x, y). This mapping is not conformal but it gives for x and y the relationship with the initial shape configuration such as:

$$\begin{cases} x = \frac{1}{2}\left[F_2(k(\mu) + il(\eta)) + \overline{F_2}(k(\mu) - il(\eta))\right] \\ y = \frac{1}{2i}\left[F_2(k(\mu) + il(\eta)) - \overline{F_2}(k(\mu) - il(\eta))\right] \end{cases} \tag{5}$$

According to the main hypothesis of the morpho-elasticity theory, the geometric gradient of deformation $\mathbf{F}$ and the elastic gradient of deformation tensor $\mathbf{F_e}$ are related by : $\mathbf{F} = \mathbf{F_e}\mathbf{G}$ [4]. Written in these conformal coordinates, these tensors become:

$$\mathbf{F} = \frac{1}{|\partial_\Xi F_1|}\begin{bmatrix} \frac{\partial x}{\partial \mu} & \frac{\partial x}{\partial \eta} \\ \frac{\partial y}{\partial \mu} & \frac{\partial y}{\partial \eta} \end{bmatrix} \quad \text{and} \quad \mathbf{F_e} = \frac{1}{|\partial_\Xi F_1|}\begin{bmatrix} \frac{p}{g}\frac{\partial x}{\partial \mu} & \frac{1}{pg}\frac{\partial x}{\partial \eta} \\ \frac{p}{g}\frac{\partial y}{\partial \mu} & \frac{1}{pg}\frac{\partial y}{\partial \eta} \end{bmatrix} \tag{6}$$

The first physical constraint concerns the incompressibility of the sample which imposes:

$$\mathrm{Det}(\mathbf{F_e}) = 1 \Longleftrightarrow \frac{\partial x}{\partial \mu}\frac{\partial y}{\partial \eta} - \frac{\partial x}{\partial \eta}\frac{\partial y}{\partial \mu} = g^2 |\partial_\Xi F_1|^2 \tag{7}$$

In addition, a stress-free configuration imposes $I_1 = Tr\left(\mathbf{F_e}^{\mathbf{T}}\mathbf{F_e}\right) - 2 = 0$ and we derive:

$$p^2\left(\frac{\partial x}{\partial \mu}\right)^2 + p^2\left(\frac{\partial y}{\partial \mu}\right)^2 + \frac{1}{p^2}\left(\frac{\partial x}{\partial \eta}\right)^2 + \frac{1}{p^2}\left(\frac{\partial y}{\partial \eta}\right)^2 = 2g^2|\partial_\Xi F_1|^2 = 2\left(\frac{\partial x}{\partial \mu}\frac{\partial y}{\partial \eta} - \frac{\partial x}{\partial \eta}\frac{\partial y}{\partial \mu}\right) \tag{8}$$

A simple reorganization of Eq.(8) leads to:

$$\left(p\frac{\partial x}{\partial \mu} - \frac{1}{p}\frac{\partial y}{\partial \eta}\right)^2 + \left(p\frac{\partial y}{\partial \mu} + \frac{1}{p}\frac{\partial x}{\partial \eta}\right)^2 = 0 \tag{9}$$

so we get:

$$p\frac{\partial x}{\partial \mu}-\frac{1}{p}\frac{\partial y}{\partial \eta}=0 \quad \text{and} \quad p\frac{\partial y}{\partial \mu}+\frac{1}{p}\frac{\partial x}{\partial \eta}=0 \tag{10}$$

If $p=1$ (isotropic growth), Eq.(10) recovers the Cauchy relations and implies that F_2 is an holomorphic function. If $p\neq 1$, an anisotropic growth process may also generate a stress free configuration. The coefficient of anisotropy for a description ruled by F_2 (see Eq.(5)) is obtained with:

$$\frac{\partial x}{\partial \mu}=k'(\mu)\frac{{F_2}'+\overline{F_2}'}{2}, \quad \frac{\partial x}{\partial \eta}=l'(\eta)\,i\frac{{F_2}'-\overline{F_2}'}{2}, \quad \frac{\partial y}{\partial \mu}=k'(\mu)\frac{{F_2}'-\overline{F_2}'}{2i}, \quad \frac{\partial y}{\partial \eta}=l'(\eta)\,i\frac{{F_2}'+\overline{F_2}'}{2} \tag{11}$$

For simplicity, we do not detail the variable of each function and the symbol prime ($'$) means the first derivative with respect to the natural variable as defined in Eq.(5). So introducing the values of the partial derivatives given by Eq.(11) into Eq.(10) gives:

$$p^2=\frac{l'(\eta)}{k'(\mu)} \tag{12}$$

II. COMPLEX REPRESENTATIONS OF LEAVES

In the main text, four different types of leaves are simulated, showing different properties. Knowing their outer border, their respective shape functions are derived from the hyperbolic function $S=\cosh(a(\mu+\mathrm{i}\eta))$, eventually with a correction S_c. We consider 2 different times. The first one called the initial time or time t=0 corresponds to the situation where the leaf is yet planar and its shape characteristics rather well defined, the second time concerns the situation where obviously the surface of the leaf has increased and perhaps some new features concerning eventually the tip or the margin appear. Due to the growth, the coefficients between the two configurations will evolve in time and will reveal the observed shapes of mature leaves at time t. In the cases considered in the main manuscript, we have firstly found the contour function of the Jujube leaf, which is similar to an oval, with sharp tips and jagged edges, and it reads:

$$z=-i\left(b_1(t)S+b_2(t)S^2+b_3(t)S^3+c(t)\,e^{d(t)(\mu+i\eta-0.6)}S\right) \tag{13}$$

Redbud leaf resembles an inverted heart shape, with rounded tip and smooth border:

$$z=-i\left(b_1(t)S+b_2(t)S^2\right) \tag{14}$$

Robinia pseudoacacia leaf has a concave tip and smooth border suggesting:

$$z=-i\left(b_1(t)S+b_2(t)\,S^2+c(t)\,e^{d(t)(\mu+i\eta-0.6)}S\right) \tag{15}$$

Monstera leaf is the same as Redbud leaf, their petiole is concave, but the overall leaf is slightly longer, narrower and the tip is more pronouced:

$$z=-i\left(b_1(t)S-b_2(t)\,S^2+0.1(\mathrm{Log}\,(S-S_0))^{1.09}\right) \tag{16}$$

where $S_0=\cosh(a(\mu_v+I\eta_v))$, (μ_v,η_v) being located at the vertex coordinate of the function $z=-i\left(b_1(t)S-b_2(t)\,S^2\right)$. a is a constant, and $b_k(t)$, $c(t)$ and $d(t)$ are functions of t. Except for the Monstera, the data are obtained by simple guess in Table SI. For the Monstera leaf, the data between two time intervals of 14 days are derived by fit of the outer contour at time $t=0$, t_1 (leave 1) and t_2 (leave 2). In the following, we restrict first on the Redbud case, then on the Monstera case.

III. DETERMINATION OF THE GROWTH CHARACTERISTICS

In this section, we detail the method to reach the growth parameters as $g(\mu,\eta)$ and $p(\mu,\eta)$ for the Redbud leaf. From Eq.(14), we choose the initial representation as :

$$\begin{aligned} X&=-b_{10}\sin(a\eta)\sinh(a\mu)-2b_{20}\cos(a\eta)\cosh(a\mu)\sin(a\eta)\sinh(a\mu)\\ Y&=b_{10}\cos(a\eta)\cosh(a\mu)+b_{20}\{\cos(a\eta)\cosh(a\mu)\}^2-b_{20}\{\sin(a\eta)\sinh(a\mu)\}^2 \end{aligned} \tag{17}$$

Leaf Name	μ_0	a	b_{10}	$b_1(t)$	b_{20}	$b_2(t)$	b_{30}	$b_3(t)$	c_0	$c(t)$	d_0	$d(t)$
Jujube Leaf	0.51	1	0.8	1	0.55	0.6	0.16	0.16	2.42	6.58	60	70
Redbud Leaf	1	1.1	-0.62	-0.7	-0.5	-0.22	-	-	-	-	-	-
Robinia pseudoacacia leaf	0.7	1	1.5	1.75	0.28	0.3	-	-	0.11	0.09	3	3
Monstera leaf 1	0.8	1.2	1.7	1.8	0.58	0.6	-	-	-	-	-	-
Monstera leaf 2	0.8	1.2	1.8	1.9	0.6	0.63	-	-	-	-	-	-

TABLE.S I. Parameters of leaf functions at initial time and at time t. For Monstera, two times of observation are listed.independently of $t = 0$.

and the current representation as:

$$\begin{aligned} x &= -b_1(t)\sin(a\eta)\sinh(a\mu) - 2b_2(t)\cos(a\eta)\cosh(a\mu)\sin(a\eta)\sinh(a\mu) \\ y &= b_1(t)\cos(a\eta)\cosh(a\mu) + b_2(t)\{\cos(a\eta)\cosh(a\mu)\}^2 - b_2(t)\{\sin(a\eta)\sinh(a\mu)\}^2 \end{aligned} \tag{18}$$

The volumetric growth density parameter $g(\mu,\eta)^2$, for isotropic growth has been established in Eq.(2) of the main text, and is displayed in Fig.(2) and Fig.(4) of the main text, with green colors of variable intensity according to the values of g^2. Once we fix the initial configuration at time $t = 0$ with the same representation (which is not mandatory), we get the following volumetric growth rate:

$$g^2 = \frac{b_1(t)^2 + 2b_2(t)^2\cos(2a\eta) + 4b_1(t)b_2(t)\cos(a\eta)\cosh(a\mu) + 2b_2(t)^2\cosh(2a\mu)}{{b_{10}}^2 + 2b_{20}^2\cos(2a\eta) + 4b_{10}b_{20}\cos\cos(a\eta)\cosh(a\mu) + 2{b_{20}}^2\cosh(2a\mu)} \tag{19}$$

The same method can be applied for finding the growth rate which determines the stress-free pattern for the other leaves. All the parameters of leaf functions are shown in Table SI. Fig.(2) of the main text shows three kinds of leaves: Jujube, Redbud and Robinia pseudoacacia leaf. In Fig.(4) (a)(c)(e) devoted to Monstera, the initial state leaf uses the parameters of the Monstera leaf 1 to calculate the growth. Current state leaf and Fig.(4) (f) use the parameters of the Monstera leaf 2.

To illustrate the method for anisotropic growth, we define $k(\mu) = \mu$ and $l(\eta) = (2\pi)^{-2}e^{\frac{(\eta^2-1)}{(2\pi)^2}} + \eta - 0.1$ according to Eq.(3) of the main manuscript, defining the current configuration:

$$z = ib_1(t)\cosh\left[a\left(\mu + il\left(\eta\right)\right)\right] + ib_2(t)\cosh^2\left[a\left(\mu + il\left(\eta\right)\right)\right] \tag{20}$$

According to Eq.(12), the anisotropic coefficient p is given by $p^2 = 1 + (8\pi^4)^{-1}\eta e^{\frac{\eta^2}{(2\pi)^2}-1}$, and the volumetric growth rate becomes:

$$g^2 = \frac{l'(\eta)\left\{\cos\left(2al\left(\eta\right)\right) - \cosh\left(2a\mu\right)\right\}\left\{b_1(t)^2 + 2b_2(t)^2\left(\cos\left(2al\left(\eta\right)\right) + \cosh\left(2a\mu\right)\right) + 4b_1(t)b_2(t)\cos\left(al\left(\eta\right)\right)\cosh\left(a\mu\right)\right\}}{\{\cos(2a\eta) - \cosh(2a\mu)\}\left\{b_{10}^2 + 2b_{20}^2\cos(2a\eta) + 4b_{10}\mathrm{b}_{20}\cos(a\eta)\cosh(a\mu) + 2b_{20}^2\cosh(2a\mu)\right\}} \tag{21}$$

where the parameters are the same as the ones for the isotropic growth. The mathematical leaves are shown in Fig.(S1) and we can observe that the position of the leaf veins has changed with the growth anisotropy. So growth anisotropy gives a way to modify the position of the lateral veins if their positions change between the two times of observation.

IV. HELE-SHAW BUBBLES VERSUS HOLES IN MONSTERA

The Monstera leaf fenestration requires specific tools for its representation. Our strategy consists in isolating the area where the hole is located maintaining the original whole shape given by Eq.(16). We look for a conformal mapping which involves the domain between the central axis, two consecutive veins and the outer frontier of the leaf defined by $\mu_0 = 0.8$. The strategy is obvious if a complex mapping is known for a complex potential function defined in a stripe with one or two holes. The potential flow representing a bubble or a finger travelling in a linear Hele-Shaw cell can be a good candidate. Indeed, the hydrodynamic flow being governed by the Darcy law with incompressibility leads to a Laplacian pressure field, the shape bubble appearing as a line of zero-pressure. The classical work of a unique finger [5] or bubble [6] in the linear infinite channel geometry has been solved by Saffman and Taylor a long time ago, and the more recent extension to a periodic set of bubbles has been discovered later, giving a way to solve a major difficulty: the domain of interest in our case has a finite length and we must link this domain to a unique period of the stationary flow.

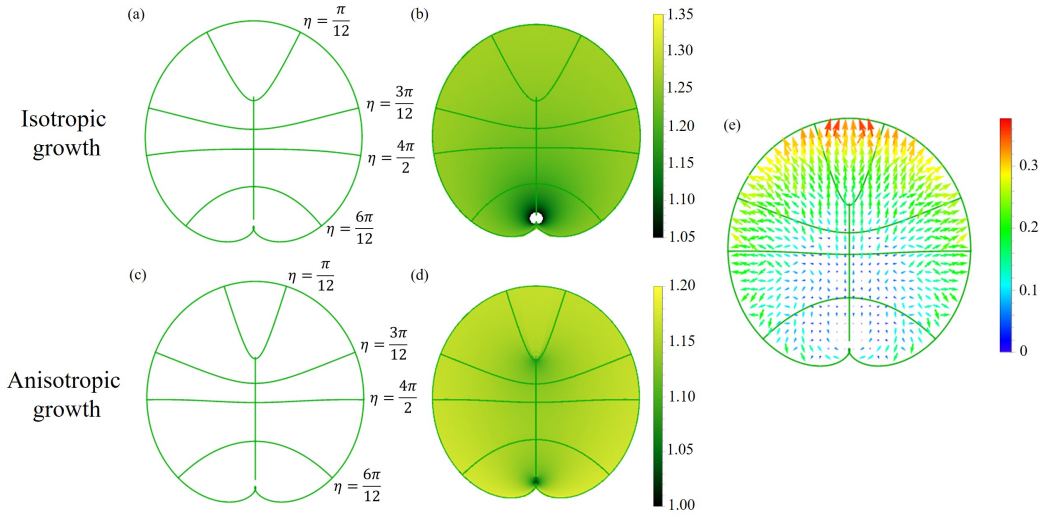

Fig.S 1. (a) Current outer contour corresponding to $\mu_0 = 1$ of the isotropic growth. Veins of constant value $\eta = \eta_0$. (b)Volumetric isotropic growth coefficient in green colors. Intensity varies between 1.05 and 1.35. (c) Current outer contour corresponding to $\mu_0 = 1$ of the anisotropic growth. Veins of constant value $\eta = \eta_0$. For anisotropic growth $p^2 = 1 + (8\pi^4)^{-1}\eta e^{\frac{\eta^2}{(2\pi)^2}-1}$. Comparing to the (a), the position of veins changed. (d) Volumetric anisotropic growth coefficient in green colors. Intensity varies between 1 and 1.2. (e) Displacement of the velocity field visualized with arrows.

A. Symmetric hole

We first focus on the symmetric hole/bubble located in the middle of the domain. D. Burgess and S. Tanveer [7] have derived a three-parameter family of exact solutions defined in the unit half-disc, see Fig.(S2)(a)-(b). We select this conformal mapping $z_b(\zeta)$ determined by:

$$\frac{dz}{d\zeta} = KF(\zeta)\left(2/U + A + A\zeta^2\right) \quad \text{with} \quad F(\zeta) = \frac{1}{\sqrt{(\zeta^2-\beta^2)(\zeta^2-\alpha^2)(1-\alpha^2\zeta^2)(1-\beta^2\zeta^2)}} \tag{22}$$

where $z_b(\zeta) = u + iv$, and (u, v) are the coordinates in the physical plane of the Hele-shaw cell moving with a bubble with the velocity U. α, β and U are the 3 degrees of freedom, while the constants K and A are determined via α, β and U:

$$f_n(\alpha,\beta) = \int_\alpha^\beta t^n F(t)dt; n = 0, 2, \quad K = \frac{U-1}{f_0 - f_2}, \quad \text{and} \quad A = \frac{1}{f_0+f_2}\left(\frac{f_0-f_2}{U-1} - \frac{2f_0}{U}\right) \tag{23}$$

These parameters are within the following ranges: $1 < U < \infty$, $0 < \alpha < \beta < 1$, $K > 0$ and $-1/U < A < \infty$.

As shown in Fig.(S2)(a) and (b) similar to the Fig.(2) in the Ref.[7], six points from A to E represent the one-to-one correspondence points before and after the mapping. We divide them into four parts, line segment CD, EF, DE and half bubble AB, and then we use Eq.[22] for piecewise integration to obtain the Fig.(S2)(b), which shows a half-bubble in the rectangle. It is worth noting that in the integration we need to specify the length L and width of the rectangle. The width is constant in this mapping and equal to 1, L is determined by:

$$g_n(\alpha,\beta) = \int_{-\alpha}^{\alpha} t^2 F(t)dt; n = 0, 2 \quad \text{and} \quad K[(2/U + A)g_0 + Ag_2] = L \tag{24}$$

By means of the symmetry in Fig.(S2)(b), a complete bubble is obtained, and an additive conformal mapping is required for the transformation of the bubble into a hole located between two lateral curved veins. By letting $\alpha = 0.79$, $\beta = 0.808$, $U = 3$ for Fig.(S2)(c) and $\alpha = 0.9$, $\beta = 0.935$, $U = 3.5$ for Fig.(S2)(d), the original hole shape at two different times (green figures) are obtained. Then the transformation can be achieved by a simple linear relationship, $\mu = ku + m_1$ and $\eta = kv + m_2$, where constants $k = \pi/16$, $m_1 = 0$ and $m_2 = \pi/16$, two cases are obtained with holes in different areas, and their details are shown in Fig.(S2)(c)-(d).

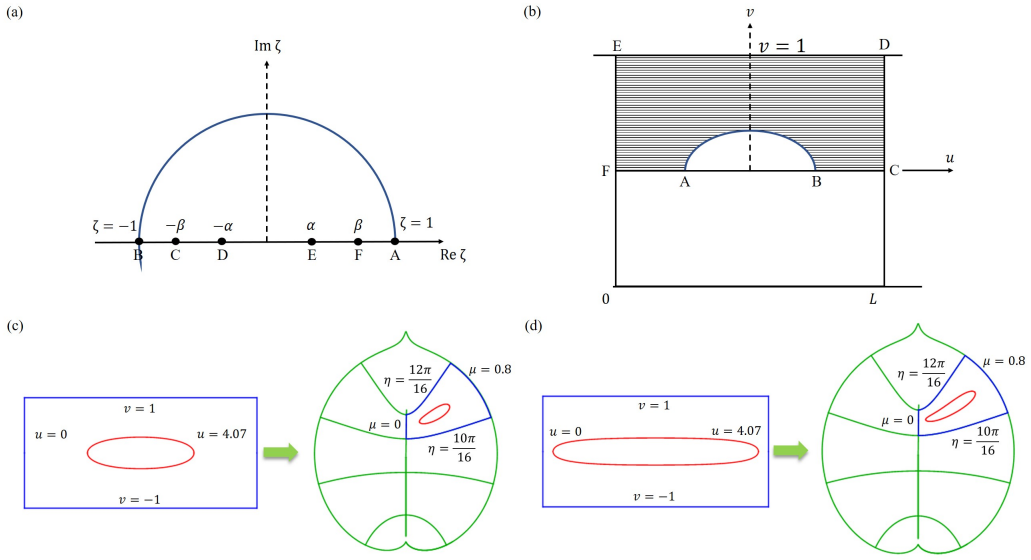

Fig.S 2. In (a) the flow region in the ζ plane, in (b) the physical z_b plane from [7] . In (c) and (d) original and transformed holes at time $t = 0$ and time t in a growing leaf.

B. Asymmetrical hole/bubble

Noticing that, in the Monstera deliciosa, the shape of holes looks like more a viscous finger issued from the outer boundary, we consider now a process where the left-right symmetry is not preserved. Such solutions and extension of the previous case [7] have been explicited in different works by G. Vasconcelos and his collaborators [8, 9] and D. Crowdy [10, 11], and following the formulation developed in Ref. [8], see also Fig.(S3)(a)-(b), the function $z_b(\zeta)$ reads:

$$z_b\left(\zeta\right) = -\frac{1}{U}\left[W(\zeta) - \widetilde{W}(\zeta)\right] \tag{25}$$

where $W(\zeta)$ and $\widetilde{W}(\zeta)$ are defined by :

$$W(\zeta) = \mathrm{K}\int_{\zeta_0}^{\zeta} \frac{P\left(q^2\frac{\zeta}{\beta_1},q\right)P\left(q^2\frac{\zeta}{\beta_3},q\right)}{\sqrt{\prod_{k=1}^{4}P\left(\frac{\zeta}{\alpha_k},q\right)}}d\zeta \quad \text{and} \quad \widetilde{W}(\zeta) = \widetilde{\mathrm{K}}\int_{\alpha_4}^{\zeta} \frac{P\left(q^2\frac{\zeta}{\beta_2},q\right)P\left(q^2\frac{\zeta}{\beta_4},q\right)}{\sqrt{\prod_{k=1}^{4}P\left(\frac{\zeta}{\alpha_k},q\right)}}d\zeta \tag{26}$$

the constants K and $\widetilde{\mathrm{K}}$ being given by:

$$\mathrm{K}^{-1} = \frac{1}{w\left(U-V\right)}\int_{\theta_3}^{\theta_4} \frac{P\left(q^2\frac{e^{i\theta}}{\beta_1},q\right)P\left(q^2\frac{e^{i\theta}}{\beta_3},q\right)}{\sqrt{\prod_{k=1}^{4}P\left(e^{i(\theta-\theta_k)},q\right)}}e^{i\theta}d\theta \quad \text{and} \quad \widetilde{\mathrm{K}}^{-1} = -\frac{1}{wV}\int_{\theta_3}^{\theta_4} \frac{P\left(q^2\frac{e^{i\theta}}{\beta_2},q\right)P\left(q^2\frac{e^{i\theta}}{\beta_4},q\right)}{\sqrt{\prod_{k=1}^{4}P\left(e^{i(\theta-\theta_k)},q\right)}}e^{i\theta}d\theta \tag{27}$$

The angle θ_i satisfies the following sequence such that $0 < \theta_1 < \theta_2 < \theta_3 < \theta_4 \leq 2\pi$, $\theta_k = \arg\left(\alpha_k\right)$, see Fig. (S3)(a). The function $P\left(\zeta,q\right)$ is related to the first Jacobi Theta function $\Theta_1\left(\zeta,q\right)$:

$$P\left(\zeta,q\right) = -\frac{ie^{-\tau/2}}{Cq^{1/4}}\Theta_1\left(i\tau/2,q\right) \tag{28}$$

where $\tau = -\log\left(\zeta\right)$, and C is a positive constant which will not appear in the following. α and β must satisfy some relationships as:

$$\alpha_1\alpha_2\alpha_3\alpha_4 = 1 \tag{29}$$

$$\beta_1\beta_3 = q^2, \quad \beta_3 = \overline{\beta_1} \tag{30}$$

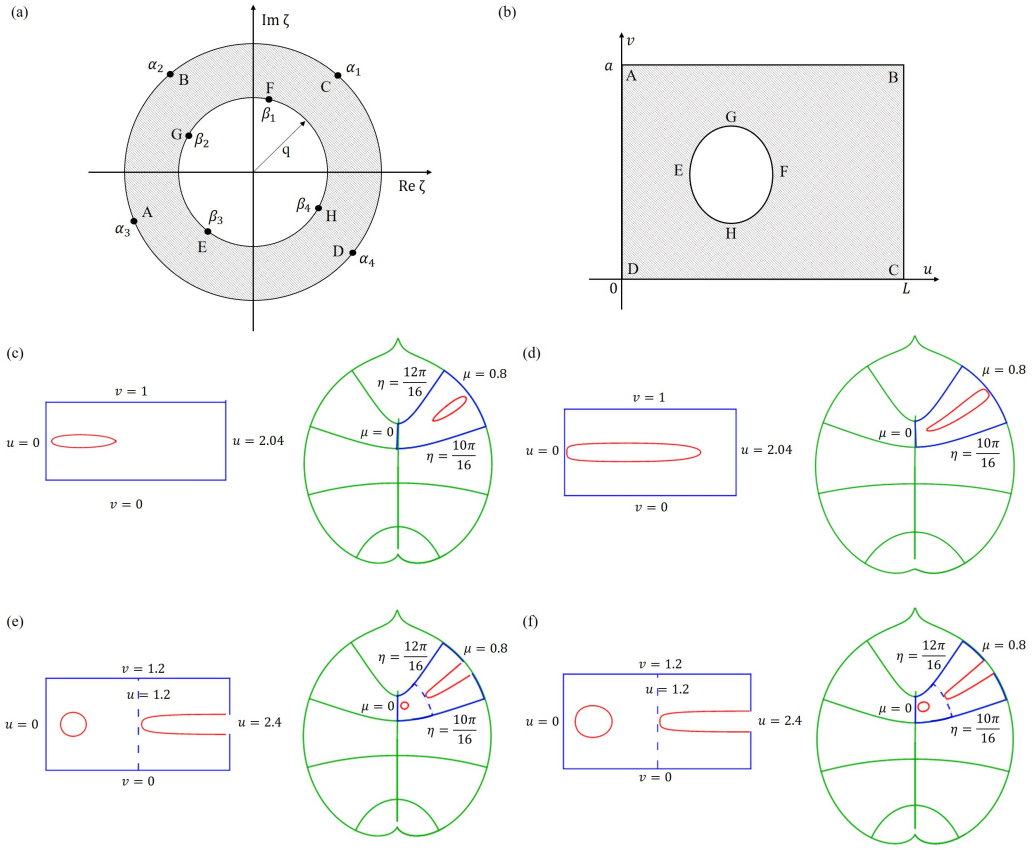

Fig.S 3. In (a) the flow region in the ζ plane, in (b) z_b plane. In (c) and (d), original and transformed hole at time $t = 0$ and t in the z_b plane. (e)(f) Original and transformed holes at $t = 0$ and t in a growing leaf.

$$\beta_2\beta_4 = -q^2, \quad \beta_4 = -\overline{\beta_2} \tag{31}$$

The imposed up and down symmetry of the bubbles (but not left and right symmetry) causes additional relations on α_i:

$$\begin{aligned} \alpha_2 &= -\overline{\alpha_1} \\ \alpha_4 &= -\overline{\alpha_3} \end{aligned} \tag{32}$$

Then, for such solution, there are eight parameters to determine the final position and the bubble shape, the velocity U, V θ_1, θ_3, β_1, β_2, q and a in the calculation. For simplicity, we always define $\theta_3 = \pi$, $\beta_1 = \pi/2$, $V = 1$, so $\theta_4 = 0\,(2\pi)$ and $\beta_3 = 3\pi/2\,(-\pi/2)$. Now, the bubble is obtained by five parameters θ_1, β_2, q and a, U. These parameters are within the following range: $0 < \theta_1 < \pi/2$, $0 < \beta_2 < \pi$, $0 < q < 1$ and $0 < w < +\infty$, $1 < U < +\infty$.

As before, a conformal mapping is required for the transformation of the bubble into a hole located between two lateral veins. By assuming $\theta_1 = 1.547$, $\beta_2 = 0.35$, $q = 0.4$, $w = 1$, $U = 4.5$ and $\theta_1 = 1.41$, $\beta_2 = 0.505$, $q = 0.68$, $w = 1$, $U = 4.5$, the original hole shape in two different states are obtained (see Fig.(S3)(c) and (d)). The transformation can be also achieved by the simple linear relationship, $\mu = -u\pi/(8a) + m_1$ and $\eta = -v\pi/(8a) + m_2$. For the process in Fig.(S3)(c), the constants are $m_1 = 4/5$ and $m_2 = 3/4$, and for the process in Fig.(S3)(d), $m_1 = 4/5$ and $m_2 = 3\pi/4$.

For the two hole examples, we still use the asymmetric bubble function to obtain a small bubble close to the left border and then get a finger-shaped bubble near the right border. The image of the finger-shaped bubble is shifted to the left by the length L, which is the length of the small bubble cell. We treat it as a whole and map it between two lateral veins. For the initial state as shown in Fig.(S3)(e), we define $\theta_1 = 1.24$, $\beta_2 = 0.26$, $q = 0.3$, $w = 1.2$, $U = 2$ to get the small bubble, and $\theta_1 = 0.82$, $\beta_2 = 1.5$, $q = 0.6$, $w = 1.2$, $U = 4.5$ to get the finger-shaped bubble. Current state is shown in Fig.(S3)(f), we define $\theta_1 = 1.22$, $\beta_2 = 0.32$, $q = 0.4$, $w = 1.2$, $U = 2$ to get the small bubble, and $\theta_1 = 0.674$, $\beta_2 = 1.3$, $q = 0.66$, $w = 1.2$, $U = 4.5$ to get the finger-shaped bubble. Linear transformation is the same as before, $\mu = -u\pi/(8w) + m_1$ and $\eta = -v\pi/(8w) + m_2$, the constants being $m_1 = 0$ and $m_2 = 5\pi/8$ for both processes.

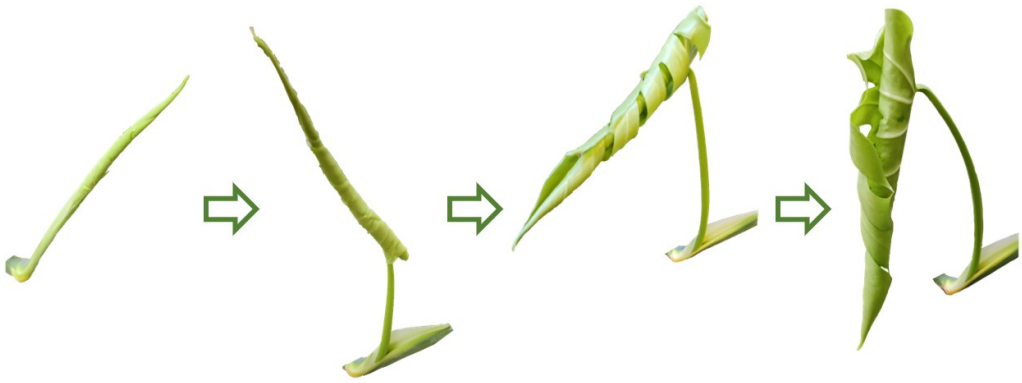

Fig.S 4. Monstera leaf in early stages.

V. IMAGES OF YOUNG MONSTERA

In the main text, we mentioned the young Monstera leaves are inside a sheath, and they will expand over time, as shown in Fig.(S4). It takes about one month for the young leaf to get planar (which may be our initial time), but after, growth will continue during years.

REFERENCES

[1] T. K. DeLillo and A. R. Elcrat, Numerical conformal mapping methods for exterior regions with corners, Journal of Computational Physics **108**, 199 (1993).

[2] T. K. DeLillo, A. R. Elcrat, and J. Pfaltzgraff, Schwarz-christoffel mapping of multiply connected domains, Journal d'Analyse Mathématique **94**, 17 (2004).

[3] T. K. DeLillo and S. Sahraei, Computation of plane potential flow past multi-element airfoils using conformal mapping, revisited, Journal of Computational and Applied Mathematics **362**, 246 (2019).

[4] E. K. Rodriguez, A. Hoger, and A. D. McCulloch, Stress-dependent finite growth in soft elastic tissues, Journal of biomechanics **27**, 455 (1994).

[5] G. Taylor and P. Saffman, A note on the motion of bubbles in a Hele-Shaw cell and porous medium, The Quarterly Journal of Mechanics and Applied Mathematics **12**, 265 (1959).

[6] P. G. Saffman and G. I. Taylor, The penetration of a fluid into a porous medium or Hele-Shaw cell containing a more viscous liquid, Proceedings of the Royal Society of London. Series A. Mathematical and Physical Sciences **245**, 312 (1958).

[7] D. Burgess and S. Tanveer, Infinite stream of Hele-Shaw bubbles, Physics of Fluids A; (USA) **3:3**, 10.1063/1.858146 (1991).

[8] A. M. Silva and G. L. Vasconcelos, Doubly periodic array of bubbles in a Hele-Shaw cell, Proceedings of the Royal Society A: Mathematical, Physical and Engineering Sciences **467**, 346 (2011).

[9] G. L. Vasconcelos, Exact solutions for steady bubbles in a Hele-Shaw cell with rectangular geometry, Journal of Fluid Mechanics **444**, 175 (2001).

[10] D. Crowdy, An assembly of steadily translating bubbles in a Hele-Shaw channel, Nonlinearity **22**, 51 (2008).

[11] D. Crowdy, Multiple steady bubbles in a Hele-Shaw cell, Proceedings of the Royal Society A: Mathematical, Physical and Engineering Sciences **465**, 421 (2009).

Appendix B

List of figures

List of Figures

Appendix C

List of tables

List of Tables

Bibliography

[1] Surrey T, Nédélec F, Leibler S, Karsenti E. Physical properties determining self-organization of motors and microtubules. Science. 2001;292(5519):1167-71.

[2] Ben Amar M, Jia F. Anisotropic growth shapes intestinal tissues during embryogenesis. Proceedings of the National Academy of Sciences. 2013;110(26):10525-30.

[3] Chen X, Dai HH. Stress-free configurations induced by a family of locally incompatible growth functions. Journal of the Mechanics and Physics of Solids. 2020;137:103834.

[4] Ben Amar M, Qiuyang-Qu P, Vuong-Brender TTK, Labouesse M. Assessing the contribution of active and passive stresses in C. elegans elongation. Physical Review Letters. 2018;121(26):268102.

[5] Lewis J. From signals to patterns: space, time, and mathematics in developmental biology. Science. 2008;322(5900):399-403.

[6] Goriely A. The mathematics and mechanics of biological growth. vol. 45. Springer; 2017.

[7] Weinberg RA. How cancer arises. Scientific American. 1996;275(3):62-70.

[8] van der Vliet JA, Boll AP. Abdominal aortic aneurysm. The Lancet. 1997;349(9055):863-6.

[9] Prisant LM, Mondy III JS. Abdominal aortic aneurysm. The Journal of Clinical Hypertension. 2004;6(2):85-9.

[10] Javier RT, Butel JS. The history of tumor virology. Cancer research. 2008;68(19):7693-706.

[11] Chantereau P, Brieu M, Kammal M, Farthmann J, Gabriel B, Cosson M. Mechanical properties of pelvic soft tissue of young women and impact of aging. International urogynecology journal. 2014;25:1547-53.

[12] Hall CM, Moeendarbary E, Sheridan GK. Mechanobiology of the brain in ageing and Alzheimer's disease. European Journal of Neuroscience. 2021;53(12):3851-78.

[13] Koch AL. The problem of hyphal growth in streptomycetes and fungi. Journal of theoretical biology. 1994;171(2):137-50.

[14] Howard RJ, Valent B. Breaking and entering: host penetration by the fungal rice blast pathogen Magnaporthe grisea. Annual Reviews in Microbiology. 1996;50(1):491-512.

[15] Money NP. Wishful thinking of turgor revisited: the mechanics of fungal growth. Fungal Genetics and Biology. 1997;21(2):173-87.

[16] Harold F. How hyphae grow: morphogenesis explained? Protoplasma. 1997;197:137-47.

[17] Goriely A, Tabor M. Biomechanical models of hyphal growth in actinomycetes. Journal of theoretical biology. 2003;222(2):211-8.

[18] Goriely A, Tabor M. Self-similar tip growth in filamentary organisms. Physical review letters. 2003;90(10):108101.

[19] Dumais J, Shaw SL, Steele CR, Long SR, Ray PM. An anisotropic-viscoplastic model of plant cell morphogenesis by tip growth. The International journal of developmental biology. 2006.

[20] Geitmann A, Steer M. The architecture and properties of the pollen tube cell wall. In: The pollen tube: a cellular and molecular perspective. Springer; 2006. p. 177-200.

[21] Frietsch S, Wang YF, Sladek C, Poulsen LR, Romanowsky SM, Schroeder JI, et al. A cyclic nucleotide-gated channel is essential for polarized tip growth of pollen. Proceedings of the National Academy of Sciences. 2007;104(36):14531-6.

[22] Ackerly SC. Kinematics of accretionary shell growth, with examples from brachiopods and molluscs. Paleobiology. 1989;15(2):147-64.

[23] Moss-Salentijn L, Hendricks-Klyvert M. Dental and oral tissues: an introduction. Lea & Febiger; 1990.

[24] Fawcett DWDW, Bloom W. A textbook of histology / Don W. Fawcett. 12th ed. New York ; London: Chapman & Hall; 1994.

[25] Skalak R, Farrow D, Hoger A. Kinematics of surface growth. Journal of mathematical biology. 1997;35(8):869-907.

[26] Moulton DE, Goriely A, Chirat R. Mechanical growth and morphogenesis of seashells. Journal of theoretical biology. 2012;311:69-79.

[27] Moulton DE, Goriely A. Surface growth kinematics via local curve evolution. Journal of mathematical biology. 2014;68:81-108.

[28] Cowin SC. Bone Stress Adaptation Models. Journal of Biomechanical Engineering. 1993 11;115(4B):528-33. Available from: https://doi.org/10.1115/1.2895535.

[29] Huiskes R, Hollister SJ. From Structure to Process, From Organ to Cell: Recent Developments of FE-Analysis in Orthopaedic Biomechanics. Journal of Biomechanical Engineering. 1993 11;115(4B):520-7. Available from: https://doi.org/10.1115/1.2895534.

[30] Taber LA. Biomechanics of Growth, Remodeling, and Morphogenesis. Applied Mechanics Reviews. 1995 08;48(8):487-545. Available from: https://doi.org/10.1115/1.3005109.

[31] Humphrey JD. Continuum biomechanics of soft biological tissues. Proceedings of the Royal Society of London Series A: Mathematical, Physical and Engineering Sciences. 2003;459(2029):3-46.

[32] Cowin SC. Tissue growth and remodeling. Annu Rev Biomed Eng. 2004;6:77-107.

[33] Li B, Cao YP, Feng XQ, Gao H. Surface wrinkling of mucosa induced by volumetric growth: theory, simulation and experiment. Journal of the Mechanics and Physics of Solids. 2011;59(4):758-74.

[34] Stylianopoulos T, Martin JD, Chauhan VP, Jain SR, Diop-Frimpong B, Bardeesy N, et al. Causes, consequences, and remedies for growth-induced solid stress in murine and human tumors. Proceedings of the National Academy of Sciences. 2012;109(38):15101-8.

[35] Ciarletta P. Buckling instability in growing tumor spheroids. Physical review letters. 2013;110(15):158102.

[36] Newman SA, Frisch H. Dynamics of skeletal pattern formation in developing chick limb. Science. 1979;205(4407):662-8.

[37] Skalak R. Growth as a finite displacement field. In: Proceedings of the IUTAM Symposium on Finite Elasticity: Held at Lehigh University, Bethlehem, PA, USA August 10–15, 1980. Springer; 1982. p. 347-55.

[38] Rodriguez EK, Hoger A, McCulloch AD. Stress-dependent finite growth in soft elastic tissues. Journal of biomechanics. 1994;27(4):455-67.

[39] Hsu FH. The influences of mechanical loads on the form of a growing elastic body. Journal of biomechanics. 1968;1(4):303-11.

[40] Thompson DW. On Growth and Form. Bonner JT, editor. Canto. Cambridge University Press; 1992.

[41] Hillebrand G, Liang Z, Yan X, Yoshii T. New wrinkles on wrinkling: an 8-year longitudinal study on the progression of expression lines into persistent wrinkles. British Journal of Dermatology. 2010;162(6):1233-41.

[42] Turner RT. Invited review: what do we know about the effects of spaceflight on bone? Journal of applied physiology. 2000;89(2):840-7.

[43] Puszczałowska-Lizis E, Dąbrowiecki D, Jandziś S, Żak M. Foot deformities in women are associated with wearing high-heeled shoes. Medical science monitor: international medical journal of experimental and clinical research. 2019;25:7746.

[44] Coutts M, Grace J. Wind and trees. Cambridge University Press; 1995.

[45] Skalak R, Zargaryan S, Jain RK, Netti PA, Hoger A. Compatibility and the genesis of residual stress by volumetric growth. Journal of mathematical biology. 1996;34:889-914.

[46] Cowin S. On the modeling of growth and adaptation. Springer; 2006.

[47] Hosford WF. Mechanical behavior of materials. Cambridge university press; 2010.

[48] Schajer GS. Practical residual stress measurement methods. John Wiley & Sons; 2013.

[49] Eskandari M, Kuhl E. Systems biology and mechanics of growth. Wiley Interdisciplinary Reviews: Systems Biology and Medicine. 2015;7(6):401-12.

[50] Du Y, Lü C, Chen W, Destrade M. Modified multiplicative decomposition model for tissue growth: beyond the initial stress-free state. Journal of the Mechanics and Physics of Solids. 2018;118:133-51.

[51] Du Y, Lü C, Destrade M, Chen W. Influence of initial residual stress on growth and pattern creation for a layered aorta. Scientific reports. 2019;9(1):8232.

[52] Xu F, Huang Y, Zhao S, Feng XQ. Chiral topographic instability in shrinking spheres. Nature Computational Science. 2022;2(10):632-40.

[53] Yin J, Gerling GJ, Chen X. Mechanical modeling of a wrinkled fingertip immersed in water. Acta biomaterialia. 2010;6(4):1487-96.

[54] Chen X, Yin J. Buckling patterns of thin films on curved compliant substrates with applications to morphogenesis and three-dimensional micro-fabrication. Soft Matter. 2010;6(22):5667-80.

[55] Balbi V, Kuhl E, Ciarletta P. Morphoelastic control of gastro-intestinal organogenesis: Theoretical predictions and numerical insights. Journal of the Mechanics and Physics of Solids. 2015;78:493-510.

[56] Bayer SA, Altman J. The human brain during the second trimester. CRC Press; 2005.

[57] Roussos ET, Condeelis JS, Patsialou A. Chemotaxis in cancer. Nature Reviews Cancer. 2011;11(8):573-87.

[58] Edelstein L. Greek medicine in its relation to religion and magic. Bulletin of the Institute of the History of Medicine. 1937;5(3):201-46.

[59] Cannon WB. Organization for physiological homeostasis. Physiological reviews. 1929;9(3):399-431.

[60] Cannon WB. The wisdom of the body. Norton & Co.; 1939.

[61] Smith GP. Unacknowledged contributions of Pavlov and Barcroft to Cannon's theory of homeostasis. Appetite. 2008;51(3):428-32.

[62] Zorea AW. Steroids. ABC-CLIO; 2014.

[63] Kluger MJ. Fever: its biology, evolution, and function. Princeton University Press; 2015.

[64] Mahadevan SV, Garmel GM. An introduction to clinical emergency medicine. Cambridge university press; 2012.

[65] Richter JP, et al. The notebooks of Leonardo da Vinci. vol. 2. Courier Corporation; 1970.

[66] Yan J, Yao M, Goult BT, Sheetz MP. Talin dependent mechanosensitivity of cell focal adhesions. Cellular and molecular bioengineering. 2015;8:151-9.

[67] Salbreux G, Jülicher F. Mechanics of active surfaces. Physical Review E. 2017;96(3):032404.

[68] Heer NC, Miller PW, Chanet S, Stoop N, Dunkel J, Martin AC. Actomyosin-based tissue folding requires a multicellular myosin gradient. Development. 2017;144(10):1876-86.

[69] Mietke A, Jemseena V, Kumar KV, Sbalzarini IF, Jülicher F. Minimal model of cellular symmetry breaking. Physical review letters. 2019;123(18):188101.

[70] García-Lara J, Weihs F, Ma X, Walker L, Chaudhuri RR, Kasturiarachchi J, et al. Supramolecular structure in the membrane of Staphylococcus aureus. Proceedings of the National Academy of Sciences. 2015;112(51):15725-30.

[71] Tamemoto N, Noguchi H. Pattern formation in reaction–diffusion system on membrane with mechanochemical feedback. Scientific reports. 2020;10(1):19582.

[72] Berthoumieux H, Maître JL, Heisenberg CP, Paluch EK, Jülicher F, Salbreux G. Active elastic thin shell theory for cellular deformations. New Journal of Physics. 2014;16(6):065005.

[73] Patil N, Bonneau S, Joubert F, Bitbol AF, Berthoumieux H. Mitochondrial cristae modeled as an out-of-equilibrium membrane driven by a proton field. Physical Review E. 2020;102(2):022401.

[74] Brinkmann F, Mercker M, Richter T, Marciniak-Czochra A. Post-Turing tissue pattern formation: Advent of mechanochemistry. PLoS computational biology. 2018;14(7):e1006259.

[75] Prost J, Jülicher F, Joanny JF. Active gel physics. Nature physics. 2015;11(2):111-7.

[76] Mietke A, Jülicher F, Sbalzarini IF. Self-organized shape dynamics of active surfaces. Proceedings of the National Academy of Sciences. 2019;116(1):29-34.

[77] Turlier H, Fedosov DA, Audoly B, Auth T, Gov NS, Sykes C, et al. Equilibrium physics breakdown reveals the active nature of red blood cell flickering. Nature physics. 2016;12(5):513-9.

[78] Ogden R. Non-linear elastic deformations. Elsevier; 1984.

[79] Kaye A, Stepto R, Work W, Aleman J, Malkin AY. Definition of terms relating to the non-ultimate mechanical properties of polymers (recommendations 1998). Pure and applied chemistry. 1998;70(3):701-54.

[80] Dvorkin EN, Goldschmit MB. Nonlinear continua. Springer Science & Business Media; 2006.

[81] Sadik S, Yavari A. On the origins of the idea of the multiplicative decomposition of the deformation gradient. Math Mech Solids. 2017;22(4):771-2.

[82] Flory PJ. Statistical thermodynamics of semi-flexible chain molecules. Proceedings of the Royal Society of London Series A Mathematical and Physical Sciences. 1956;234(1196):60-73.

[83] Kröner E. Kontinuumstheorie der versetzungen und eigenspannungen. vol. 5. Springer; 1958.

[84] Kröner E, Seeger A. Non-linear elasticity theory of dislocations and residual stresses. Archive for Rational Mechanics and Analysis. 1959;3:97-119.

[85] Kröner E. General Continuum Theory of Dislocations and Residual Stresses. Archive for Rational Mechanics and Analysis. 1959;4:273-334.

[86] Lee EH. Elastic-Plastic Deformation at Finite Strains. Journal of Applied Mechanics. 1969 03;36(1):1-6. Available from: https://doi.org/10.1115/1.3564580.

[87] Kondaurov V, Nikitin L. Finite strains of viscoelastic muscle tissue. Journal of Applied Mathematics and Mechanics. 1987;51(3):346-53.

[88] Takamizawa K. Stress-Free Configuration of a Thick-Walled Cylindrical Model of the Artery: An Application of Riemann Geometry to the Biomechanics of Soft Tissues. Journal of Applied Mechanics. 1991 09;58(3):840-2. Available from: https://doi.org/10.1115/1.2897272.

[89] Takamizawa K, Hayashi K. Strain energy density function and uniform strain hypothesis for arterial mechanics. Journal of biomechanics. 1987;20(1):7-17.

[90] Takamizawa K, Matsuda T. Kinematics for Bodies Undergoing Residual Stress and its Applications to the Left Ventricle. Journal of Applied Mechanics. 1990 06;57(2):321-9. Available from: https://doi.org/10.1115/1.2891992.

[91] Beatty MF. Topics in Finite Elasticity: Hyperelasticity of Rubber, Elastomers, and Biological Tissues—With Examples. Applied Mechanics Reviews. 1987 12;40(12):1699-734. Available from: https://doi.org/10.1115/1.3149545.

[92] Ogden RW. Non-linear elastic deformations. Courier Corporation; 1997.

[93] Spencer AJM. Deformations of fibre-reinforced materials; 1972.

[94] Spencer AJM. Constitutive theory for strongly anisotropic solids. Continuum theory of the mechanics of fibre-reinforced composites. 1984:1-32.

[95] Holzapfel GA, Gasser TC, Ogden RW. A new constitutive framework for arterial wall mechanics and a comparative study of material models. Journal of elasticity and the physical science of solids. 2000;61:1-48.

[96] Ciarletta P, Micera S, Accoto D, Dario P. A novel microstructural approach in tendon viscoelastic modelling at the fibrillar level. Journal of biomechanics. 2006;39(11):2034-42.

[97] Ciarletta P, Dario P, Micera S. Pseudo-hyperelastic model of tendon hysteresis from adaptive recruitment of collagen type I fibrils. Biomaterials. 2008;29(6):764-70.

[98] Rivlin R. Large elastic deformations of isotropic materials. I. Fundamental concepts. Philosophical Transactions of the Royal Society of London Series A, Mathematical and Physical Sciences. 1948;240(822):459-90.

[99] Mooney M. A theory of large elastic deformation. Journal of applied physics. 1940;11(9):582-92.

[100] Ogden RW. Large deformation isotropic elasticity–on the correlation of theory and experiment for incompressible rubberlike solids. Proceedings of the Royal Society of London A Mathematical and Physical Sciences. 1972;326(1567):565-84.

[101] Biomechanics: mechanical properties of living tissues. Springer Science & Business Media; 2013.

[102] Gent AN. A new constitutive relation for rubber. Rubber chemistry and technology. 1996;69(1):59-61.

[103] Rolland-Lagan AG, Bangham JA, Coen E. Growth dynamics underlying petal shape and asymmetry. Nature. 2003;422(6928):161-3.

[104] Marder M, Papanicolaou N. Geometry and elasticity of strips and flowers. Journal of statistical physics. 2006;125:1065-92.

[105] Nechaev S, Voituriez R. On the plant leaf's boundary,jupe à godets' and conformal embeddings. Journal of Physics A: Mathematical and General. 2001;34(49):11069.

[106] Marder M. The shape of the edge of a leaf. Foundations of Physics. 2003;33:1743-68.

[107] Liang H, Mahadevan L. The shape of a long leaf. Proceedings of the National Academy of Sciences. 2009;106(52):22049-54.

[108] Dervaux J, Ciarletta P, Amar MB. Morphogenesis of thin hyperelastic plates: a constitutive theory of biological growth in the Föppl–von Kármán limit. Journal of the Mechanics and Physics of Solids. 2009;57(3):458-71.

[109] Dervaux J, Amar MB. Morphogenesis of growing soft tissues. Physical review letters. 2008;101(6):068101.

[110] Müller MM, Amar MB, Guven J. Conical defects in growing sheets. Physical review letters. 2008;101(15):156104.

[111] Amar MB, Müller MM, Trejo M. Petal shapes of sympetalous flowers: the interplay between growth, geometry and elasticity. New Journal of Physics. 2012;14(8):085014.

[112] Xu F, Fu C, Yang Y. Water affects morphogenesis of growing aquatic plant leaves. Physical review letters. 2020;124(3):038003.

[113] Chen X, Ciarletta P, Dai HH. Physical principles of morphogenesis in mushrooms. Physical Review E. 2021;103(2):022412.

[114] Toro R, Burnod Y. A morphogenetic model for the development of cortical convolutions. Cerebral cortex. 2005;15(12):1900-13.

[115] Goriely A, Geers MG, Holzapfel GA, Jayamohan J, Jérusalem A, Sivaloganathan S, et al. Mechanics of the brain: perspectives, challenges, and opportunities. Biomechanics and modeling in mechanobiology. 2015;14(5):931-65.

[116] Tallinen T, Chung JY, Rousseau F, Girard N, Lefèvre J, Mahadevan L. On the growth and form of cortical convolutions. Nature Physics. 2016;12(6):588-93.

[117] Ben Amar M, Bordner A. Mimicking cortex convolutions through the wrinkling of growing soft bilayers. Journal of Elasticity. 2017;129(1):213-38.

[118] Kücken M, Newell AC. Fingerprint formation. Journal of theoretical biology. 2005;235(1):71-83.

[119] Ciarletta P, Amar MB. Papillary networks in the dermal–epidermal junction of skin: a biomechanical model. Mechanics Research Communications. 2012;42:68-76.

[120] Coulombre AJ, Coulombre JL. Intestinal development: I. Morphogenesis of the villi and musculature. Oxford University Press for The Company of Biologists Limited; 1958.

[121] Coulombre AJ, Coulombre JL. Intestinal Development: I. Morphogenesis of the Villi and Musculature. Development. 1958 09;6(3):403-11. Available from: https://doi.org/10.1242/dev.6.3.403.

[122] Hannezo E, Prost J, Joanny JF. Instabilities of monolayered epithelia: shape and structure of villi and crypts. Physical Review Letters. 2011;107(7):078104.

[123] Shyer AE, Tallinen T, Nerurkar NL, Wei Z, Gil ES, Kaplan DL, et al. Villification: how the gut gets its villi. Science. 2013;342(6155):212-8.

[124] Li B, Cao YP, Feng XQ, Yu SW. Mucosal wrinkling in animal antra induced by volumetric growth. Applied Physics Letters. 2011;98(15):153701.

[125] Ambrosi D, Mollica F. On the mechanics of a growing tumor. International journal of engineering science. 2002;40(12):1297-316.

[126] Ramírez-Torres A, Rodríguez-Ramos R, Glüge R, Bravo-Castillero J, Guinovart-Díaz R, Rodríguez-Sanchez R. Biomechanic approach of a growing tumor. Mechanics Research Communications. 2013;51:32-8.

[127] Jain RK, Martin JD, Stylianopoulos T. The role of mechanical forces in tumor growth and therapy. Annual review of biomedical engineering. 2014;16:321-46.

[128] Riccobelli D, Ciarletta P. Morpho-elastic model of the tortuous tumour vessels. International Journal of Non-Linear Mechanics. 2018;107:1-9.

[129] Lucci G, Agosti A, Ciarletta P, Giverso C. Coupling solid and fluid stresses with brain tumour growth and white matter tract deformations in a neuroimaging-informed model. Biomechanics and Modeling in Mechanobiology. 2022;21(5):1483-509.

[130] Wu M, Ben Amar M. Modelling fibers in growing disks of soft tissues. Mathematics and Mechanics of Solids. 2015;20(6):663-79.

[131] Wu M, Ben Amar M. Growth and remodelling for profound circular wounds in skin. Biomechanics and modeling in mechanobiology. 2015;14:357-70.

[132] Zurlo G, Truskinovsky L. Printing non-Euclidean solids. Physical review letters. 2017;119(4):048001.

[133] Zurlo G, Truskinovsky L. Inelastic surface growth. Mechanics Research Communications. 2018;93:174-9.

[134] Truskinovsky L, Zurlo G. Nonlinear elasticity of incompatible surface growth. Physical Review E. 2019;99(5):053001.

[135] Sydney Gladman A, Matsumoto EA, Nuzzo RG, Mahadevan L, Lewis JA. Biomimetic 4D printing. Nature materials. 2016;15(4):413-8.

[136] Dai A, Amar MB. Minimizing the elastic energy of growing leaves by conformal mapping. Physical Review Letters. 2022;129(21):218101.

[137] Chadwick P. Continuum mechanics: concise theory and problems. Courier Corporation; 1999.

[138] Vuong-Brender TTK, Ben Amar M, Pontabry J, Labouesse M. The interplay of stiffness and force anisotropies drives embryo elongation. Elife. 2017;6:e23866.

[139] Ackermann J, Qu PQ, LeGoff L, Ben Amar M. Modeling the mechanics of growing epithelia with a bilayer plate theory. The European Physical Journal Plus. 2022;137:1-29.

[140] Ackermann J. Growth and Mechanics of Cellular Structures : Continuous Models for Tissue Growth [Theses]. Sorbonne Université; 2022. Available from: `https://theses.hal.science/tel-03885483`.

[141] Dkhar J, Pareek A. What determines a leaf's shape? EvoDevo. 2014;5(1):1-19.

[142] Vicente-Manzanares M, Ma X, Adelstein RS, Horwitz AR. Non-muscle myosin II takes centre stage in cell adhesion and migration. Nature reviews Molecular cell biology. 2009;10(11):778-90.

[143] Cowan CR, Hyman AA. Acto-myosin reorganization and PAR polarity in C. elegans. Development. 2007 03;134(6):1035-43. Available from: `https://doi.org/10.1242/dev.000513`.

[144] Olson MF, Sahai E. The actin cytoskeleton in cancer cell motility. Clinical & experimental metastasis. 2009;26(4):273-87.

[145] Palumbo S, Benvenuti E, Fraldi M. Actomyosin contractility and buckling of microtubules in nucleation, growth and disassembling of focal adhesions. Biomechanics and Modeling in Mechanobiology. 2022:1-14.

[146] Levayer R, Lecuit T. Biomechanical regulation of contractility: spatial control and dynamics. Trends in cell biology. 2012;22(2):61-81.

[147] Bertet C, Sulak L, Lecuit T. Myosin-dependent junction remodelling controls planar cell intercalation and axis elongation. Nature. 2004;429(6992):667-71.

[148] Blankenship JT, Backovic ST, Sanny JS, Weitz O, Zallen JA. Multicellular rosette formation links planar cell polarity to tissue morphogenesis. Developmental cell. 2006;11(4):459-70.

[149] Saxena A, Denholm B, Bunt S, Bischoff M, VijayRaghavan K, Skaer H. Epidermal growth factor signalling controls myosin II planar polarity to orchestrate convergent extension movements during Drosophila tubulogenesis. PLoS biology. 2014;12(12):e1002013.

[150] Shindo A, Wallingford JB. PCP and septins compartmentalize cortical actomyosin to direct collective cell movement. Science. 2014;343(6171):649-52.

[151] Priess JR, Hirsh DI. Caenorhabditis elegans morphogenesis: the role of the cytoskeleton in elongation of the embryo. Developmental biology. 1986;117(1):156-73.

[152] Gally C, Wissler F, Zahreddine H, Quintin S, Landmann F, Labouesse M. Myosin II regulation during C. elegans embryonic elongation: LET-502/ROCK, MRCK-1 and PAK-1, three kinases with different roles. Development. 2009;136(18):3109-19.

[153] McKeown C, Praitis V, Austin J. sma-1 encodes a betaH-spectrin homolog required for Caenorhabditis elegans morphogenesis. Development. 1998;125(11):2087-98.

[154] Sulston JE, Schierenberg E, White JG, Thomson JN. The embryonic cell lineage of the nematode Caenorhabditis elegans. Developmental biology. 1983;100(1):64-119.

[155] Sellers JR. Myosins: a diverse superfamily. Biochimica et Biophysica Acta (BBA)-Molecular Cell Research. 2000;1496(1):3-22.

[156] Chisholm AD, Hardin J. Epidermal morphogenesis. WormBook: The Online Review of C elegans Biology [Internet]. 2005.

[157] Rayment I, Holden HM, Whittaker M, Yohn CB, Lorenz M, Holmes KC, et al. Structure of the actin-myosin complex and its implications for muscle contraction. Science. 1993;261(5117):58-65.

[158] Sato M, Schwarz WH, Pollard TD. Dependence of the mechanical properties of actin/α-actinin gels on deformation rate. Nature. 1987;325(6107):828-30.

[159] Humphrey D, Duggan C, Saha D, Smith D, Käs J. Active fluidization of polymer networks through molecular motors. Nature. 2002;416(6879):413-6.

[160] Gardel ML, Nakamura F, Hartwig JH, Crocker JC, Stossel TP, Weitz DA. Prestressed F-actin networks cross-linked by hinged filamins replicate mechanical properties of cells. Proceedings of the National Academy of Sciences. 2006;103(6):1762-7.

[161] Mayer M, Depken M, Bois JS, Jülicher F, Grill SW. Anisotropies in cortical tension reveal the physical basis of polarizing cortical flows. Nature. 2010;467(7315):617-21.

[162] Reymann AC, Staniscia F, Erzberger A, Salbreux G, Grill SW. Cortical flow aligns actin filaments to form a furrow. Elife. 2016;5:e17807.

[163] Williams BD, Waterston RH. Genes critical for muscle development and function in Caenorhabditis elegans identified through lethal mutations. The Journal of cell biology. 1994;124(4):475-90.

[164] Costa M, Draper BW, Priess JR. The Role of Actin Filaments in Patterning theCaenorhabditis elegansCuticle. Developmental biology. 1997;184(2):373-84.

[165] Costa M, Raich W, Agbunag C, Leung B, Hardin J, Priess JR. A putative catenin–cadherin system mediates morphogenesis of the Caenorhabditis elegans embryo. The Journal of cell biology. 1998;141(1):297-308.

[166] Lardennois A, Pásti G, Ferraro T, Llense F, Mahou P, Pontabry J, et al. An actin-based viscoplastic lock ensures progressive body-axis elongation. Nature. 2019;573(7773):266-70.

[167] Moerman DG, Williams BD. Sarcomere assembly in C. elegans muscle. WormBook: The Online Review of C elegans Biology [Internet]. 2006.

[168] Denham JE, Ranner T, Cohen N. Signatures of proprioceptive control in Caenorhabditis elegans locomotion. Philosophical Transactions of the Royal Society B: Biological Sciences. 2018;373(1758):20180208.

[169] Holzapfel GA. Nonlinear solid mechanics: a continuum approach for engineering science. Kluwer Academic Publishers Dordrecht; 2002.

[170] Howard J, Clark R. Mechanics of motor proteins and the cytoskeleton. Appl Mech Rev. 2002;55(2):B39-9.

[171] Vuong-Brender TTK, Suman SK, Labouesse M. The apical ECM preserves embryonic integrity and distributes mechanical stress during morphogenesis. Development. 2017;144(23):4336-49.

[172] Serra M, Nájera GS, Chuai M, Spandan V, Weijer CJ, Mahadevan L. A mechanochemical model recapitulates distinct vertebrate gastrulation modes. bioRxiv. 2021:2021-10.

[173] Zhang H, Landmann F, Zahreddine H, Rodriguez D, Koch M, Labouesse M. A tension-induced mechanotransduction pathway promotes epithelial morphogenesis. Nature. 2011;471(7336):99-103.

[174] Yang Xinyi FT, Kelly Molnar NM, Loic Royer JP, Stephan Grill GM, Labouesse M. Plana asymmetry in epithelial junction elongation results from repeated muscle contraction events. Preprint Sorbonne University. 2023.

[175] Tan T, De Vita R. A structural constitutive model for smooth muscle contraction in biological tissues. International Journal of Non-Linear Mechanics. 2015;75:46-53.

[176] De Vita R, Grange R, Nardinocchi P, Teresi L. Mathematical model for isometric and isotonic muscle contractions. Journal of Theoretical Biology. 2017;425:1-10.

[177] Ciarletta P, Ben Amar M, Labouesse M. Continuum model of epithelial morphogenesis during Caenorhabditis elegans embryonic elongation. Philosophical Transactions of the Royal Society A: Mathematical, Physical and Engineering Sciences. 2009;367(1902):3379-400.

[178] Goriely A, Tabor M. Rotation, inversion and perversion in anisotropic elastic cylindrical tubes and membranes. Proceedings of the Royal Society A: Mathematical, Physical and Engineering Sciences. 2013;469(2153):20130011.

[179] Moulton D, Lessinnes T, Goriely A. Morphoelastic rods. Part I: A single growing elastic rod. Journal of the Mechanics and Physics of Solids. 2013;61(2):398-427.

[180] Moulton DE, Oliveri H, Goriely A. Multiscale integration of environmental stimuli in plant tropism produces complex behaviors. Proceedings of the National Academy of Sciences. 2020;117(51):32226-37.

[181] Kaczmarski B, Moulton DE, Kuhl E, Goriely A. Active filaments I: Curvature and torsion generation. Journal of the Mechanics and Physics of Solids. 2022;164:104918.

[182] Goriely A, Moulton DE, Angela Mihai L. A rod theory for liquid crystalline elastomers. Journal of Elasticity. 2022:1-24.

[183] Nardinocchi P, Teresi L. On the active response of soft living tissues. Journal of Elasticity. 2007;88(1):27-39.

[184] Moulton DE, Lessinnes T, Goriely A. Morphoelastic rods III: Differential growth and curvature generation in elastic filaments. Journal of the Mechanics and Physics of Solids. 2020;142:104022.

[185] Kirchhoff G, Hensel K. Vorlesungen über mathematische Physik. vol. 1. Druck und Verlag von BG Teubner; 1883.

[186] Mielke A. On Saint-Venant's problem for an elastic strip. Proceedings of the Royal Society of Edinburgh Section A: Mathematics. 1988;110(1-2):161-81.

[187] Mora MG, Müller S. Derivation of the nonlinear bending-torsion theory for inextensible rods by Gamma-convergence. preprint. 2002.

[188] Mora MG, Müller S. A nonlinear model for inextensible rods as a low energy Γ-limit of three-dimensional nonlinear elasticity. Annales de l'Institut Henri Poincaré C. 2004;21(3):271-93.

[189] Goriely A, Ben Amar M. On the definition and modeling of incremental, cumulative, and continuous growth laws in morphoelasticity. Biomechanics and modeling in mechanobiology. 2007;6(5):289-96.

[190] Norman KR, Moerman DG. α spectrin is essential for morphogenesis and body wall muscle formation in Caenorhabditis elegans. The Journal of cell biology. 2002;157(4):665-77.

[191] Labouesse M. Viscosity of the intersticial fluid. The fluid contained in the embryo egg is a highly viscous solution full of diverse sugars and other molecules necessary for metabolism The proof is given by the necessity to put the embryo in a solution when the hatching is achieved on purpose The survival of the embryo lasts few hours The solution is a sorbitol aqueous solution containing approximately 1-12 mole/L. 2023.

[192] Jiang X, Zhu C, Ma Y. Density and viscosity of sorbitol/maltitol in L-ascorbic acid aqueous solutions at T=(293.15 to 323.15) K. Journal of Molecular Liquids. 2013;188:67-73.

[193] Landau L, Lifshitz E. Mécanique des fluides, editions Mir. vol. 6; 1971.

[194] Landau LD, Lifshitz EM. Fluid Mechanics: Landau and Lifshitz: Course of Theoretical Physics, Volume 6. vol. 6. Elsevier; 2013.

[195] Zhukoski NE. Conference. Comm Math Soc Kharkov. 1887;17:31-46.

[196] Ballal B, Rivlin R. Flow of a Newtonian fluid between eccentric rotating cylinders: inertial effects. Archive for Rational Mechanics and Analysis. 1976;62:237-94.

[197] Page AP, Johnstone I. The cuticle. WormBook. 2007.

[198] Schulz AK, Boyle M, Boyle C, Sordilla S, Rincon C, Hooper S, et al. Skin wrinkles and folds enable asymmetric stretch in the elephant trunk. Proceedings of the National Academy of Sciences. 2022;119(31):e2122563119.

[199] Schulz A, Dimitriyev M, Singal K, Sordilla S, Sahin A, Boyle C, et al. Creating bio-inspired tissue mimics of African elephant trunks' wrinkled and folded skin. In: APS March Meeting Abstracts. vol. 2022; 2022. p. Z08-010.

[200] Kang R, Branson DT, Guglielmino E, Caldwell DG. Dynamic modeling and control of an octopus inspired multiple continuum arm robot. Computers & Mathematics with Applications. 2012;64(5):1004-16.

[201] Nakajima K, Hauser H, Kang R, Guglielmino E, Caldwell DG, Pfeifer R. A soft body as a reservoir: case studies in a dynamic model of octopus-inspired soft robotic arm. Frontiers in computational neuroscience. 2013;7:91.

[202] Calisti M, Corucci F, Arienti A, Laschi C. Dynamics of underwater legged locomotion: modeling and experiments on an octopus-inspired robot. Bioinspiration & biomimetics. 2015;10(4):046012.

[203] Saffman PG, Taylor GI. The penetration of a fluid into a porous medium or Hele-Shaw cell containing a more viscous liquid. Proceedings of the Royal Society of London Series A Mathematical and Physical Sciences. 1958;245(1242):312-29.

[204] Taylor G, Saffman P. A note on the motion of bubbles in a Hele-Shaw cell and porous medium. The Quarterly Journal of Mechanics and Applied Mathematics. 1959;12(3):265-79.

[205] Burgess D, Tanveer S. Infinite stream of Hele–Shaw bubbles. Physics of Fluids A: Fluid Dynamics. 1991;3(3):367-79.

[206] Vasconcelos GL. Exact solutions for steady bubbles in a Hele-Shaw cell with rectangular geometry. Journal of Fluid Mechanics. 2001;444:175-98.

[207] Crowdy D. An assembly of steadily translating bubbles in a Hele–Shaw channel. Nonlinearity. 2008;22(1):51.

[208] Crowdy D. Multiple steady bubbles in a Hele-Shaw cell. Proceedings of the Royal Society A: Mathematical, Physical and Engineering Sciences. 2009;465(2102):421-35.

[209] Silva AM, Vasconcelos GL. Doubly periodic array of bubbles in a Hele-Shaw cell. Proceedings of the Royal Society A: Mathematical, Physical and Engineering Sciences. 2011;467(2126):346-60.